

Transverse Beam Transfer Functions of Relativistic Ion Bunches

Zur Erlangung des Grades eines Doktors der Naturwissenschaften (Dr. rer. nat.)
genehmigte Dissertation von Paul Andreas Görzen, M. Sc. aus Darmstadt
Tag der Einreichung: 6. 7. 2015, Tag der Prüfung: 25. 9. 2015
Darmstadt (2015) — D 17

Referent: Prof. Dr. rer. nat. Oliver Boine-Frankenheim

Korreferent: Prof. Dr.-Ing. Thomas Weiland



TECHNISCHE
UNIVERSITÄT
DARMSTADT



Fachbereich 18 -
Elektrotechnik und
Informationstechnik
Institut für Theorie
Elektromagnetischer Felder

Transverse Beam Transfer Functions of Relativistic Ion Bunches

Genehmigte Dissertation von Paul Andreas Görgen, M. Sc. aus Darmstadt

Referent: Prof. Dr. rer. nat. Oliver Boine-Frankenheim

Korreferent: Prof. Dr.-Ing. Thomas Weiland

Tag der Einreichung: 6. 7. 2015

Tag der Prüfung: 25. 9. 2015

Darmstadt (2015) – D 17

Bitte zitieren Sie dieses Dokument als:

URN: urn:nbn:de:tuda-tuprints-50230

URL: <http://tuprints.ulb.tu-darmstadt.de/5023>

Dieses Dokument wird bereitgestellt von tuprints,

E-Publishing-Service der TU Darmstadt

<http://tuprints.ulb.tu-darmstadt.de>

tuprints@ulb.tu-darmstadt.de



Die Veröffentlichung steht unter folgender Creative Commons Lizenz:

Namensnennung – Keine kommerzielle Nutzung – Keine Bearbeitung 3.0

Deutschland

<http://creativecommons.org/licenses/by-nc-nd/3.0/de/>

Kurzfassung

Diese Arbeit befasst sich mit der transversalen Dynamik paketierter Ionenstrahlen in Kreisbeschleunigern. Ausgehend von analytischen Modellen zur Beschreibung der transversalen Dynamik gleichförmiger Ionenstrahlen werden analytische Modelle zur Beschreibung der Strahltransferfunktionen (Beam Transfer Functions, BTFs) paketierter Ionenstrahlen im Grenzfall relativistischer Energien entwickelt.

Im Kontext von Colliderringen wird auf Strahltransferfunktionen von Strahlen unter Einfluss der durch den zweiten Strahl verursachten nichtlinearen Felder eingegangen. Außerdem wird der Einfluss von Raumladung im Zusammenhang mit chromatischer Frequenzverbreiterung auf die Strahltransferfunktion diskutiert.

Die Ergebnisse der entwickelten analytischen Modelle der Strahltransferfunktionen stimmen mit den Ergebnissen eines parallel entwickelten Simulationsmodells überein. Einer der wichtigsten Anwendungsfälle von Strahltransferfunktionen ist die Bestimmung der transversalen Oszillationsfrequenz (Betatronfrequenz) der Ionen. Aus diesem Grund werden die Implikationen des Modells für die Bestimmung der mittleren Betatronfrequenz der Teilchen im Zusammenhang mit Raumladung untersucht. Des Weiteren wird die Bestimmung der Betatronfrequenzverteilung anhand der Strahltransferfunktion im Zusammenhang mit Strahl-Strahl Interaktionen näher diskutiert. Dabei wird auf den erwarteten Gültigkeitsbereich der analytischen Modelle eingegangen und dieser anhand der Simulationsergebnissen validiert.

Abschließend werden die erzielten Simulationsergebnisse und die analytischen Modelle für Strahltransferfunktionen von Strahlen unter Einfluss lokaler Nichtlinearitäten aufgrund von Strahl-Strahl Interaktionen mit im Rahmen dieser Arbeit am Brookhaven National Laboratory erhobenen Messdaten verglichen. Es zeigt sich, dass die im Rahmen dieser Arbeit entwickelte Methode zur Bestimmung der Betatronfrequenzverbreiterung auf Meßdaten anwendbar ist, vorausgesetzt kohärente Schwingungen spielen keine Rolle.



Abstract

Transverse beam dynamics of bunched beams in synchrotrons are the subject of this work. Building on analytic models of transverse beam dynamics of coasting beams, analytic models for the description of Beam Transfer Functions (BTFs) of bunched beams in the limit of relativistic energies are derived. Specifically, the BTF of bunched beams under the influence of a local transverse nonlinearity arising from interactions between beams in colliders as well as the BTF of beams dominated by space charge in combination with chromatic frequency spread are discussed.

The resulting analytic models for the BTF are presented and agree with a simulation model developed for the purpose. One of the primary applications of BTFs is the measurement of the transverse oscillation frequency (betatron frequency) of the ions. For this reason this work elaborates on the implications of the model for the determination of the betatron frequency in the presence of space charge. Furthermore the determination of the betatron frequency distribution from the BTF in connection with beam-beam interactions is discussed. The expected regime of validity of the analytic models is validated on simulated BTF data.

Finally, simulated and analytic BTFs of beams under the influence of beam-beam interactions are compared to BTFs measured at the Brookhaven National Laboratory as part of this work. Analytic expectation and simulated BTFs agree with the measurement outcome. A method for obtaining the betatron frequency spread from BTFs of bunched beams with beam-beam interactions developed in this work is successfully applied to measured BTFs.



Contents

1	Introduction	1
2	Synchrotrons and Colliders	5
2.1	Brookhaven National Laboratory	5
2.1.1	The Relativistic Heavy Ion Collider	6
2.2	SIS100 and GSI	8
3	Beam Dynamics and Intensity Effects	11
3.1	Single Particle Dynamics	11
3.1.1	Coordinate System for Beam Dynamics	12
3.1.2	Transverse Beam Dynamics	13
3.1.3	Longitudinal Dynamics	17
3.1.4	Combined Longitudinal and Transverse Effects	19
3.2	Space Charge Fields	22
3.2.1	Incoherent Transverse Space Charge Tune Shift	24
3.2.2	Beam-Beam Effect	27
4	Beam Transfer Functions	33
4.1	Direct Diode Detection for Bunched Beams	34
4.2	BTFs of Coasting Beams with Chromaticity	36
4.3	BTFs in Presence of a Local Transverse Nonlinearity	37
4.4	BTFs with Space Charge	40
4.4.1	Coasting Beams	41
4.4.2	Bunched Beams	42
5	Simulation	45
5.1	Simulation Model	45
5.1.1	General Description of Particle Tracking for Synchrotrons	46
5.1.2	Transverse Fields	47
5.1.3	Space Charge	50
5.1.4	Beam-Beam Effect	52
5.1.5	Electron Lens	55
5.2	Beam Transfer Functions	56

5.3	Validation	57
5.3.1	Beam Transfer Function	57
5.3.2	Space Charge	57
5.3.3	Beam-Beam Effect	57
6	BTFs of Bunched Beams with Space Charge	61
6.1	BTFs of Bunched Beams with Frozen Synchrotron Motion	61
6.1.1	Implications for Tune Measurements	64
6.1.2	Simulation	64
6.2	Finite Synchrotron Frequencies	67
6.3	Determining the Space Charge Tune Shift	68
7	Using BTF to Measure Tune Spread	71
7.1	BTF Phenomenology	71
7.2	Recovery of Tune Distributions	73
7.2.1	Flat Beams	73
7.3	Thresholds	75
7.3.1	Choice of Thresholds	76
7.3.2	Recovered Tune Spreads and Beam-Beam Parameters	77
7.3.3	Thresholds and Coherent Beam-Beam Modes	77
8	Measurement with the Threshold Method	81
8.1	Weak-strong Beam-Beam Interaction as a Stand-in for the Electron Lens	81
8.2	Influence of Bunching	82
8.3	Experimental Setup	84
8.4	Experimental Results	86
8.5	Threshold Method Applied to an Actual Electron Lens	93
8.6	Threshold Method in Presence of Coherent Beam-Beam Modes	93
8.7	Conclusions from the Measurements	95
9	Conclusion and Outlook	97
	Acknowledgements	99
	List of Figures	101
	List of Tables	103
	List of Symbols	105
	List of Acronyms	109
	Bibliography	110
	Curriculum Vitæ	118

1 Introduction

Particle beams have proven to be a flexible tool for basic and applied science for the last century. After the discovery of cathode radiation with the following discovery of the electron in the 1860s [1] and the discovery of α -particle radiation by Ernest Rutherford in 1911 [2], particle accelerators for increasingly higher energies were developed in the first half of the 20th century. The limitations of electrostatic accelerators due to the finite breakdown voltage [3] led to parallel development of oscillating field linear particle accelerators [4]. Additionally, circular accelerators were developed. In these, charged particles are guided on a circular orbit by means of a magnetic field. The particles are repeatedly accelerated when passing the same oscillating electric field. Their increasing velocity is accounted for by either allowing the radius to increase (in cyclotrons) or by synchronous adjustments to the frequency of the accelerating electric field and the amplitude of the guiding magnetic field (in synchrotrons) [5].

Courant and Snyder [6] were the first to develop and mathematically describe strong focusing, a technique used for transverse confinement of beams in all synchrotrons since the 1950s. Strong focusing leads to transverse oscillation (betatron oscillation) with a location-dependent amplitude defined by the beta function. A longitudinal potential imposed on the beam by means of radio frequency cavities causes longitudinal confinement of the particles in bunches. The cavities are tuned to a multiple of the particle revolution frequency. When confined by radio frequency, particles oscillate longitudinally in the imposed potential (synchrotron oscillation). Both betatron and synchrotron oscillations are characterized by the number of oscillations of a particle per revolution. This quantity is called betatron- or synchrotron tune, respectively. The velocity-dependence of the transverse focusing, characterized by the chromaticity, couples the transverse and longitudinal plane resulting in momentum-dependent particle tunes.

The development of increasingly higher energy accelerators allowed new types of nuclear physics experiments which led to discovery and detailed measurements of new particle species. Thus, the development of accelerators fueled the new field of high energy particle physics. Concurrently, accelerators found use in medicine, material sciences, and industry [7]. This work focuses on beam diagnostic methods for strong focusing high energy synchrotrons, which find their primary use in the particle and nuclear physics communities.

As technology advances, physicists demand higher beam qualities and energies to observe increasingly rare processes with maximum precision. To reach higher collision energies, physics experiments observe collisions between particle beams of equal energy to avoid wasting a large amount of energy on the motion of the centre of mass [8]. Special storage rings called colliders [9] such as the Relativistic Heavy Ion Collider (RHIC) [10] provide counter-circulating beams, often traveling in separate magnet systems to produce these collisions. The beam size scales with the emittance, a quantity characterizing the volume of the beam in phase space. Emittance is related to entropy and as such can only grow or be conserved (for the beams of interest for this work). Many physics experiments indirectly require minimization of emittances via requirements for luminosity or beam intensity. Acceleration from the source to top energy in today's highest energy machines takes up to an hour [11, 12]. Beams have to be stored for the experiments for up to approximately a day. In order to maximize the usable time span before the machines need to be re-filled, the preservation of emittance is a key objective of accelerator physics research. Optimization of machine parameters requires detailed measurement and control of beam parameters. One important method of beam diagnostics is the Beam Transfer Function (BTF) [13, 14]. The BTF quantifies the ratio of the beam response to excitation as a function of frequency. BTFs have been shown in the past to allow measurement of the betatron tune [11], the betatron tune spread of coasting beams, and other machine parameters. With tune spread among the primary quantities determining emittance growth, this work focuses on the diagnostic properties of the transverse BTF with respect to the transverse tune spread in bunched beams. In practice, BTFs are often measured for a number of equidistantly spaced excitation frequency samples in a frequency region of interest. The finite measurement time for such a sample determines its frequency resolution.

One of the main factors responsible for emittance growth in modern-day accelerators is the electromagnetic interaction between the particles. The collisions in colliding beam experiments, aside from producing the nuclear and particle physical effects for investigation by experimental physicists, allow the particles of each beam to interact with the electromagnetic field of the other. The amplitude dependent force and resulting spread in particle betatron tunes arising from this so-called beam-beam effect [15] can lead to a deterioration of emittance. In recent years so-called electron lenses [16, 17, 18] were developed for its partial compensation. The analytic expectations for the BTF of a beam experiencing tune spread due to a transverse nonlinearity from this work were successfully applied to develop a method for determination of the tune spread directly from the BTF. One application of this work with respect to beam-beam interactions was the development of a method for quantification of the tune spread introduced by the new electron lenses

at RHIC. In 2015, the method was successfully employed during the commissioning of the electron lenses at RHIC and the results indicate its utility for tune spread measurement in absence of coherent modes.

Especially at low and intermediate particle energies (below 10 GeV for protons), the electromagnetic interaction between the particles of a single beam becomes significant. It leads to a position dependent force on each particle. This so-called space charge force [19] originates from the beam distribution itself and on its own has no influence on the centre of charge motion of the beam. It would not be detectable by BTF measurements but for the interplay with other effects. Due to interaction of the bunches electromagnetic potential with the beam surroundings and due to interference with other sources of tune spread, space charge nevertheless produces a characteristic signature in BTFs for both non-bunched beams [20] and bunched beams [21, 22, 23]. This work investigates BTFs of bunched beams with space charge in a new intermediate regime between the previous theories for coasting beams and for bunched beams with fast synchrotron motion. The results are relevant for conditions as they can commonly be found at intermediate to high energy synchrotrons such as the Schwerionensynchrotron 100 (SIS100).

Only a small amount of beam time is available for accelerator physics experiments in the main rings of large facilities (e.g. RHIC). The priority is the provision of beams for regular physics experiments. Additionally, predictions for machines which are still under design, such as the SIS100 at GSI Helmholtzzentrum für Schwerionenforschung (GSI), are substantial. Furthermore, some beam properties are neither accessible by measurement nor by analytic considerations. For these reasons, computer simulation by means of particle tracking algorithms became a primary tool of accelerator physics research already in the 1960s [24]. Simulations of beams with beam-beam interactions began in the 1970s [25, 26], employing simplified models for the expression of the electromagnetic fields present during the interaction. In the 1990s, computing power became sufficient to allow self-consistent numerical field computations in synchrotron particle tracking simulations on supercomputers [27]. Self-consistent field calculations became more and more commonplace with the rise of computer performance. Today they are part of a variety of particle tracking codes [28, 29]. For this work, a preexisting particle tracking code [30] was extended with modules for simulation of electron lenses, the beam-beam effect, the beam transfer function and chromaticity. Their implementation was successfully validated against well-known analytic results. The code was then used to validate analytic results derived in the course of this work and to validate the applicability of the methods for measurements outside the domain of the narrow prerequisites of the analytic models. Results concerning BTFs of beams under influence of the beam-beam effect and electron lenses were applied to measurement

from the RHIC accelerator proving their applicability for their primary use cases. Simulations of BTFs of bunched beams with space charge in high energy machines were discussed in the framework of analytic results derived for this work.

In this Thesis, Chapter 2 makes the reader familiar with the two machines the work focuses on, namely the SIS100 planned in the framework of the Facility for Antiproton and Ion Research (FAIR) at GSI in Darmstadt and RHIC at BNL in Upton, New York, in the United States. Crucial quantities for the rest of the work are given and the effects of concern are named. Chapter 3 introduces the theoretical framework for the description of ion beams in synchrotrons that is used throughout the remainder of the work. Chapter 4 presents analytical models of BTFs of beams under influence of selected beam dynamics effects. Building on these preparations, Chapter 5 makes the reader familiar with the necessary details of the simulation model. Modules for effects that were introduced to the code in the course of this work are validated against the previously introduced analytic expectations. With the necessary framework in place, Chapter 6 draws conclusions about BTFs of bunched beams in the presence of space charge and explains important consequences for the measurement of machine tune. Furthermore it examines possibilities for recovery of the tune spread from the BTF. With beams under the influence of electron lenses or the beam-beam effect at RHIC in mind, a method for measurement of the transverse tune spread due to a local nonlinearity via the BTF is investigated in Chapter 7. It is argued analytically that recovery of the distribution itself is not possible. Instead, a novel method for the recovery of only the width of the distribution is introduced. Finally, Chapter 8 shows the application of the method to measured BTF of beams with beam-beam interactions and an electron lens. Results show that the method can be used to directly quantify the magnitude of the tune spread introduced by an electron lens and, under special conditions, the beam-beam effect. Chapter 9 concludes with a summary of the results and an outlook.

2 Synchrotrons and Colliders

The focus of this work is on particle dynamics in circular accelerators at intermediate to high energies (above a few GeV/u). Specifically, transverse BTF are discussed on the example of the Relativistic Heavy Ion Collider operating at Brookhaven National Laboratory and the future SIS100 which is to be built in the framework of the FAIR project at GSI. This chapter familiarizes the reader with the two machines and names the key parameters required in the remainder of the work.

2.1 Brookhaven National Laboratory

Brookhaven National Laboratory is a large-scale research facility operated by the U.S. department of energy. Its current research topics range from nuclear and high energy physics over material science and energy research to environmental and neuroscience and biology. Soon after its founding in 1947 the construction of the worlds first synchrotron began, the Cosmotron [31] started operating in 1952. In 1962 the Alternating Gradient Synchrotron (AGS) [32] with a circumference of 807.10 m [33] started operation. To increase the available intensities, the accelerator chain was expanded by a 200 MeV linear accelerator (linac) in 1971. In 1986 the commission of the 201.78 m circumference [34] AGS booster synchrotron increased the available intensities by raising the available injection energy and reducing dynamic vacuum and space charge effects. Until today, besides delivering beam to other experiments, AGS and AGS booster serve as injector to the second-highest energy hadron collider in the world, the 3833.85 m circumference RHIC [33, 10]. To date, RHIC is the only machine in the world to provide polarized proton beams for high energy physics experiments [35]. Ion species from protons up to lead ions can be accelerated for use in RHIC. This work focuses on beams in RHIC and therefore the numerous BNL accelerators unrelated to RHIC proton operation are not mentioned. Detailed descriptions of the booster, AGS and RHIC parameters, can be found elsewhere [34, 10, 36].

A schematic of the accelerator chain used for RHIC proton operation is shown in Figure 2.1. The provision of protons for RHIC proceeds as follows: Polarized proton beams for RHIC are produced by the optically pumped polarized H^- ion source [37]. The source delivers about 10^{12} H^- ions in a single pulse. After preacceleration in the 200 MeV linac, the H^- are injected into the booster by means of charge-stripping

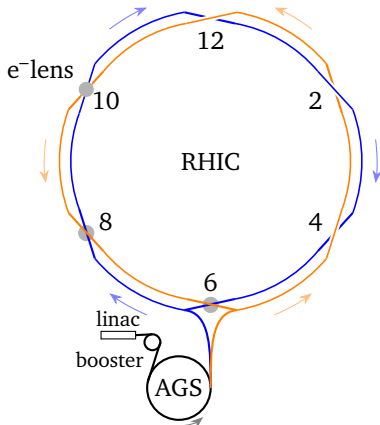


Figure 2.1: The proton-related parts of the RHIC accelerator chain. The rings in this schematic are to scale, but their relative positions are not. The numbers given to the interaction points are indicated. Protons are accelerated by the linac to 200 MeV and accumulated in the booster for up to 20 pulses. After acceleration in the booster to 1.5 GeV they are transferred to AGS and accelerated to 20.58 GeV or more for injection into RHIC. Each of the two separate rings (colored after their names blue and yellow) can be filled with a train of up to 92 proton bunches.

injection. The beam intensity is increased by accumulation of up to 20 pulses. Subsequently, protons are accelerated as a single bunch to about 1.5 GeV [38]. The particles are transferred from the booster to AGS which accelerates the proton bunch up to the RHIC injection energy of (between 20.58 GeV and 28.3 GeV) [39]. Finally, they are injected into RHIC which accumulates up to 92 bunches in each of its two rings.

2.1.1 The Relativistic Heavy Ion Collider

As an ion collider, RHIC consists of two separate synchrotrons allowing beams of the same charge sign¹ to circulate in opposite directions [36]. The two rings for the clockwise and counter-clockwise circulating beams are arbitrarily named *blue*

¹ As opposed to a particle-antiparticle collider in which both beams travel in the same magnet system but have opposite charge signs.

and *yellow*, respectively. They intersect in six interaction points (IPs) numbered according to the hands of the clock, allowing for up to six collisions of the bunches per turn (see Figure 2.1).

At the time of writing and during the experiments of this work, in normal RHIC operation the beams are only brought into collision in two IPs, namely the ones at IP 6 (in the STAR experiment) and at IP 8 (in the PHENIX experiment). At the other IPs they pass each other with a transverse offset of about 30σ (with σ the root mean square width of the Gaussian bunches).

After filling, RHIC provides proton beams with $2 \cdot 10^{11}$ protons per bunch and equal or similar emittances² in both transverse planes between 10 and $20\mu\text{m}$. They can be accelerated to energies up to 250 GeV. After acceleration, focusing functions are adjusted for collision and the beams are brought into collision in the experiments. The beta functions at the experiment IPs, a measure for the focusing strength and an important parameter for the luminosity available to the experiments, are then in the range of 0.8 m in both transverse directions.

Past experience at RHIC indicated that the amplitude dependent force due to electromagnetic interactions in the beam-beam collisions was leading to beam quality deterioration. This was determined as limiting factor for the luminosity available to the experiments. Electron lenses as a counter measure for the nonlinear amplitude dependent force were commissioned and installed in 2013. Figure 2.2 shows one of the RHIC electron lenses. They began operation on gold beams in 2014, and operated with proton beams for the first time in 2015. The electron lenses are installed in IP 10. They are set up to compensate the nonlinear force due to one of the two beam-beam interactions.

The nonlinear transverse force introduced by the electron lenses leads to a characteristic amplitude dependent change in the particles betatron frequencies. The measurement of the BTF with driving frequencies in the baseband below the beam revolution frequency of 78.2 kHz is one of the standard beam diagnostic methods at RHIC [40]. At RHIC the betatron tune $Q_{x,y}$ is in the regime of 30, while the synchrotron tune Q_s is about 0.0003. The key quantity of interest in this work, the tune spread introduced by the electron lens and/or beam-beam interactions, is up to 0.02. An additional source of tune-spread is quantified by the chromaticity ξ_{chrom} which is compensated in RHIC and under normal operating conditions has a value between 0 and 6. The meaning of these parameters is discussed in detail in Chapter 3.

² Normalized 6σ emittances are indicated adhering to convention at RHIC.

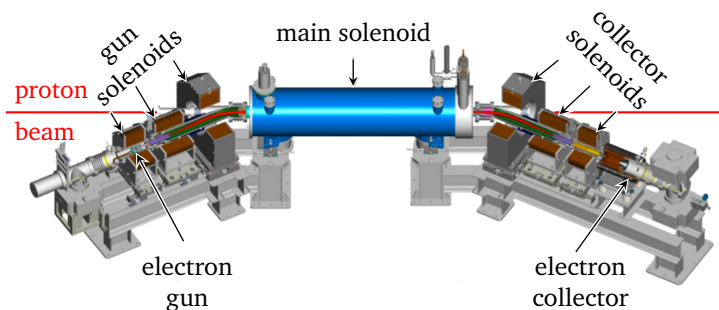


Figure 2.2: Sketch of one of the RHIC electron lenses. The electron beam is produced at the gun which can deliver up to 10 keV electrons at a current of up to 1 A. The beam is guided towards the proton beam and confined on the proton beam axis for 2.1 m by means of solenoid magnets before being guided away from the proton beam and being dumped on the electron collector. The gun design is optimized to deliver Gaussian transverse beam profiles, the beam diameter can be adjusted by manipulating the solenoidal magnetic fields. (Figure from [41])

2.2 SIS100 and GSI

The GSI Helmholtz Centre for Heavy Ion Research is a multipurpose research facility founded in 1969 [42] in Darmstadt, Germany. GSI's first (linear) accelerator, the Universal Linear Accelerator (UNILAC), saw first beam in 1975 and is still in operation today. It can accelerate ions of all species up to uranium to an energy of 11.4 MeV/u. In the early 1990s, GSI was extended by two synchrotrons, the Schwerionensynchrotron (SIS18) and, further downstream, the Experimentierspeicherring (ESR). With a circumference of 216 metres, SIS18 is able to accelerate heavy ions up to 1 GeV/u and protons up to 4.5 GeV [43]. The existing facilities at GSI are the basis for the construction of a large amount of additional machines in the upcoming years: The Facility for Ion and Antiproton Research (FAIR) [44] will greatly extend the research capabilities at GSI. The layout of the planned facility is shown in Figure 2.3. The current GSI accelerators will serve as injectors to the new accelerator complex, the main ring of which is the 1083 m long SIS100 Synchrotron [44].

For the FAIR project, transverse space charge is considered one of the key factors limiting beam intensities [46]. For this reason investigations into direct measurements of the space charge tunes shift appear to be worthwhile. A transverse BTF

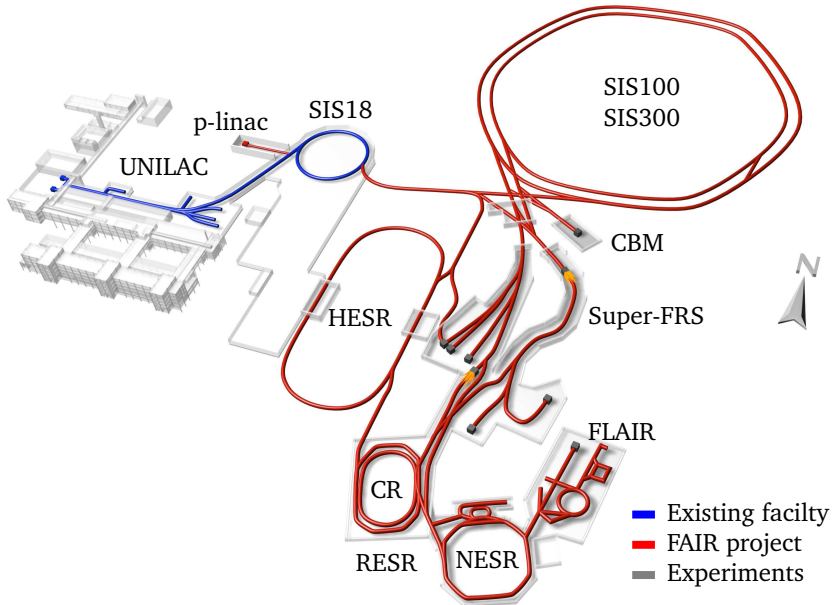


Figure 2.3: Original layout of the FAIR project. Ion beams relevant for this work are produced in sources connected to the UNILAC, accelerated to the SIS18 injection energy of 11.4 MeV/u and injected into SIS18, where they are further accelerated to ion species specific SIS100 injection energies of typically between 200 MeV/u and 4 GeV/u. In SIS100 they can be accelerated to energies of up to 28 GeV/u (for protons) and can be extracted towards the various experiments indicated to the lower right of the picture. (Figure from [45])

system similar to the one installed at RHIC is available at SIS18 and will be available at SIS100 [47]. Previous research at GSI discussed the influence and measurement of space charge on BTF of coasting (DC) beams [48]. Additionally, the influence of space charge on the BTF of bunched beams and the observation of head-tail modes as they appear for SIS18 working conditions was discussed [21, 22, 47]. This work focuses on an intermediate regime: BTF with slow synchrotron motion as they will be observed in SIS100. The various research accelerators downstream of SIS100 (including SIS300) will not be described further and the remainder of the section focuses on the supply chain for SIS100.

Beams for SIS100 are produced in different ion sources connected to the UNILAC and accelerated to the SIS18 injection energy of 11.4 MeV/u. At this energy, space charge limits the reachable proton intensity to $8.7 \cdot 10^{11}$ particles per bunch [46]. Originally, a specialized proton linac was foreseen for FAIR to inject protons at a higher energy (70 MeV with a space charge limit of $5.8 \cdot 10^{12}$ particles per bunch) into SIS18 and thereby be able to reach a higher intensity. Currently injecting protons accelerated by UNILAC to an increased energy of 20 MeV (space charge limit: $1.5 \cdot 10^{12}$ particles per bunch) as an alternative to building a proton linac is discussed [46]. This would result in a corresponding reduction of intensity. After injection into SIS18, the particles are accelerated to 0.2-4 GeV and transferred to SIS100, where they are further accelerated to their individual extraction energies between 1 GeV/u (ions) and 28 GeV (protons). The various storage rings and experiments downstream of SIS100 are not mentioned explicitly here.

In SIS100, the typical synchrotron tunes lie between³ $Q_s = 0.001$ and⁴ $Q_s = 0.0001$. When the excitation time for the measurement of one BTF frequency sample is shorter than the synchrotron period (less than 1000-10000 turns for the beams under consideration), the transverse BTF cannot resolve the effect of synchrotron oscillation [21, 22, 47]. At the same time the beam cannot be described as BTF of a DC beam [48]. When the synchrotron motion becomes slow compared to the measurement time of the BTF, it seems intuitive to model the beam as longitudinally frozen and explore the range of validity of this model in simulation. This model is developed in this work and its range of validity and implications for BTF measurements with space charge in SIS100 are discussed in Chapter 6.

³ Protons at injection, $E_{\text{kin}} = 4 \text{ GeV}$, $\gamma_T = 17.48$, $V_{\text{RF}} = 310 \text{ kV}$, $h = 10$

⁴ For high energy protons, $E_{\text{kin}} = 28.8 \text{ GeV}$, $\gamma_T = 17.48$, $V_{\text{RF}} = 250 \text{ kV}$, $h = 5$

3 Beam Dynamics and Intensity Effects

The complexity of modern-day accelerators has led to the development of a common theoretical framework for the description of transverse beam dynamics. This chapter introduces the framework to the extent needed as a basis for the following chapters. Section 3.1 begins by presenting the basics of single particle beam dynamics. The coordinate system commonly used for description of particle motion in synchrotrons and storage rings is introduced in Subsection 3.1.1. The concept of transverse betatron motion and the resulting machine parameter tune are established in Subsection 3.1.2. Subsection 3.1.3 introduces the necessary elements for the description of longitudinal motion. Finally Subsection 3.1.4 discusses the interplay between longitudinal and transverse dynamics.

Section 3.2 focuses on the beam dynamics that arise from electromagnetic interactions of particles with one another. It begins by discussing transverse electric fields that arise from a particle distribution and their effect on the tune. The results are first applied to the electromagnetic self-fields of the beam (space charge) and subsequently the interaction of beams with one another (beam-beam effect) or with an electron lens.

3.1 Single Particle Dynamics

Particles in accelerators are guided and accelerated via electric and magnetic fields by means of the Lorentz force. The Lorentz force \vec{F} on a particle of charge q with velocity \vec{v} as a result of the electric field \vec{E} and magnetic flux density \vec{B} is given by:

$$\vec{F} = q(\vec{E} + \vec{v} \times \vec{B}) \quad (3.1)$$

and is found in this form in introductory physics text books such as [49]. In vacuum, \vec{B} depends on the magnetic field strength \vec{H} via $\vec{B} = \mu_0 \vec{H}$ with μ_0 the vacuum permeability. In this work the particles typically travel in vacuum. Therefore in this work the field \vec{B} is referenced to as the *magnetic field* for the sake of simplicity. The force on the particle due to a magnetic field scales with v , making it the field of choice for deflection of particle beams when the particle motion becomes relativistic.

The Lorentz force due to a homogeneous magnetic field of strength B acting on a particle of charge q and rest mass m_0 is perpendicular to the direction of motion. The field leads to a circular trajectory of bending radius ρ which satisfies the relation

$$B\rho = \frac{m_0\gamma\beta c}{q}. \quad (3.2)$$

With c the speed of light and γ and β the relativistic factors. $B\rho$ is called the magnetic rigidity. The maximum magnetic rigidity reachable in a storage ring or synchrotron is called its *bending power* and sometimes given to quantify its energy range. The names SIS18 and SIS100 refer to the magnetic bending power of 18 T m and 100 T m of the two machines. Dipolar magnets are used to guide the beam around the machine, quadrupoles are used for focusing. Even higher multipoles are used for Landau-damping, interplane coupling and emittance exchange and are not discussed in this work.

3.1.1 Coordinate System for Beam Dynamics

The coordinate system used in circular accelerators is co-moving with a so-called reference particle. The reference particle is a particle defined by the design of an accelerator. It is commonly chosen to travel with velocity \vec{v}_0 around the machine in the centre of all magnets, such that its trajectory is determined solely by the fields of the dipole magnets (the fields of multipolar magnets of higher order are zero on the trajectory of the reference particle). The reference orbit has a length of C_{circ} and is closed. The reference particle travels along the same trajectories in subsequent revolutions (turns) in the machine. At any given time, the current position of the reference particle on the reference trajectory is given by $s_0(t) = \int_0^t v_0 d\tau$. The co-moving coordinate system in which the beam is described is chosen with the reference particle as its origin. An illustration can be found in Figure 3.1. The unit vector in z direction \vec{e}_z of the system points along \vec{v}_0 . The unit vectors \vec{e}_x and \vec{e}_y in the x and y direction are chosen perpendicular to \vec{e}_z and point in the horizontal and vertical direction respectively. The coordinate system is curved such that \vec{e}_x and \vec{e}_y are perpendicular to the reference trajectory. Thereby a particles z coordinate always relates to a time advance $\Delta t = z/v_0$ with respect to the reference particle. Δt is then the time the reference particle will need to move from its present location s_0 to the longitudinal position of the offset particle at $s = s_0 + z$. The description of transverse beam dynamics often allows to apply the same equations in \vec{e}_x and \vec{e}_y direction. Where this is the case in this document either the indices are discarded or only give the equations for the x are given direction to aid readability. In the first

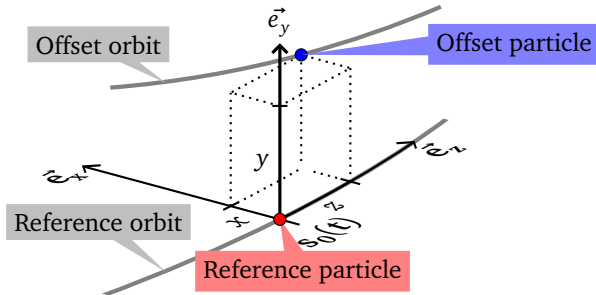


Figure 3.1: Illustration of the co-moving coordinate system used to parametrize the particle position with respect to the reference particle. The reference coordinate system moves with the reference particle such that its origin is always found at $s_0(t)$.

case adding an index x or y gives the equations valid for the respective plane, in the second exchange of x and y yields the equation for the other plane.

The coordinates of particles offset with respect to the reference particle are described by a vector \vec{r} :

$$\vec{r} = \begin{pmatrix} x \\ x' \\ y \\ y' \\ z \\ \delta \end{pmatrix} \quad (3.3)$$

wherein $x' = dx/ds$ and $y' = dy/ds$ are the derivatives of x and y with respect to s . $\delta = (p - p_0)p_0^{-1}$ is the relative momentum deviation with respect to the reference momentum p_0 .

3.1.2 Transverse Beam Dynamics

Particles with transverse momentum offsets $(x', y') \neq 0$ need to be focused back towards the reference trajectory to prevent x and y from growing ad infinitum and the resulting particle loss. Quadrupolar magnets are used to provide the focusing. The focusing force in typical machines is a function of the local quadrupole strength

$k(s)$. Following [50] and assuming a particle with $z = 0$ and $\delta = 0$, the particle motion is then determined by Hills differential equation:

$$x''(s) - k(s)x(s) = 0. \quad (3.4)$$

$x(s)$ describes a transverse oscillation that is commonly referred to as *betatron oscillation*. $k(s)$ is periodic such that $k(s) = k(s + C_{\text{circ}})$ holds. The equation can be solved using Floquets theorem. After some transformations which can be found in standard textbooks [50, 51], the solution is of the form:

$$x(s) = \sqrt{2J\beta(s)} \cos(\Psi(s) + \phi) \quad (3.5)$$

$$x'(s) = \sqrt{\frac{2J}{\beta(s)}} [\alpha(s) \cos(\Psi(s) + \phi) + \sin(\Psi(s) + \phi)] \quad (3.6)$$

with $\beta(s)$ the so-called *beta function*, J the *action* of the particle, a quantity solely dependent on the particle coordinates and discussed in detail below, ϕ a particle-dependent phase,

$$\Psi(s) = \int_0^s \frac{d\tilde{s}}{\beta(\tilde{s})} \quad (3.7)$$

the betatron phase and $\alpha(s) = -\beta'(s)/2$ an optical function. $\alpha(s)$, $\beta(s)$ and $\gamma(s) = (1 + \alpha^2(s))\beta(s)^{-1}$ make up the so-called *Twiss parameters* or *betatron functions* characterizing transverse particle motion in a synchrotron [51, 52]. For readability x -indices were omitted from each quantity in the above. Of course α , β , γ , Ψ and ϕ are all valid for the x direction and a similar set of parameters exists for the y direction. Where explicit separation between the two planes is necessary an index x or y is appended to the corresponding symbols for the lattice functions.

The number of oscillations of a particle around the reference trajectory per revolution is called *tune* and can be calculated by integrating the phase change around the machine [51, 52]:

$$Q = \frac{\Psi(C_{\text{circ}}) - \Psi(0)}{2\pi} \quad (3.8)$$

Like the other quantities related to betatron motion it can be given independently in x and y direction.

The choice of the tunes Q_x, Q_y , also called *working point*, is one of the primary parameters influencing beam lifetime and beam quality in a synchrotron. The working point is identical to the tune of the reference particle and sometimes also

referenced as Q_0 , other particles' tunes may be different. Certain choices for the working point can lead to fast beam loss. The mechanism is easiest to understand for integer Q , which lead to beam loss in presence of a small dipolar magnetic field error: With an integer tune, particles return to each location in the machine with the same betatron phase ϕ . Suppose a small, dipolar magnetic field error influences particle at one lattice location. Upon each passage of the location, the particle experiences a change of its x' coordinate. Upon subsequent passes, the changes happen in phase (the particle always returns with the same phase) and therefore add up, resulting in amplitude growth and particle loss. Higher order magnetic field errors result in amplitude growth and losses for working points fulfilling the condition [53]:

$$nQ_x + mQ_y = o \quad (3.9)$$

with $n, m, o \in \mathbb{Z}$ and $|n| + |m| = l$ the order of the resonance. l gives a measure for the destructiveness of a resonance, where higher orders are less problematic. Figure 3.2 shows the so-called resonance lines, on which Equation 3.9 is fulfilled for $l \leq 1$. In this diagram and in the following, frequently the only the fractional part of

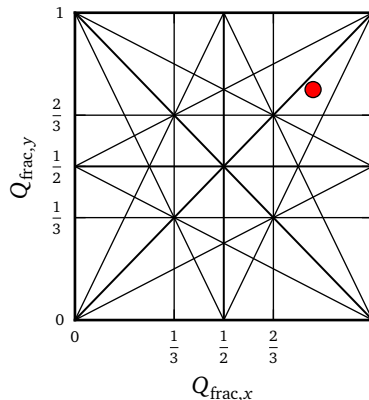


Figure 3.2: Resonance diagram, the resonance condition (Equation 3.9) is fulfilled on the lines for order $l \leq 3$. The ticks are located at rational fractions corresponding to resonances, for example at $1/3$ one finds a 3rd order resonance. The line thickness is scaled with l^{-1} . A working point of $Q_x = 0.8, Q_y = 0.75$ is indicated.

the tune Q_{frac} is indicated instead of Q . The reason for this choice is that the pattern

of resonance lines is identical independently of the integer part of Q . Depending on the required lifetime of the beam and the machine linearity, resonances above a machine dependent minimum between 4th and 10th order resonances are considered safe for the beam.

With the quantities defined above, the translation of one transverse coordinate of a particle between two locations s_1 and s_2 can be written as a transfer matrix [51]:

$$\mathbf{M}(s_2|s_1) = \begin{pmatrix} \sqrt{\beta_2} & 0 \\ -\frac{\alpha_2}{\sqrt{\beta_2}} & \frac{1}{\sqrt{\beta_2}} \end{pmatrix} \begin{pmatrix} \cos \Delta\Psi & \sin \Delta\Psi \\ -\sin \Delta\Psi & \cos \Delta\Psi \end{pmatrix} \begin{pmatrix} \frac{1}{\sqrt{\beta_1}} & 0 \\ \frac{\alpha_1}{\sqrt{\beta_1}} & \beta_2 \end{pmatrix}. \quad (3.10)$$

Here, $\alpha_1, \alpha_2, \beta_1, \beta_2$ the values of the Twiss functions $\alpha(s), \beta(s)$ at the respective locations and $\Delta\Psi = \Psi(s_2) - \Psi(s_1)$. The particles transverse phase space coordinate, here in x direction, changes according to: $(x, x')^T(s_2) = \mathbf{M}(x, x')^T(s_1)$. The translation of particle coordinates between any two points in an uncoupled lattice is then written as:

$$\begin{pmatrix} x \\ x' \\ y \\ y' \end{pmatrix}(s_2) = \begin{pmatrix} \mathbf{M}_x(s_1|s_2) & 0 \\ 0 & \mathbf{M}_y(s_1|s_2) \end{pmatrix} \begin{pmatrix} x \\ x' \\ y \\ y' \end{pmatrix}(s_1) \quad (3.11)$$

With \mathbf{M}_i the transfer matrix in the direction i (with i either x or y). In a real machine, the off-diagonal matrices become nonzero but usually small and \mathbf{M}_i may slightly deviate from Equation 3.10.

Emittance

The action J is an important quantity. In a linear machine as the one discussed above, it can be given separately in the two transverse dimensions x and y and is proportional to the area of the phase-space ellipse depicted in Figure 3.3. A single particle in an ideal machine will always pass an observer with phase-space coordinates on the ellipse. J is a constant of motion in a perfect machine, sometimes the single particle emittance $\epsilon_{\text{particle}} = 2J$ is used instead. The *beam emittance* ϵ is given by the root mean square (RMS) value of the single particle emittances. Beam properties important to physics experiments (e.g. luminosity, total achievable beam current, flux density on a target) frequently require minimization of ϵ . For this reason the emittance is used to quantify the beam quality. ϵ is conserved when particle motion is governed by Equation 3.4. Liouville's theorem states that in the presence of conservative forces as assumed above, infinitesimal phase space

volumina are conserved, so one might naively assume that in presence of static electromagnetic fields emittance does not change. Unfortunately, even neglecting possible time-dependence of fields, Liouville's theorem only holds for infinitesimal volumina. As a result, the emittance is not necessarily conserved even for static electromagnetic fields acting on the beam, the resulting beam dynamics may lead to an increase in emittance. In connection with nonlinear electromagnetic fields, the resonances introduced above can lead to amplitude growth of particles and as a result, RMS emittance growth.

When a particle's transverse oscillation amplitude increases, for example due to an excited resonance (Equation 3.9), its J grows. As it contributes to ϵ via its contribution to the RMS J , the beam emittance grows accordingly.

During acceleration, the beams are only accelerated in longitudinal direction. This leads to a decrease in transverse emittance because the conserved transverse momentum only allows for a smaller transverse velocity with the increasing relativistic mass. To reflect this fact, for accelerated beams it makes sense to introduce a normalized emittance $\epsilon_{\text{normalized}}$ which is conserved under ideal acceleration conditions:

$$\epsilon_{\text{normalized}} = \epsilon \gamma \beta \quad (3.12)$$

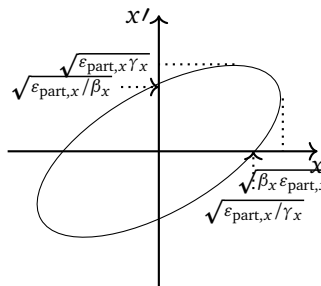


Figure 3.3: Illustration of the betatron phase space ellipse. During betatron motion on a linear lattice a particle's phase space coordinates are always found on this ellipse. ϵ_{part} is proportional to the area of the ellipse.

3.1.3 Longitudinal Dynamics

Two types of beams are mentioned in this work, *coasting* and *bunched* beams. In coasting beams, the particles are not confined longitudinally and therefore circulate

around the ring with constant longitudinal velocity corresponding to their momenta. Each particles betatron frequency is modified due to the machine chromaticity (see Subsubsection 3.1.4). For coasting beams a constant (in time) transverse density profile is assumed. It is solely defined by the beam emittance and the Swiss functions.

In bunched beams, the particles are confined longitudinally by an RF field. Assuming a sinusoidal longitudinal voltage applied to the particle by means of an RF cavity. The resulting longitudinal motion is called synchrotron motion. The equations of synchrotron motion can be found in standard textbooks, for the necessary parts, this discussion follows the approach of [51] closely. The longitudinal equations of motion can be derived from a Hamiltonian, the assumption being that the particle longitudinal motion is sufficiently slow to approximate the discrete kicks at the locations of the RF cavity by an RF potential:

$$H = \frac{1}{2} h \omega_0 \eta \delta^2 + \frac{\omega_0 q V}{2\pi \beta^2 E} \left(\cos \phi - \cos \phi_s^1 + (\phi - \phi_s) \sin \phi_s^0 \right). \quad (3.13)$$

In the equation h is the harmonic number, ω_0 the revolution frequency, η the slip factor, δ the relative momentum deviation, q the particle charge, β the relativistic parameter and E the beam energy. $\phi = hz/C_{\text{circ}}$ is the particle synchrotron phase. In Hadron synchrotrons the reference particle phase ϕ_s is $\phi_s = 0$ for beams at constant energy. Because this discussion assumes constant beam energy the resulting simplifications are marked.

The resulting equations of motion can be linearized and result in sinusoidal oscillations for small amplitude particles. The oscillations are referred to as synchrotron oscillations. They are characterized by the small amplitude angular oscillation frequency ω_s

$$\omega_s = \omega_0 \sqrt{\frac{hqV\eta}{2\pi\beta^2 E}} = 2\pi f_s. \quad (3.14)$$

For easy comparison with the betatron frequency one often gives the synchrotron tune indicating the number of synchrotron oscillations per turn:

$$Q_s = \frac{\omega_s}{\omega_0} = \sqrt{\frac{hqV\eta}{2\pi\beta^2 E}} \quad (3.15)$$

Typical synchrotron tunes in intermediate to high energy ion synchrotrons are $Q_s \leq 10^{-3}$ [51], justifying the initial assumption that synchrotron motion is sufficiently slow to approximate the RF by a smooth potential. The sinusoidal RF force is

not a linear function of the longitudinal particle coordinate and therefore higher amplitude particles will show a lower synchrotron frequency than low amplitude particles. In the theoretical treatment the synchrotron frequency spread is neglected under the assumption that the bunch length justifies the linearization of the RF potential. A treatment including synchrotron frequency spread can be found in [54]. In the simulation model the full sinusoidal RF kick is used.

Synchrotron Satellites of Revolution Harmonics

Particles oscillate longitudinally, therefore the time τ a particle needs for one revolution is modulated with the synchrotron oscillation. For the i^{th} particle [55] with a synchrotron amplitude (in time) of $\hat{\tau}_j$:

$$\tau_j(t) = \hat{\tau}_j \sin(\omega_s t + \Psi_j). \quad (3.16)$$

to a local idealized current measurement device, the particle current presents itself as a train of δ functions yielding a signal [55]:

$$I_j(t) = qf_0 + 2qf_0 \text{Re} \left(\sum_{n=1}^{\infty} e^{-in\omega_0(t+\hat{\tau}_j \sin(\omega_s t + \Psi_j))} \right). \quad (3.17)$$

By means of the Jacobi-Anger-Relation [56] this can be rewritten as:

$$I_j(t) = qf_0 + 2qf_0 \text{Re} \sum_{n=1}^{\infty} I_n \quad (3.18)$$

with

$$I_n = 2\pi qf_0 \text{Re} \left(\sum_{p=-\infty}^{\infty} J_p(n\omega_0 \hat{\tau}_j) e^{-i(n\omega_0 t + p\omega_s t)} e^{-ip\Psi_j} \right). \quad (3.19)$$

From I_n follows the frequency distribution of the signal of the particle: A signal is to be expected at $nf_0 \pm pf_s$ with $p \in \mathbb{Z}$. The signal power at the corresponding frequencies will be proportional to $J_p(n\omega_0 \hat{\tau}_j)^2$ with J_p the Bessel function of order p . The signal clusters around multiples of the revolution frequency f_0 (revolution harmonics). The individual lines are called Synchrotron satellites of the revolution harmonics. An example spectrum is shown in Figure 3.4.

3.1.4 Combined Longitudinal and Transverse Effects

Some effects depend on both longitudinal and transverse beam properties. Therefore they cannot be described by a purely longitudinal or purely transverse picture of the beam dynamics.

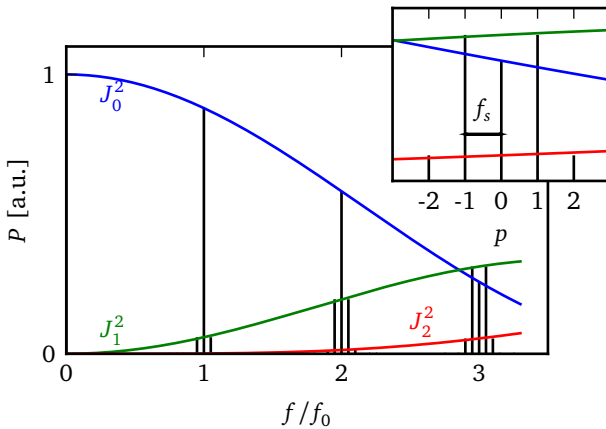


Figure 3.4: Illustration of the longitudinal spectrum of the synchrotron oscillation of a particle. The particle produces harmonics at nf_0 with sidebands at $p f_s$ of intensity $J_p(n\omega_0\hat{\tau}_j)^2$. The sidebands are shown as vertical lines and J_{1-3} is indicated in the figure. The inset magnifies the 3rd harmonic. $\hat{\tau} = 0.1f_0, Q_s = 0.05$ was chosen for this illustration.

Synchrotron Satellites of Betatron Sidebands

The synchrotron motion also affects the betatron oscillation of the particles. Measuring the dipole current $d_j(t) = a_j(t) \cdot i_j(t)$ of particle j at a fixed position returns a train of δ functions with the same time distribution as in Equation 3.17. The amplitude of the pulses follows the betatron oscillation of the particle, the timing is defined by the longitudinal motion of the particle.

The modulation of the dipolar current is given by the particles betatron oscillation via

$$a_j(t) = a_{\text{betatron}} \cos(Q_{\text{frac},j} \omega_0 t + \phi_j) \quad (3.20)$$

. Combining with the timing known from the synchrotron oscillation (Equation 3.17) the dipole signal reads [55]:

$$d_j(t) = a_{\text{betatron}} \cos(Q_{\text{frac},j} \omega_0 t + \phi_j) q f_0 \text{Re} \left(\sum_{n=-\infty}^{\infty} e^{-in\omega_0(t+\hat{\tau}_j \sin(\omega_s t + \Psi_j))} \right), \quad (3.21)$$

which can be rewritten as:

$$d_j(t) = qf_0 + 2qf_0 \operatorname{Re} \sum_{n=1}^{\infty} d_n. \quad (3.22)$$

With [55]

$$d_n = qf_0 a_{\text{betatron}} \operatorname{Re} \left(\sum_{p=-\infty}^{\infty} J_p(v_n) e^{-i((n \pm Q_{\text{frac},j})\omega_0 + p\omega_s)t} e^{-ip\Psi_j - i\phi_j} \right) \quad (3.23)$$

wherein:

$$v_n = \begin{cases} (n \pm Q_{\text{frac}})\omega_0 \hat{\tau}_j & \text{without chromaticity} \\ \left((n \pm Q_{\text{frac}}) - \frac{Q\xi}{\eta} \right) \omega_0 \hat{\tau}_j & \text{with chromaticity} \end{cases} \quad (3.24)$$

The results are derived and discussed at length in [54]. The primary result necessary for this treatise is in the frequencies of the emerging satellites. They can be found at:

$$Q_{l,k} = l \pm Q_{\text{frac}} + kQ_s \quad \text{with } k, l \in \mathbb{Z}, \quad (3.25)$$

now expressed in terms of tunes. Here, the signal at $Q_{l,0}$ is called the l^{th} betatron sideband and $Q_{l,k}$ is the k^{th} synchrotron satellite of the respective betatron sideband.

The betatron sidebands and their synchrotron satellites appear at their expected positions in simulated and measured transverse beam transfer functions [21, 22]. Simulation results are also discussed in Chapter 6.

Momentum Compaction

Off-Momentum particles follow an orbit different from the reference particle due to dispersion. For beams with finite momentum spread, the momentum deviation of the individual particles leads to a momentum dependent revolution frequency f different from the revolution frequency of the reference particle f_0 . The revolution frequency of the i^{th} particle behaves as [51]

$$f_i = (1 + \delta_i \eta) f_0, \quad (3.26)$$

with η the so-called slip factor, a machine- and energy-dependent quantity calculated as

$$\eta = \frac{1}{\gamma_T^2} - \frac{1}{\gamma^2}. \quad (3.27)$$

Here, γ_T , the transition γ , is the relativistic γ for which all particles share the same revolution frequency¹. γ_T is a parameter that can be adjusted via the magnet strengths.

¹ neglecting the small change in η due to the momentum deviation

Chromaticity

Particles with a nonzero momentum deviation δ have a magnetic rigidity (Equation 3.2) different from the reference particle and consequently they experience a different focusing strength $k^*(s)$ in (3.4). For a linear lattice, the resulting error in focusing strength is proportional to the momentum deviation [51]:

$$k^*(s) = k(s) - \overbrace{\delta k(s)}^{\Delta k(s)}. \quad (3.28)$$

The subsequent tune change can be computed by integration of the gradient errors around the machine [57]. Commonly this behaviour is characterized by indicating the chromaticity ξ_{chrom} of a machine:

$$\xi_{\text{chrom}} = \frac{\Delta Q}{\delta} = \frac{1}{4\pi} \int \beta(s) \Delta k(s) ds \quad (3.29)$$

The tune change due to the momentum deviation of a particle can then be computed as $\Delta Q = \delta \cdot \xi_{\text{chrom}}$. Generally the chromatic tune change is a nonlinear function of δ , but in this work the small contribution of higher order chromaticity is neglected. With respect to chromaticity, $\Delta Q_{\text{chrom}} = \delta_{\text{RMS}} \cdot \xi_{\text{chrom}}$ references the RMS tune spread of the beam ΔQ_{chrom} .

3.2 Space Charge Fields

The dynamics that have been described so far are so-called *single particle* dynamics. This means that they take place regardless of how many particles are contained in the beam. Particles were described without accounting for their interaction with other particles. The single particle picture holds well for beams with low particle number, but as the beam current rises, the electromagnetic interaction between particles needs to be taken into account.

The electric potential of a particle bunch of a given density $\varrho(x, y, z)$ travelling in vacuum can be computed by solving the Poisson equation. In the frame of reference of the beam, the particles are in good approximation stationary. For some particle distributions, an analytic solution for the electric fields exists. Most notably this is true for the round Gaussian charge density distribution [15] and the elliptic Gaussian charge density distribution [58]. Both frequently emerge in particle accelerators. Commonly, the interaction of the beam with its surroundings is taken into account via impedances. Impedances describe the frequency dependent coherent self-fields

of the beam via its surroundings in terms of a multipole expansion of the beam signal (usually truncated at the beams dipolar moment)[59]. In this document we assume to be dealing with beams in vacuum and neglect the influence of the surroundings.

Calculating the direct space charge for a coasting beam, the beam is usually modelled as an infinitely long cylinder, the reasoning being that the variation of the beam diameter is sufficiently slow to approximate it by a cylinder slice at a chosen location of the machine. It makes sense to define cylindrical coordinates such that the longitudinal coordinate points in the beam direction. Defining the radial coordinate r and angular coordinate, a normalized transverse circular Gaussian charge density distribution $\varrho(r)$ takes the form

$$\varrho(r) = \frac{nq}{\sigma_r^2 2\pi} \exp\left(-\frac{r^2}{2\sigma_r^2}\right). \quad (3.30)$$

The electric potential φ corresponding to a line density n of particles with charge q with an RMS distribution width of σ_r is then given as [15, 60]²

$$\varphi(r, \sigma_r) = \frac{nq}{4\pi\epsilon_0} \int_0^\infty \frac{\exp\left(-\frac{r^2}{2\sigma_r^2 + \tilde{q}}\right)}{2\sigma_r^2 + \tilde{q}} d\tilde{q}. \quad (3.31)$$

The electric potential shows radial symmetry, for this reason the gradient of the potential will point in the radial direction. The magnitude of the field can be computed as:

$$E_r = -\frac{d}{dr} \varphi(r, \sigma_r) = -\frac{nq}{4\pi\epsilon_0} \frac{\partial}{\partial r} \int_0^\infty \frac{\exp\left(-\frac{r^2}{2\sigma_r^2 + \tilde{q}}\right)}{2\sigma_r^2 + \tilde{q}} d\tilde{q} \quad (3.32)$$

following [15] and taking the derivative first, the radial field simplifies to

$$E_r = -\frac{nq}{2\pi\epsilon_0} \frac{1}{r} \left(1 - \exp\left(-\frac{r^2}{2\sigma_r^2}\right) \right). \quad (3.33)$$

It can be verified that this field is consistent with the initially assumed ϱ : The divergence $\nabla \cdot \vec{E}$ must be equal to $\frac{\varrho}{\epsilon_0}$. In this case a long cylinder of radial symmetry was assumed and E_r is the only finite component of the electric field. Thus

$$\nabla \cdot \vec{E} = \frac{1}{r} \frac{\partial}{\partial r} r E_r = -\frac{nq}{\sigma_r^2 2\pi\epsilon_0} \left(\exp\left(-\frac{r^2}{2\sigma_r^2}\right) \right) = \frac{\varrho(r)}{\epsilon_0}. \quad (3.34)$$

² :

3.2.1 Incoherent Transverse Space Charge Tune Shift

This section discusses space charge for coasting beams. As already mentioned, this assumption demands the beam to have the same transverse charge density distribution everywhere, and, especially that there are no significant current fluctuations over time. When referencing to the self-fields of a beam one uses the term *space charge*. The term *incoherent* in this context refers to the fact that different particles experience a different space charge force, and therefore the transverse dynamics due to space charge is particle dependent. Consequently, when one talks of effects affecting the bunch as a whole one speaks about *coherent* effects.

The magnetic fields observable in the laboratory frame are sourced by a current density proportional to the aforementioned charge distribution. The current density points in the \vec{e}_z direction by virtue of the particles moving in good approximation in parallel, resulting in a current density of $\vec{j} = \vec{e}_z \beta c \varrho$. As a result, the magnetic field \vec{B} is perpendicular to the electric field, lies in the transverse plane and its amplitude is proportional to the electric field. For the round beam the magnetic field points in azimuthal direction. Its transverse components are given by [15]

$$B_x = -\beta E_y c^{-1} \quad B_y = \beta E_x c^{-1} \quad (3.35)$$

The Lorentz force F_L on the particles from the electric and magnetic fields combined reads [19]

$$\vec{F}_L = q(\vec{E} + \vec{v} \times \vec{B}) = q \left(\begin{pmatrix} E_x \\ E_y \\ 0 \end{pmatrix} + \vec{e}_z \times \begin{pmatrix} -\beta c B_y \\ \beta c B_x \\ 0 \end{pmatrix} \right) = q \vec{E} (1 - \beta^2) = q \vec{E} \gamma^{-2} \quad (3.36)$$

For the round Gaussian beam the resulting force is

$$F_L = q E_r \gamma^{-2} \quad (3.37)$$

accordingly.

This force on a particle at a radius r corresponds to a change in the particles $r' = \partial r / \partial s$:

$$r'' = \frac{\partial^2 r}{\partial s^2} = \frac{\ddot{r}}{\beta^2 c^2} = \frac{1}{\beta^2 c^2} \frac{nq^2}{\gamma^3 m_0 2\pi \epsilon_0} \frac{1}{r} \left(1 - \exp\left(-\frac{r^2}{2\sigma_r^2}\right) \right). \quad (3.38)$$

Frequently, it is expressed in terms of the classical particle radius $r_0 = \frac{q^2}{4\pi\epsilon_0 m_0 c^2}$ and with $n = \frac{I}{\beta c}$ it simplifies to

$$r'' = \frac{2I r_0}{\beta^3 \gamma^3 c r} \left(1 - \exp\left(-\frac{r^2}{2\sigma^2}\right) \right). \quad (3.39)$$

Taylor expansion around $r = 0$ gives:

$$r'' \approx \frac{Ir_0}{\beta^3 c \gamma^3 \sigma^2} r. \quad (3.40)$$

Noting that $r'' \propto r$ and corresponding to a change of k in Equation 3.4 of $\Delta k = -r''/r$, the resulting tune change ΔQ_x^{sc} in \vec{e}_x direction for a low amplitude particle can be computed [57] as:

$$\Delta Q_x^{\text{sc}} = -\frac{1}{4\pi} \int_0^{C_{\text{circ}}} \beta_x(s) \Delta k(s) ds = -\frac{1}{4\pi} \int_0^{C_{\text{circ}}} \beta_x(s) \frac{Ir_0}{\beta^3 c \gamma^3 \sigma^2} ds \quad (3.41)$$

which, with constant $\beta(s)\sigma^{-2} = \varepsilon_x^{-1}$ simplifies to:

$$\Delta Q_x^{\text{sc}} = -\frac{Ir_0 R}{2\beta^3 \gamma^3 c \varepsilon_x} = \frac{r_0 N}{4\pi \beta^2 \gamma^3 \varepsilon_x}. \quad (3.42)$$

Here, $N = C_{\text{circ}} I_0 \beta^{-1} c^{-1}$ is the total particle number. Interestingly the tune shift is independent of the beta function. Additionally it should be emphasized that since the net force is defocusing, ΔQ_x^{sc} is a *negative* value. Due to its change of the focusing strength, space charge will also result in a change of the beta function which for the cases of interest here is small and its inclusion is beyond the scope of this discussion.

When replacing r'' by its Taylor expansion to first order around 0 in Equation 3.40, the applicability of the solution is restricted to low amplitude particles. For higher amplitude particles the tune shift is amplitude dependent. Particles in the centre of the beam experience the highest change in tune, and particles far from the centre the lowest. Equations for the amplitude dependence in round or elliptic Gaussian beams are derived in the literature [61, 62]. Here, mostly the formula for round beams is used [61]:

$$Q_x(J_x, J_y) = Q_x^0 + \Delta Q_x^{\text{sc}} \int_0^1 \frac{\left(I_0\left(\frac{J_x z}{2}\right) - I_1\left(\frac{J_x z}{2}\right)\right) I_0\left(\frac{J_y z}{2}\right)}{\exp(z(J_x + J_y)/2)} dz \quad (3.43)$$

$Q_x(J_x, J_y)$ gives the tune of a particle with transverse actions J_x, J_y as a function of lattice tune Q_x^0 and the maximum space charge tune shift $|\Delta Q_x|$. The scaling of Q_x , E_r and ϱ as a function of r is illustrated in Figure 3.5.

The effect of space charge is amplitude dependent, therefore particles in a beam affected by space charge differ in tune. This makes it more difficult to find a working point far from resonance. An example is shown in Figure 3.6. The space charge tune

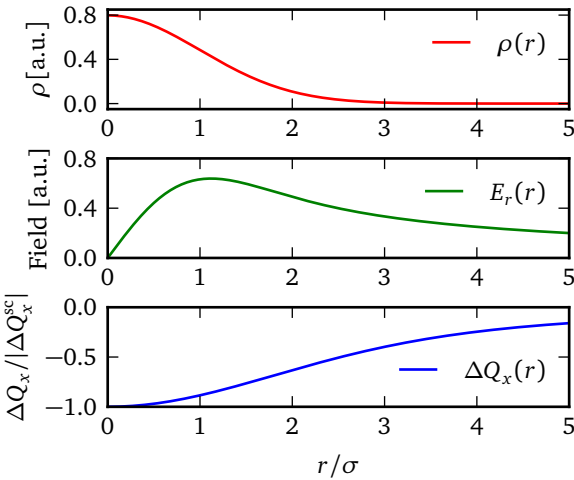


Figure 3.5: Density ϱ , field strength ($E \propto B$) and tune shift (averaged over time) $\Delta Q_x(r, 0)$ for particles as a function of maximum betatron amplitude r along \vec{e}_x . As visible in the plot the largest tune shift is experienced by particles in the centre of the beam. With increasing maximum betatron amplitude, the tune shift experienced by the particles due to the nonlinear electric fields decreases.

spread has a diamond-shape, with particles in the centre of the beam falling onto the lower-left tip of the diamond-shaped tune spread and particles of the highest amplitudes at the other three corners. The working point was chosen such that with the expected space charge the particles would not fall onto the second order resonance (diagonal of the square) or the half order resonance at $Q_y = 1/2$. The working point and space charge used for the figure correspond to the working point for protons at injection in one of the envisioned SIS 100 lattices for the FAIR facility (S. Sorge, personal communication, October 10th, 2014).

In ion operation, incoherent space charge tune shifts are highest at the beginning of the accelerator chain. Incoherent space charge tune shifts of up to 0.25 are tolerated in everyday operation [63], but higher tune shifts of up to 1.9 have been realized in beam experiments at AGS [64] and above 4 in the University of Maryland Electron Ring [65] (UMER, a machine specialized for investigation of space charge effects).

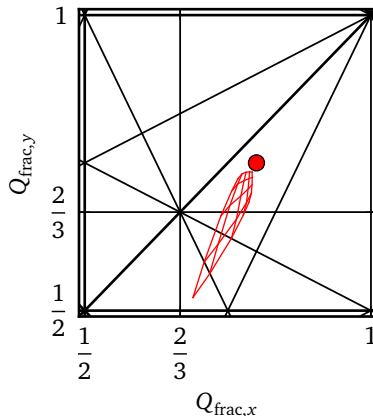


Figure 3.6: Resonance diagram showing resonances up to $l = 3$. The fractional parts of the horizontal and vertical tunes are given as: $Q_{\text{frac},x} = 0.8$, $Q_{\text{frac},y} = 0.75$. The distribution of the particle tunes due to a space charge tune shift of $\Delta Q_x^{\text{sc}} = 0.111$, $\Delta Q_y^{\text{sc}} = 0.228$ is indicated, the particles in the center of the beam are found on the lower left point of the diamond-shaped tune distribution. The working point was chosen to avoid overlap of the space charge tune spread with the $Q_x = 2/3$ or $Q_y = 1/2$.

3.2.2 Beam-Beam Effect

The only two currently operational hadron colliders, the Large Hadron Collider (LHC) and RHIC, rely on two separate magnet systems to collide positively charged ion beams. In colliding beam experiments in these hadron accelerators, physics experiments primarily measure products of head-on collisions: the bunches of the two oncoming beams collide with each other head-on to produce the physical effects to be investigated. In each collision, only very few particles (of the order of 10 to 100) interact with the strong force and produce particle physics. The vast majority of particles of each bunch³ only experience an undesired electromagnetic interaction with particles of the colliding bunch leading to an amplitude dependent defocusing. Furthermore, the interaction allows coherent motion of the bunches against each other [66]. Depending on the design of the interaction region and the longitudinal spacing between the bunches, additional *long range* interactions can occur before

³ At RHIC for proton beams: typically about $2 \cdot 10^{11}$ protons per bunch

and after the bunches collide head-on [15]. In these interactions the bunches see each other from afar, that is to say a few σ of separation. In this work long-range interactions are neglected. The developed methods are employed primarily for diagnosis of electron lenses where no long range interactions occur. Furthermore, the approach focuses on RHIC, where the contributions from long range interactions to the beam-beam effect are small because the separation during long range interaction in noncolliding interaction points is with 30σ rather large [67].

Incoherent Head-on Beam-Beam Effect

The incoherent effects of the beam-beam interaction show strong similarity to the treatment of space charge. The transverse electric field for a circular Gaussian bunch was given in Equation 3.33. For the description of the beam-beam effect, commonly one starts by assuming electric fields arise from a head-on collision between two circular beams of equal emittance at one IP, with equal beta functions for both beams. Comparing with the treatment of space charge in Subsection 3.2.1, the current giving rise to the magnetic field is now in the opposite direction, the sign of \vec{B} and its contribution in Equation 3.37 changes [15]. Equation 3.36 is modified accordingly and gives

$$\vec{F}_l = q\vec{E}(1 + \beta^2). \quad (3.44)$$

Corresponding to an amplitude dependent force of

$$\ddot{r} = \frac{\partial^2 r}{\partial t^2} = \frac{nq^2(1 + \beta^2)}{\gamma m_0 2\pi \varepsilon_0} \frac{1}{r} \left(1 - \exp\left(-\frac{r^2}{2\sigma_r^2}\right) \right) \approx \frac{nr_0(1 + \beta^2)r}{\beta^2 \gamma \sigma^2} \quad (3.45)$$

for the particles in both beams. With the line charge density n as a function of longitudinal position and time (both bunches move with velocity $v = \beta c$ in opposite directions, resulting in a velocity difference in the laboratory frame of $\Delta v = 2\beta c$)

$$n(s, t) = \frac{N}{\sqrt{2\pi}\sigma_s} \exp\left(-\frac{(s + 2\beta ct)^2}{2\sigma_s^2}\right), \quad (3.46)$$

With N the particle number and σ_s the length of the oncoming bunch. Integration of \ddot{r} over the full collision time under the assumption of constant transverse position yields the kick a particle experiences due to one collision. \ddot{r} is time independent apart from n , and so only the integration over n is of interest:

$$\int_{-\infty}^{\infty} n(s, t) dt = \frac{N}{2\beta c}. \quad (3.47)$$

Inserting this into Equation 3.45, taking into account $\beta \approx 1$ for modern-day hadron colliders and Taylor expanding to first order in r , the total momentum change $\Delta r'$ for small amplitude particles during the interaction becomes:

$$\Delta r' = \frac{1}{\beta^2 c^2} \Delta \dot{r} = \frac{Nr_0 r}{\gamma \sigma^2}. \quad (3.48)$$

Computing the change in k and with it the beam-beam analogue of Equation 3.42 results in:

$$\xi_x = -\frac{1}{4\pi} \int_0^{C_{\text{circ}}} \delta_d(s - s_0) \beta_x^* \frac{Nr_0}{\gamma \sigma^2} ds = -\frac{Nr_0}{4\pi \gamma \varepsilon_x} \quad (3.49)$$

with δ_d the Dirac delta function, s_0 the collision location along the ring and, adhering to convention β_x^* the value of $\beta_x(s)$ at the collision point. ξ_x is called the *beam-beam parameter*. $|\xi_x|$ gives the maximum tune shift due to a beam-beam interaction. As already observed for incoherent space charge, the beam-beam tune shift is independent of β_x^* .

For asymmetric (elliptic) beams with $\varepsilon_x \neq \varepsilon_y$ the horizontal beam-beam parameter becomes [68]:

$$\xi_x = -\frac{Nr_0 \beta_x^*}{2\pi \gamma \sqrt{\varepsilon_x \beta_x^*} (\sqrt{\varepsilon_x \beta_x^*} + \sqrt{\varepsilon_y \beta_y^*})}, \quad (3.50)$$

wherein exchange of x and y yields the beam-beam parameter in the vertical direction. As discussed in the treatment of space charge, the defocusing nature of the interaction results in a negative tune change.

Coherent Beam-Beam Effects

In beam-beam interactions, oscillations of bunches with respect to each other *as a whole* becomes possible [66]. These oscillations are called *coherent* oscillations. In the most simple case, two bunches collide with each other once per turn in rings with identical tunes, two coherent modes arise. Firstly the σ mode which can be grasped intuitively: The bunches oscillate in phase, therefore each turn they collide exactly head-on. Since their centres of charge are not offset with respect to each other, no force acts on the centre of charge. This mode is found at the lattice tune Q_x . Secondly the π mode, where the bunches return to the IP out of phase. It is shifted in frequency with respect to the bare tune by $\Delta Q_{x,\pi}$. Extensive numerical computations for the frequency shift were undertaken by Yokoya and Koiso. In [66] they give an phenomenological polynomial fit to their numerical results for the frequency shift of the π mode: for beams with arbitrary but matching aspect ratio

and $r_{\text{aspect}} = \sigma_y^*/(\sigma_x^* + \sigma_y^*)$ (with σ_x^* , σ_y^* the beam size at the collision point) the π mode is shifted by:

$$\frac{\Delta Q_{x,\pi}}{\xi_x} = \Lambda(r_{\text{aspect}}) = 1.33 - 0.37r_{\text{aspect}} + 0.279r_{\text{aspect}}^2. \quad (3.51)$$

For round beams $r = 1/2$ and thus $\Lambda = 1.215$.

For interaction schemes where bunches interact head-on with more than one collision partner (e.g. colliders with multiple interaction points), the calculations become more complex and apart from π and σ mode additional modes appear. This thesis focuses on interaction schemes where only two bunches interact. Empirically, for n collisions per turn of bunches of equal aspect ratios and intensities, the highest incoherent frequency shift is found approximately at $Q_x - n\xi$ and the coherent π mode at $Q_x - n\xi\Lambda$.

If the tunes in the two rings or the bunch intensities differ, the coherent modes may fall together with the incoherent spectrum and be sufficiently damped to not distort the beam spectrum. This scenario is discussed in detail in Chapter 8.

Electron Lens

Contemporary high energy colliders typically have refill times of the order of an hour. To produce required statistics for physics experiments, the beams need to be kept in collision on a time scale of several hours up to a day while preserving emittance as good as possible. The incoherent beam-beam tune spread can, on these time scales, become a problem for emittance preservation: As even high order resonances can lead to emittance increase, the incoherent tune spread limits the number of resonances that can be avoided and thus decreasing the tune spread becomes desirable. In recent years so-called electron lenses have been discussed as a means of compensating the amplitude dependent beam-beam tune shift. In electron lenses, an electron beam of typically a few keV is generated by means of an electron gun, guided in parallel to the proton- or ion beam for a short distance and then disposed of in a collector. A cartoon of an electron lens is shown in Figure 3.7. Typically the beam profile is matched to that of the ion beam at the location of the lens. In this work the transverse shape of the electron beam is assumed to be Gaussian, corresponding to the shape of the proton- or Ion beams. The calculation of the field strength can be done following the same steps as for the beam-beam effect and space charge. The transverse fields for the electron lens can be found in Equation 3.33. Finally the amplitude dependent tune shift experienced by the proton beam due to the interaction follows the same shape as for space charge and the beam-beam effect and can be found in Equation 3.42. A plot of the amplitude dependent tune shift together with the radial electric field was shown in Figure 3.5.

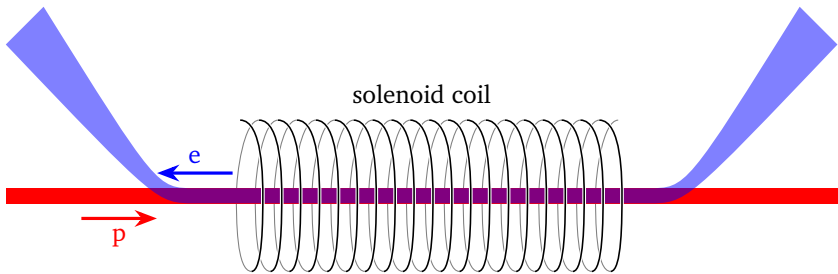


Figure 3.7: Cartoon of an electron lens. An electron beam is guided in parallel to the proton (ion) beam inside a solenoid. The resulting transverse force is amplitude dependent and defined by the chosen electron beam shape. A picture of the electron lens in operation at RHIC can be found in Figure 2.2.



4 Beam Transfer Functions

Beam Transfer Functions are the diagnostic method central to this work. This chapter discusses the BTFs of beams under the influence of the effects introduced in the previous chapter. The chapter begins by defining the BTF. After a short introduction into the most common detector system in Section 4.1, analytic expectations for BTFs of coasting beams with tune spread due to momentum spread and chromaticity are introduced in Section 4.2. In this special case the tune distribution can easily be measured using the BTF, finding a similarly powerful method for recovery of tune spread from transverse sources was a key motivation for this work. In Section 4.3 the analytic expectations for BTFs of coasting beams interacting with a local transverse nonlinearity such as an electron lens or a beam-beam interaction in absence of coherent modes are introduced. Space charge is not localized but instead moves with the beam. Expectations for BTF of coasting and bunched beams in the presence of space charge are introduced in Section 4.4.

The primary method of beam diagnostics investigated in this work are transverse beam transfer functions. A schematic of a BTF measurement is shown in Figure 4.1. The BTF represents the response of the centre of charge $\langle x \rangle(t)$ of the beam to a transverse excitation $a(t)$. The BTF is then given as the fraction of complex response amplitude and complex driving amplitude and as a function of frequency. The hat over the x and a denotes their Fourier transform with respect to time.

$$R(\Omega) = \frac{\langle \hat{x} \rangle(\Omega)}{\hat{a}(\Omega)}. \quad (4.1)$$

It is understood that the BTF is meaningful when taken at small excitation amplitudes where $\langle \hat{x} \rangle(\Omega)$ scales linearly with $\hat{a}(\Omega)$. While some measure only the absolute value of the BTF, for this work the complex value of the BTF is of interest.

In the cases where the beam exhibits coherent modes like the synchrotron satellites and the coherent beam-beam modes in Chapter 3, the BTF will generally show a high amplitude response at an angle of $\pi/2$ at the position of the coherent mode. Primarily cases where no coherent modes are visible to the BTF are of interest as these cases are most likely to show a direct correspondence between the tune distribution inside the beam and the BTF. In the application of the BTF in Chapter 6 and Chapter 8, the circumvention of coherent modes in measurements and under what conditions they may be neglected are discussed.

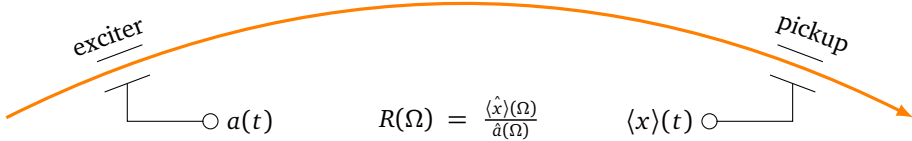


Figure 4.1: Measurement of a transverse BTF: The beam is excited by means of a transverse excitation signal of amplitude $a(t)$. The responding motion of its center of charge $\langle x \rangle(t)$ is recorded. The BTF $R(\Omega)$ can be calculated from x and a as a function of frequency Ω .

4.1 Direct Diode Detection for Bunched Beams

Pickup signals of bunched beams provided by transverse pickups typically contain a lot of energy at high frequencies corresponding to the beam current changes over the length of one bunch (up to the GHz regime, corresponding to current changes on a few centimetres length of bunches approaching the speed of light) [69]. In transverse BTFs one is frequently only interested in the fractional part of the machine tune. This is due to practical considerations: With a pickup in only one position of the machine, an observer can only determine the fractional part of the number of oscillations per revolution. Additionally many effects do not depend on the absolute value of the tune, just on its fractional part. Finally, the integer part of the tune is normally known from the machine design, allowing to compute the absolute value of the tune once the fractional tune is measured. For these reasons it is sufficient to measure tune at baseband, that is to say below the revolution frequency of the beam. In large accelerators baseband frequencies are typically very low (78 kHz in RHIC, 11 kHz in LHC).

To provide a low noise signal in the baseband, a measurement method recently introduced at many facilities [40] is the direct diode detection (DDD), now commonly used for base band tune (BBQ) and BTF measurements. BBQ based beam oscillation monitors were used for the BTF measurements at RHIC and are available at GSI [40].

To prepare for the modelling of the BTF system in Chapter 5, a brief introduction of the concept of direct diode detection is shown in Figure 4.2: compared with regular beam oscillation monitors where V_{con} is measured, DDD connects a diode and an RC circuit to each of the pickup output electrodes. The diodes allow the pulses from each bunch to charge the capacitor. After the bunch has passed (and V_{con} decays to zero, leading to strong high frequency components in V_{con}), V_{DDD} only

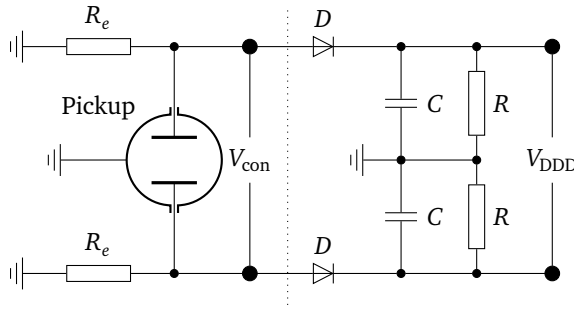


Figure 4.2: Simplified schematic of the direct diode detection circuitry, from [69]. Conventional BTF systems used the voltage V_{con} , direct diode detection provides a smooth signal in the baseband by adding the right half of the circuit. The quantity of interest is then V_{DDD}

decays slightly through the resistor. The next bunch recharges the capacitor. This method allows to boost the signal amplitude in the baseband frequency range at the cost of the (unwanted) signal amplitude of the higher harmonics. V_{DDD} retains very little of the initial high-frequency content, and is passed through additional filters and amplified before being read out digitally by low frequency equipment. V_{DDD} is assumed to follow the centre-of-charge oscillation of a passing bunch.

Using direct diode detection, the signal to noise ratio of BTF measurements can be boosted significantly by using the low frequency output of the direct diode system as the signal component $\langle \hat{x} \rangle(\Omega)$ (see Equation 4.1). $R(\Omega)$ can then be determined in connection with the driving amplitude $\hat{a}(\Omega)$. The absolute value of the BTF is commonly not required but instead only the shape is of interest (as can be seen upon revisiting Equation 4.1, any changes in amplitude can be absorbed in the constant C).

In BTF measurements commonly the exciter and the pickup are located at different locations of the ring. The phase shift due to signal propagation time in the cable and the beam oscillation between exciter and pickup needs to be accounted for by calibration. In absence of exact knowledge of all cable lengths and electronic delays, the BTF phase ϕ can be shifted such that ϕ outside the betatron peak is 0 or π respectively and the BTF peak is found at $\pi/2$.

4.2 BTFs of Coasting Beams with Chromaticity

BTFs of coasting beams have been investigated at length and some examples are discussed in textbooks such (see e.g. [70]). One example of interest to us is the BTF of a beam with a tune spread originating solely from momentum spread in connection with chromaticity. In this case all the particles have a fixed transverse (betatron-) frequency, and can be treated as harmonic oscillators. The transverse coordinate x of a particle therefore behaves according to:

$$x'' + \omega^2 x = A \cos \Omega t \quad (4.2)$$

with ω the particles eigenfrequency and Ω and A the driving frequency and amplitude respectively. This section follows [70] in the derivation of the analytic result for the BTF.

The general solution for the driven harmonic oscillator can be written as:

$$x(t) = x_0 \cos(\omega t) + \dot{x}_0 \frac{\sin \omega t}{\omega} + \frac{A}{\omega^2 - \Omega^2} (\cos \Omega t - \cos \omega t) \quad (4.3)$$

Assuming the oscillation starts from the equilibrium ($x_0 = \dot{x}_0 = 0$) this simplifies to:

$$\frac{A}{(\omega - \Omega)(\omega + \Omega)} (\cos \Omega t - \cos \omega t) \quad (4.4)$$

By decomposing into the contributions of sum and difference frequency this can be written as a product of a fast sine function representing the oscillation and a slow sine function representing the beating over time.

$$\frac{2A}{\omega^2 - \Omega^2} \sin\left(\frac{\omega + \Omega}{2} t\right) \sin\left(\frac{\omega - \Omega}{2} t\right) \quad (4.5)$$

From the Tailor expansion it can be shown that the fraction from the first term cancels with the slow sine and the result is finite even for $\omega = \Omega$. Expanding the denominator and making the assumption that the system is observed at $\omega \simeq \Omega$ so that $(\omega + \Omega) \simeq 2\Omega$ this can be rewritten to

$$\frac{A}{(\omega - \Omega)} \sin\left(\frac{\omega + \Omega}{2} t\right) \sin\left(\frac{\omega - \Omega}{2} t\right). \quad (4.6)$$

In the case of tune spread due to chromaticity alone, the density of particles in the beam ψ is known as a function of the betatron frequency ω , the BTF R at frequency Ω can be calculated by integrating over the particle peak amplitudes:

$$R(\Omega) = C \cdot \int_{-\infty}^{\infty} \frac{1}{\omega - \Omega} \psi(\omega) d\omega \quad (4.7)$$

wherein C a normalization constant. This work focuses on the BTF shape and not the overall amplitude of the BTE. Therefore make no effort is made to explicitly calculate C . The pole at $\Omega = \omega$ can be accounted for by adding a small imaginary term to the denominator or by means of the residue theorem. Finally one arrives at:

$$R(\Omega)_x = -iC\pi\psi(\Omega) + C \cdot \text{P.V.} \int_{-\infty}^{\infty} \frac{1}{\omega - \Omega} \psi(\omega) d\omega \quad (4.8)$$

Wherein P.V. denotes Cauchys principal value integral. For BTFs described by Equation 4.8, the betatron frequency distribution is proportional to the imaginary part of the BTF. Measuring the imaginary part of the BTF of a beam with tune spread solely from tune spread and chromaticity yields the betatron frequency distribution in the plane of the BTF.

For certain distributions ψ Equation 4.8 can be solved analytically. In this work beams are assumed to be Gaussian in longitudinal direction. For a corresponding Gaussian distribution of betatron frequencies around the betatron tune ω_0 with width σ_ω :

$$\psi(\omega) = \frac{1}{\sqrt{2\pi}\sigma_\omega} e^{-\frac{(\omega-\omega_0)^2}{2\sigma_\omega^2}} \quad (4.9)$$

Equation 4.8 solves to:

$$R(\Omega) = \frac{C}{\sigma_\omega} \sqrt{\frac{\pi}{2}} e^{\frac{(\Omega-\omega_0)^2}{2\sigma_\omega^2}} \left(i + \text{erfi}\left(\frac{(\Omega-\omega_0)}{\sqrt{2}\sigma_\omega}\right) \right) \quad (4.10)$$

As mentioned before the imaginary part is proportional to $\psi(\Omega)$, thus the frequency distribution can directly be read from the imaginary part of the BTF. An example of $R(\Omega)$ for Gaussian beams is shown in Figure 4.3. The hope for establishing a similar relation for BTFs with tune spread due to a transverse nonlinearity motivates investigation of the BTF of a beam with a transverse nonlinearity in the following section.

4.3 BTFs in Presence of a Local Transverse Nonlinearity

Since the tune distribution due to momentum spread and chromaticity can be readily read from the BTF one might assume that the same is the case for the tune spread from other sources. Such a method would make it easy to obtain the tune distribution caused by the beam-beam effect or electron lenses by means of BTF measurements. In the following, the theory of BTFs in presence of a transverse

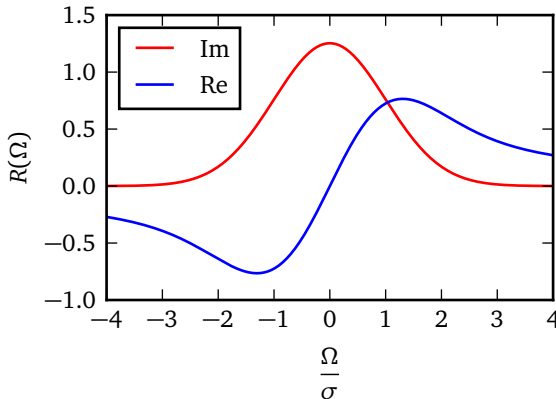


Figure 4.3: Real and imaginary part of a BTF R of a beam with momentum spread and chromaticity (Equation 4.10) as a function of frequency normalized by the RMS frequency deviation σ .

nonlinearity is reviewed with this in mind. The nonlinearity giving rise to the tune spread for the beam-beam effect and electron lenses lies in the plane of the BTF measurement. The particles changing amplitude caused by the BTF excitation results in a change in their frequency, therefore a treatment different to the case of constant betatron frequency is required. This section neglects the influence of synchrotron motion and the formulae are *a priori* only valid for coasting beams. Chapter 8 will investigate the limits in which they can nevertheless be applied to bunched beams in the limit of frozen synchrotron motion. Furthermore, application of the BTF as modelled in this section to beams under the beam-beam effect assumes that no coherent beam-beam modes are observed. This is possible under specific machine conditions also discussed in Chapter 8.

An extensive discussion can be found in [71], the core of which is repeated here:

Up to now each particle was assumed to correspond to a *linear* driven harmonic oscillator, with a Hamiltonian given by:

$$H(q_x, p_x, t) = \omega \frac{q^2 - p^2}{2} - qf(t) \quad (4.11)$$

wherein the normalized betatron coordinates q and p can be calculated from the transverse actions J and phases ϕ (introduced in Subsection 3.1.2) via

$$q = \sqrt{2J} \cos(\phi) \quad p = \sqrt{2J} \sin(\phi). \quad (4.12)$$

The Hamiltonian for linear betatron motion in one of the transverse planes is given via Equation 4.12 and Equation 4.11 by inserting the respective J and ϕ in the plane. In the linear system the Hamiltonians in the x and y directions are uncoupled.

Now the beam distribution can be written as the sum of the initial distribution ψ_0 and a perturbation due to the BTF excitation ψ_1 :

$$\psi(J_x, J_y) = \psi_0(J_x, J_y) + \epsilon \psi_1(J_x, J_y, \phi_x, t) \quad (4.13)$$

ψ_0 is independent of the betatron phase space angles ϕ , because it has a constant density in the ϕ direction. After excitation in x direction, the phases in x direction, ϕ_x , are correlated, therefore ψ_1 is ϕ_x dependent.

The BTF can then be obtained by solving the Vlasov equation for the transverse degrees of freedom. Using the phase space flow obtainable from the Hamiltonian, the Vlasov equation reads [71]:

$$\frac{\partial \psi}{\partial t} + \dot{\phi}_x \frac{\partial \psi}{\partial \phi_x} + J_x \frac{\partial \psi}{\partial J_x} + \dot{\phi}_y \frac{\partial \psi}{\partial \phi_y} + J_y \frac{\partial \psi}{\partial J_y} = 0 \quad (4.14)$$

In presence of a nonlinearity, a Hamiltonian $H_0(J_x, J_y, \phi_x, \phi_y)$ of an integrable system is assumed. In presence of a horizontal driving force the Hamiltonian is [71]:

$$H = H_0(J_x, J_y, \phi_x, \phi_y) - x f_x(t) \quad (4.15)$$

which under the assumption that still $x = \sqrt{2J_x} \cos \phi_x$ leads to [71]:

$$\dot{\phi}_x = \frac{\partial H_0}{\partial J_x} - \frac{\cos \phi_x}{\sqrt{2J_x}} f_x(t) \quad (4.16)$$

$$\dot{J}_x = -\sqrt{2J_x} \sin \phi_x f_x(t) \quad (4.17)$$

with

$$\omega_x(J_x, J_y) = \frac{\partial H_0}{\partial J_x} \quad (4.18)$$

the amplitude dependent betatron frequency.

Introducing an infinitesimal excitation:

$$f_x(t) = \epsilon B e^{-i\Omega t} \quad (4.19)$$

and inserting Equation 4.17 and Equation 4.13 into Equation 4.14, after expanding to first order in ϵ , one arrives at [71]:

$$\frac{\partial \psi_1}{\partial t} + \omega_x(J_x, J_y) \frac{\partial \psi_1}{\partial \phi_x} - B \sqrt{2J_x} \sin(\phi_x) e^{-i\Omega t} \frac{\partial \psi_0}{\partial J_x} = 0. \quad (4.20)$$

The ansatz:

$$\psi_1 = g(J_x, J_y) e^{i(\phi_x - \Omega t)} \quad (4.21)$$

substituted into Equation 4.20, and averaged over ϕ yields:

$$g(J_x, J_y) = \frac{\frac{B}{2} \sqrt{2J_x} \frac{\partial \psi_0}{\partial J_x}}{(\Omega - \omega_x(J_x, J_y))} \quad (4.22)$$

which can be used to calculate the response amplitude to the excitation [71]

$$\langle x \rangle = \iint_V dx dy dp_x dp_y x \psi(x) \quad (4.23)$$

$$= \epsilon \iint_0^\infty dJ_x dJ_y \iint_0^{2\pi} d\phi_x d\phi_y \sqrt{2J_x} \cos \phi_x \psi_1 \quad (4.24)$$

$$= 2\pi f_x(t) \iint_0^\infty dJ_x dJ_y \int_0^{2\pi} d\phi_x \sqrt{2J_x} \cos(\phi_x) \frac{\sqrt{2J_x} \exp(i\phi_x)}{2(\Omega - \omega_x(J_x, J_y))} \frac{\partial \psi_0}{\partial J_x} \quad (4.25)$$

and finally the BTF R :

$$R_x(\Omega) = 2\pi^2 \iint_0^\infty dJ_x dJ_y \frac{J_x}{\Omega - \omega_x(J_x, J_y)} \frac{\partial \psi_0}{\partial J_x}. \quad (4.26)$$

It is obvious that this result is sufficiently different from Equation 4.8 to demand further discussion. In Chapter 7 the implications for the tune spread recovery from BTFs are discussed. Figure 4.4 shows Equation 4.26 for an electron lens, modeled by using the tune spread due to a round Gaussian charge distribution matched to the beam size (Equation 3.43) for $\omega_x(J_x, J_y)$. Note that for the BTF with chromaticity (Figure 4.3) the tune distribution was exactly proportional to $\text{Im}(R)$ and therefore not displayed separately. In the case of the electron lens, the tune distribution differs from $\text{Im}(R)$ as shown in Equation 4.26.

4.4 BTFs with Space Charge

Unlike a localized transverse nonlinearity, transverse space charge as a source of tune spread alone is not visible in the BTF. When the beam is excited by an external signal, the excitation acts on all particles. As a result, the centre of charge of the beam and with it the incoherent space charge moves together with the excitation. The centre of charge responds to the excitation at the frequency of the lattice tune and the beam is indistinguishable from the BTF of a beam without space charge. Nevertheless space charge produces a specific signature in BTFs when considered in combination with other sources of tune spread in both coasting and bunched beams.

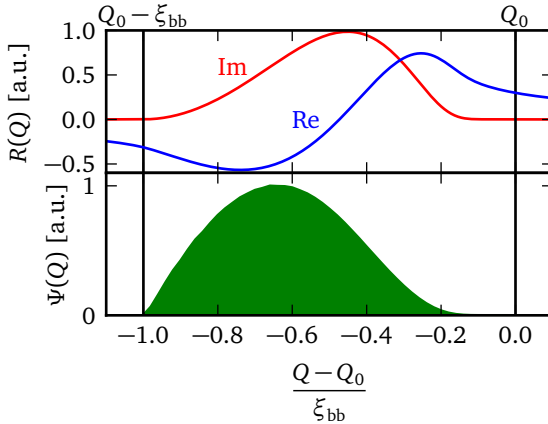


Figure 4.4: Real and imaginary part of the BTF of a round Gaussian beam interacting with a transverse nonlinearity caused by a matched defocusing round Gaussian transverse charge distribution. As can be seen $\text{Im}(R)$ is not proportional to the tune density Ψ as was the case for the tune spread from out-of-plane sources (Equation 4.8).

4.4.1 Coasting Beams

In the presence of space charge, chromaticity and transverse impedances, BTFs of coasting beams show characteristic deformations [20, 72]. An extensive description of the processes can be found in [48]. Here only the results needed as a starting point for the following considerations for bunched beams are quoted.

Assume a coasting beam of Gaussian velocity profile and chromaticity as the source of tune spread, the BTF $R(\Omega)$ can be found in Equation 4.10, which is revisited here for convenience:

$$R(\Omega) = \frac{C}{\sigma_\omega} \sqrt{\frac{\pi}{2}} e^{\frac{(\Omega - \omega_0)^2}{2\sigma_\omega^2}} \left(i + \text{erfi} \left(\frac{\Omega - \omega_0}{\sqrt{2}\sigma_\omega} \right) \right) \quad (4.10 \text{ revisited})$$

In presence of space charge on top of the chromaticity, the BTF modifies to [20]:

$$R_{\text{sc}}(\Omega) = \frac{R(\Omega)}{1 - (\Delta U_{\text{coh}} - \Delta U_{\text{sc}} + i\Delta V_{\text{coh}})R(\Omega)} \quad (4.27)$$

with the so-called space charge parameter

$$\Delta U_{\text{sc}} = \frac{\Delta Q_{\text{sc}}}{\Delta Q_{\text{chrom}}} \quad (4.28)$$

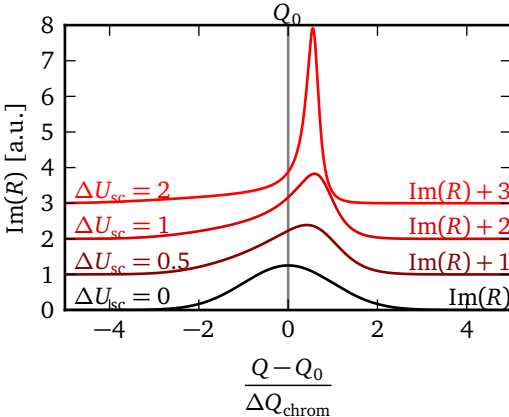


Figure 4.5: Deformation of the BTF of a coasting beam due to space charge. The imaginary part of the BTF $R(\Omega)$ is shown for different space charge parameters ΔU_{sc} . The curves displayed with an offset indicated in the plot. Note that for increasing space charge, the peak becomes narrower and moves away from the bare tune Q_0 .

corresponding to the incoherent space charge tune shift (Equation 3.42) in units of the RMS chromatic tune spread ΔQ_{chrom} and $\Delta U_{coh} + i\Delta V_{coh}$ the coherent tune shift due to coherent space charge and impedances, also in units of the chromatic tune spread.

In absence of a space charge and impedances, $R_{sc} = R$. In the resulting BTF, the peak shifts and deforms depending on the space charge related parameters. Examples are shown in Figure 4.5. The model is validated against measured and simulated BTFs [20, 48] and will later be employed to the BTF implementation carried out for this work.

4.4.2 Bunched Beams

For bunched beams with significant contributions of synchrotron motion to the transverse spectra (see Chapter 6), transverse spectra of the betatron sidebands split into the well-known synchrotron satellites (Subsubsection 3.1.4). In the presence of space charge, these spectra experience deformations. For a simplified model of the

beam assuming constant density and square beam pipe, the tune shift ΔQ_k of the k^{th} synchrotron satellite with respect to the lattice tune is given by [62, 22, 23]:

$$\Delta Q_k = -\frac{\Delta Q_{\text{sc}} + \Delta Q_{\text{coh}}}{2} \pm \sqrt{\frac{(\Delta Q_{\text{sc}} - \Delta Q_{\text{coh}})^2}{4} + (kQ_s)^2} \quad (4.29)$$

with ΔQ_{sc} the incoherent space charge tune shift and ΔQ_{coh} a real coherent tune shift representing image current effects. The $+$ is used for $k > 0$. It can be easily validated that Equation 4.29 simplifies to Equation 3.25 in absence of space charge and coherent tune shifts.



5 Simulation

This chapter introduces the computational model used for particle tracking simulations in accelerators. Section 5.1 begins with a general description of a particle tracking code as it is used for simulation of particles in synchrotrons. In the following, the models for key effects are described in detail, namely space charge, the beam-beam interaction and an electron lens. Section 5.2 presents the modelling of the BTF. Finally the code is validated on analytic expectations in Section 5.3.

5.1 Simulation Model

In particle tracking simulations of synchrotrons, a large number of macroparticles, (typically $10^5 - 10^7$) are represented by their respective coordinates x, x', y, y', z and δ . Each of these macroparticles corresponds to a number of real particles. For this work, simulations were carried out in a simulation code forked from the particle tracking code PATRIC [30]. The simulation code was written in the C++ programming language [73]. In the simulation the accelerator is approximated by a set of linear transfer matrices (Equation 3.10) corresponding to the properties of the accelerator elements. The set of matrices used to represent the machine is often called the *lattice*. The lattice of an actual machine can be computed from simulated or measured magnet data by means of the software MAD-X [74]. Lattices used to represent real-world machines often incorporate matrices representing beamline elements of different lengths s_i . Application of a matrix of an element of length s_i corresponds to a time step of duration $t_i = s_i/(\beta c)$ with the speed of light c . In modelling of space charge, the lattice is often replaced by a constant focusing model, as is the case in this work. A constant focusing model replaces the lattice by an alternative lattice of constant focusing strength k (Equation 3.4) in both spatial directions. The beta functions on that lattice are constant and as a result $\alpha(s)$ is 0. The elements of a constant focusing lattice are commonly chosen to be of uniform length and thus their transfer matrices are identical and the time stepping is uniform. The alternative lattice is chosen such that quantities of interest, most importantly the (fractional) tune, are identical to the machine lattice.

5.1.1 General Description of Particle Tracking for Synchrotrons

The general workflow of the particle tracking code is shown in Figure 5.1. For this work the basic beam dynamics for particle tracking in synchrotrons available in PATRIC [30] was used. In the beginning of the simulation, the lattice is loaded from a file or generated according to simulation input data. Then, the particle coordinate vector is initialized by a matched particle distribution randomly generated according to simulation input. In this context, *matched* means that the probability density function is chosen such that it stays constant for in absence of effects causing emittance growth.

At a lattice element n , the particle tracking code determines the beam physics effects that have to be applied at the element, and applies them by modifying the particle coordinate vectors accordingly. Some of the effects used in simulation are explained in detail in the rest of this chapter. Subsequently beam properties for simulation output are calculated and the particles are translated to the next cell via the linear transfer map $\mathbf{M}(s_n, s_{n+1})$. The process is repeated until a desired number of simulation steps has passed. The lattice is periodic with the machine circumference, therefore the transfer map $\mathbf{M}(s_n, s_{n+1})$ repeats every turn in the machine, $\mathbf{M}(s_n, s_{n+1}) = \mathbf{M}(s_n + C_{\text{circ}}, s_{n+1} + C_{\text{circ}})$.

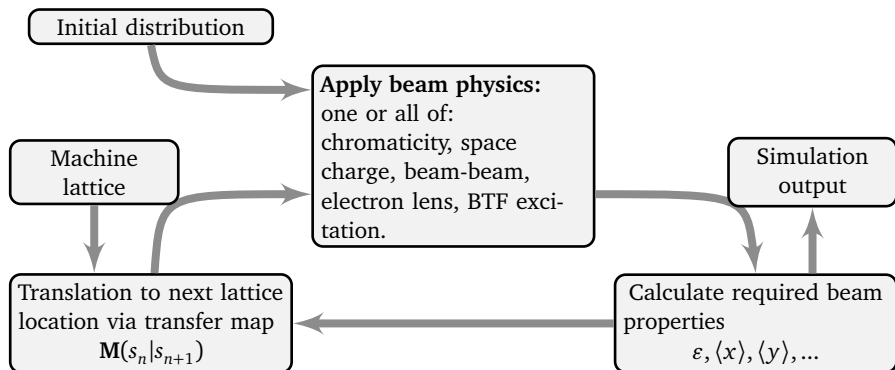


Figure 5.1: Flowchart of the particle tracking simulation. Prior to simulation an initial matched particle distribution for the desired beam parameters is generated. Additionally a machine lattice is either obtained from an input file or generated as a constant focusing lattice reproducing desired machine parameters (primarily the tune).

5.1.2 Transverse Fields

In an ideal world, it would be feasible to derive the beam fields by solving the full Maxwell's equations for the bunch and its surroundings. Unfortunately the computing power required to do so is not available. Nevertheless simplifying assumptions allow simulation of particles including transverse self fields with good accuracy. As discussed in Section 3.2 the transverse self fields originating from the charge distribution of the beam are typically derived from the density distribution by means of solving the Poisson equation to derive the transverse electric field of the particles in vacuum and making use of the proportionality of magnetic and electric field in the transverse direction (Equation 3.36). In simulation, several methods can be used to calculate the transverse fields. Effects of the bunch wake fields acting back on the bunch can be taken into account by means of impedances. Here the influence of impedances is neglected and the transverse fields are calculated assuming beams are travelling in vacuum (neglecting the beam pipe and any other surroundings). For the case of BTF with the beam-beam effect, this simplification can be justified by the good agreement between analytic expectation, simulation and the measurement results. In the case of space charge, if necessary, the underlying theory already allows for integration of impedances, which, however, were neglected for this first feasibility study.

Analytic Fields

For several beam shapes (among others circular or elliptic Gaussian beams), the transverse fields can be calculated analytically. Modules for this calculation were implemented in the framework of this thesis. In simulations where the beams are Gaussian and the beam-shape is assumed to be stable, whenever transverse fields are needed for the simulation, one has to compute the location of the beam centre of charge, i.e. in x -direction:

$$\mu_x = N^{-1} \sum_{i=1}^N x_i \quad (5.1)$$

and the standard deviation

$$\sigma_x = \sqrt{N^{-1} \sum_{i=1}^N (x_i - \mu_x)^2}. \quad (5.2)$$

The values y direction, μ_y and σ_y , are defined accordingly. Then one can use the analytic equations to calculate the beam fields, the results for round beams ($\mu_x \simeq \mu_y$) can be found in Equation 3.33, the more computationally heavy equations for elliptic

beams can be found in the literature [62]. This technique was frequently used in the past but is now more and more replaced by self-consistent field calculations for discretized particle densities derived from the particle distribution. Wall geometries can be taken into account by modelling the appropriate image charges and image currents [19].

Self-consistent Fields

The assumption that the beam shape stays constant is not always justified. For example the centre of a transversely Gaussian beam might oscillate against the beam edges upon excitation, leading to a deviation from Gaussian shape. Modern-day computer systems make it possible to calculate the transverse self fields by evaluation of the Poisson equation for the discretized two-dimensional transverse density distribution of a beam for arbitrary boundary conditions [75]. To do so the particles are interpolated onto a grid, a set of spatial coordinates on which the density is approximated. Codes using this approach are referred to as *Particle in Cell* codes [76, 77]. The calculation of the field is carried out for the discrete grid. The resulting fields are subsequently interpolated back onto the particles resulting in a change of the particle momenta. The technique does not account for direct collisions between particles, but this is not an issue only the macroscopic field is of interest.

In PATRIC such a discretization is used, Figure 5.2 shows a graphical representation of the process: A square grid of length l_{grid} with N_{grid} cells in both spatial directions is used. The grid spacing $\Delta x_{\text{grid}}, \Delta y_{\text{grid}}$ is therefore given by

$$\Delta x_{\text{grid}} = \Delta y_{\text{grid}} = \frac{l_{\text{grid}}}{N_{\text{grid}} - 1}. \quad (5.3)$$

The particle coordinates x_j, y_j are interpolated onto a two dimensional grid with discrete coordinates x_n, y_m . The local density ρ at a grid point is then given by [77]

$$\rho(x_m, y_n) = \frac{q_{\text{macro}}}{\Delta z \Delta x_{\text{grid}} \Delta y_{\text{grid}}} \sum_{j=0}^{N-1} S_{2\text{D}} \left(\frac{x_j - x_m}{\Delta x_{\text{grid}}}, \frac{y_j - y_n}{\Delta y_{\text{grid}}} \right) \quad (5.4)$$

The function $S_{2\text{D}}$ is introduced for the purpose of distributing the particle charge onto its neighbouring grid cells. It can be thought of as the macroparticle shape and needs to be chosen such that

$$\frac{\Delta z \Delta x_{\text{grid}} \Delta y_{\text{grid}}}{q_{\text{macro}}} \sum_{m=0}^{N_{\text{grid}}-1} \sum_{n=0}^{N_{\text{grid}}-1} \rho(x_n, y_m) = N \quad (5.5)$$

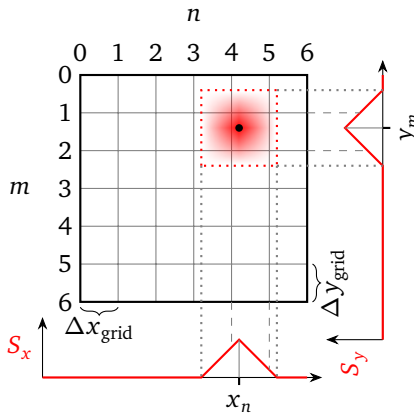


Figure 5.2: Illustration of the particle to grid interpolation. The particle distribution function (Equation 5.7) is shaded in red. The dotted red line marks the border where $S = 0$. The example particle contributes to the cells with $n = 4, 5$ and $m = 1, 2$. The horizontal and vertical component of the two-dimensional triangle function $S_x = S((x_j - x_m)\Delta x_{\text{grid}}^{-1})$ and S_y are also shown.

In PATRIC typically triangle functions are used for S ,

$$S(l) = (1 - |l|) \cdot H(1 - |l|), \quad (5.6)$$

wherein H denotes the Heavyside step function. For interpolation on the two-dimensional grid, the two dimensional unit triangle function is used for S_{2D} :

$$S_{2D}(d_x, d_y) = S(dx)S(dy) \quad (5.7)$$

is used, S_{2D} then corresponds to a linear interpolation of the particle charge onto the neighbouring 4 grid points.

Having discretized the two-dimensional charge density on the grid, the corresponding electric potential on the same grid can be obtained by solving the Poisson equation discretely. In PATRIC, the electric potential is obtained by means of spectral methods [77]. Fourier transforms are done using the fast Fourier transform algorithm. Boundary conditions for free space or arbitrary beam pipe geometries can be introduced by adding a pseudopotential calculated by means of an appropriate Greens function to the boundary of the simulatory domain [75]. The x and y components of the electric field corresponding to the obtained potential are obtained by numerical differentiation of the discretized potential.

With the discrete electric fields on the grid, the electric field for a given particle location x_j, y_j can be obtained. The field grid is projected back onto the particle coordinates by means of the same interpolation function S ,

$$E_x(x, y) = \sum_{n=0}^{N_{\text{grid}}-1} \sum_{m=0}^{N_{\text{grid}}-1} E_x(x_m, y_m) S\left(\frac{x - x_m}{\Delta x_{\text{grid}}}, \frac{y - y_n}{\Delta y_{\text{grid}}}\right), \quad (5.8)$$

and the resulting force on the particles can be calculated via the proportionality between the electric and magnetic fields (Equation 3.36). The y component of the electric field at a particles location can be obtained by replacing E_x with E_y in Equation 5.8.

5.1.3 Space Charge

For the simulation of beams under the influence of space charge, the transverse fields of the particle distribution need to be taken into account. In this work, the longitudinal force components of space charge are neglected. The transverse dynamics differ depending on whether coasting or bunched beams are simulated. The general workflow valid for both cases is shown in Figure 5.3. For this work, pre-existing modules for space charge effect were bugfixed and optimized for efficiency.

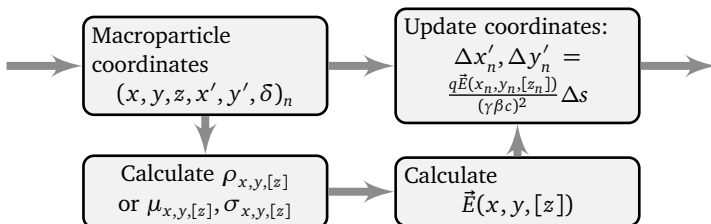


Figure 5.3: Flowchart of the space charge module of the simulation. Longitudinal fields are neglected, the $[z]$ is needed for bunched beams to take the transverse field variation over the bunch length into account.

Coasting Beams

For coasting beams, the calculation of transverse space charge is reduced to a 2D problem: In absence of longitudinal current fluctuations, the beam profile is independent of the longitudinal coordinate. For simulations with analytic fields, the

beam position μ_i and transverse dimensions σ_i are computed independently of the longitudinal coordinate of the macroparticles.

For simulations with self-consistent fields, the transverse density of the beam is interpolated onto the grid independently of the longitudinal particle position. The transverse fields on the grid are calculated as described above and the particle momentum coordinates are modified accordingly. In space charge simulations for this work, the space charge effect is calculated about 12 or more times per betatron period to ensure that the average field seen by the particles during betatron oscillation is giving a reasonable value.

Bunched Beams

In bunched beams, the transverse density depends on the longitudinal position of the particles. Generally for the beams of interest in this thesis, the longitudinal motion is very slow (the frequency of betatron oscillations is typically 10^5 as high as the synchrotron frequency, allowing to separate the two). Furthermore, the bunches are long compared to their width. For use of analytic equations for the space charge force, one can compute μ_i and σ_i as well as the local longitudinal density ρ_z as a function of z . Space charge can then be taken into account by applying the analytic electric field corresponding to a bi-Gaussian charge density with corresponding parameters.

The code for bunched beams relies on self-consistent simulation: The particles are interpolated on a three dimensional grid consisting of a number of two dimensional grids as described above aligned equidistant in the z direction with a spacing of Δz_{grid} at positions z_o (see Figure 5.4). These transverse grids are commonly called *slices*. For calculation of particle density one modifies Equation 5.4 to include the longitudinal direction:

$$\rho(x_m, y_n, z_o) = \frac{q_{\text{macro}}}{\Delta z_{\text{grid}} \Delta x_{\text{grid}} \Delta y_{\text{grid}}} \sum_{j=0}^{N-1} S_{2\text{D}} \left(\frac{x_j - x_m}{\Delta x_{\text{grid}}}, \frac{y_j - y_n}{\Delta y_{\text{grid}}} \right) S \left(\frac{z_j - z_o}{\Delta z_{\text{grid}}} \right). \quad (5.9)$$

The transverse fields are then calculated individually for each slice. The interpolation back onto the particles is done following a version of Equation 5.8 extended to three dimensions analogous to Equation 5.9. This approximation neglects longitudinal components of the fields which, due to the length of the bunch, only weakly depend on the transverse dimensions and can therefore be included by an impedance approach.

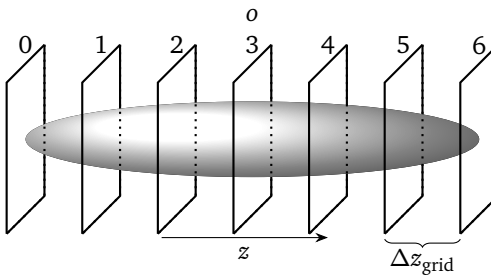


Figure 5.4: Illustration of longitudinal slicing. The actual slice number chosen in simulation for this work was between 16 and 512. For each of the particles in the bunch, its transverse density is linearly interpolated on the two neighbouring slices.

5.1.4 Beam-Beam Effect

For this work, a model of the beam-beam effect was implemented and added to the code. In the simulation code the beam-beam effect was modelled as a single interaction between the particles of each beam and the two-dimensional transverse fields of the interacting bunch. The reduction to two dimensions is justified by the bunch length in RHIC $\sigma_z \simeq 0.45$ being smaller than of the beta function at the IP $\beta^* \simeq 0.85$, thus only neglecting a betatron phase advance of $\pm 0.085\pi$ (Equation 3.7) during the collision. This was common practice in beam-beam simulation codes for a long time [78, 79]. More modern codes [28] allow the simulation of the full three dimensional interaction, but the additional computational effort is primarily introduced to allow the reproduction of the hourglass effect and crossing angle effects on the beam-beam parameter [80]. The influence of both of these can be considered negligible for the purpose of this work due to the small crossing angle and matched round Gaussian distributions with nearly equal β^* in both planes and both rings at RHIC. For this reason the substantial effort needed for implementation and simulations with a full three-dimensional model was deemed too high for the application in this work, especially after good agreement with experimental data could be shown early on for the two dimensional model.

For the implementation of the beam-beam effect, the simulation code was parallelized on a bunch level. Each of the processes simulating the particles of a bunch tracks the particles belonging to the bunch around the ring. When the simulated bunch arrives at the location of a beam-beam interaction, the transverse charge density of the bunch is discretized as described above. Attention is paid to choose

the same discretization in both bunches. The discrete electric fields corresponding to the transverse charge density are computed and exchanged with the partner bunch via MPI. A diagram of a beam-beam interaction in simulation is shown in Figure 5.5. The contribution of the magnetic field due to the relative velocity of the bunches is

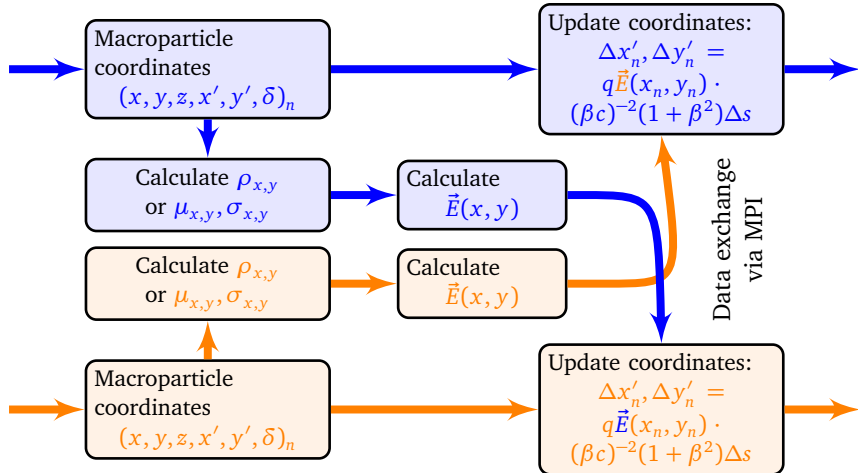


Figure 5.5: Flowchart of the beam-beam effect module of the simulation. Two processes (symbolized by yellow and blue color for the two rings in RHIC) arrive at an interaction point and exchange field data via MPI for simulation of the beam-beam effect. After the beam-beam interaction, both processes continue simulation independently. The interaction is reduced to a 2D-interaction between the transverse charge distributions of the bunches.

taken into account according to Equation 3.44. The particle momentum coordinates are modified according to the colliding bunches' electric fields interpolated at the particle location. The beam-beam effect and the electron lenses respectively present the major nonlinearity to beams interacting with them. For this reason, the particle transport between beam-beam interactions is modelled as a single transfer matrix obtained from the numerical model of RHIC (S. Tepikian, personal communication, April 2012) with the help of the MAD-X [74] code. The beam pipe diameter at the IPs in RHIC in the STAR and PHENIX detectors, 76.2 mm [81] and 40 mm [82] respectively, is orders of magnitude larger than the beam size (≈ 0.15 mm) justifying vacuum boundary conditions for the computation of the fields.

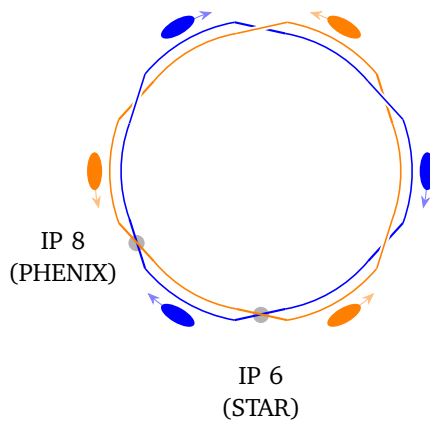


Figure 5.6: Illustration of the geometry of RHIC with the collision points at IP 6 and IP 8 (where STAR and PHENIX are located) marked. The electron lenses are located at IP 10. Depending on the filling scheme, sets of either two or six bunches are coupled by the beam-beam interaction.

Multiple Beam-Beam Interactions

In RHIC, the particles can interact at six equidistant possible interaction points as indicated in Figure 5.6. In normal operation, the beams only interact in two of the possible interaction points, namely in the STAR and PHENIX detectors. As a result of the geometry for normal operation, bunches form groups of six (three from each beam) such that the bunches from a group only interact with other bunches from the group via the beam-beam interaction. The geometry of RHIC and with the two interaction points in question indicated shown in Figure 5.6. In the simulation, the interaction between these bunches was implemented by running sets of six simulation processes exchanging electromagnetic field data upon interaction according to the scheme in Figure 5.7. The primary computational effort of the simulation is spent on the Beam-Beam interaction, therefore after every second interaction, the processes spend some time waiting until the next partner bunch arrives at the same time step. The simulation with six bunch processes can therefore be run on only three times the number of cores needed for one process without notable increase in wall clock simulation time.

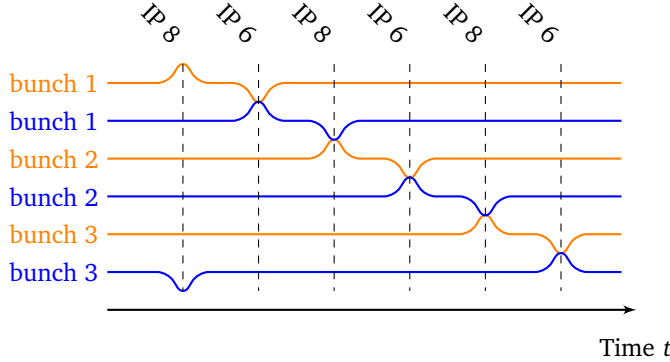


Figure 5.7: Illustration of the order of the collisions during one turn. Note that each bunch always meets the same partner in the same interaction point.

5.1.5 Electron Lens

For this work, the model of the electron lens was added to the simulation code: The electron lens is designed to deliver a Gaussian charge distribution. In simulation it is implemented by adding the total momentum change due to the fields of a Gaussian charge distribution (Equation 3.33) to the x' and y' coordinate of the particles respectively. The momentum change is applied once per turn at the location of the lens. For elliptic beams, the Bassetti-Erskine formula [58, 62] for the transverse forces F_x, F_y by a two-dimensional elliptic Gaussian distribution with σ_x, σ_y the RMS widths in the two transverse directions is used:

$$F_x + iF_y = \frac{nr_0}{\gamma} \sqrt{\frac{2\pi}{\sigma_x^2 + \sigma_y^2}} \left(w\left(\frac{x + iy}{\sqrt{2(\sigma_x^2 - \sigma_y^2)}}\right) - \exp\left(-\frac{x^2}{2\sigma_x^2} - \frac{y^2}{2\sigma_y^2}\right) w\left(\frac{\frac{\sigma_y}{\sigma_x}x + i\frac{\sigma_x}{\sigma_y}y}{\sqrt{2(\sigma_x^2 - \sigma_y^2)}}\right) \right) \quad (5.10)$$

with w the complex error function:

$$w(z) = e^{-z^2} (1 - \text{erf}(-iz)). \quad (5.11)$$

LIBCERF [83] was used to provide a fast implementation of the complex error function for use in the simulation code.

5.2 Beam Transfer Functions

This work focuses on investigations of baseband beam transfer functions, which can be measured with exceptional signal to noise ratio using direct diode detection systems (see Section 4.1). For this work, models of the BTF were added to the simulation code. In RHIC, typical bunch lengths are below 1 metre. With a machine length of 3.8 km, the phase of an excitation signal of a kicker driven in the baseband at $Q_{\text{frac}} = 0.68$ only changes by less than $0.68 \cdot 3800^{-1} < 0.0001\pi$ over the length of the bunch and can be neglected. Similar arguments can be made for other high energy machines. Therefore in the implementation of the BTF the kicker is implemented as a lattice element that changes the momentum coordinate of the particles as a function of time,

$$\Delta x' = A \cdot a(t), \quad (5.12)$$

wherein A is an arbitrary excitation amplitude and $a(t)$ is the BTF driving amplitude. $a(t)$ can either be chosen as an excitation at a specific frequency $\Omega = 2\pi Q_{\text{frac}}$ so that:

$$a(t) = \sin(\Omega t) \quad (5.13)$$

or as a band-limited white noise excitation such that

$$a(t) = \sum_{i=0}^{N_{\text{freq}}} \sin(\Omega_i t + \phi_i). \quad (5.14)$$

with Ω_i random frequencies from the frequency interval of interest and ϕ_i random phases from $[0, 2\pi]$. Each turn the offset of the transverse centre of charge of the bunch with respect to the reference trajectory $\langle x \rangle(t)$ is stored together with the kick amplitude $a(t)$. In postprocessing, $\hat{a}(\Omega)$ and $\langle \hat{x} \rangle(\Omega)$ are calculated by means of a discrete time Fourier transform [84], yielding the BTF via Equation 4.1. We implemented both methods but in this document only simulations with single frequency excitation are presented because experience showed them to be less noisy at the same computational cost.

In simulations with fixed excitation frequencies, the particle distribution is reset between subsequent excitation frequencies to avoid transient effects from the previous excitation [28, 85]. In measurement, similar behaviour can be achieved by waiting for the previous excitation to decohere. In this work the BTF were simulated with equidistant steps in excitation frequency. Since the particle distribution is reloaded before each frequency step, this allows for code parallelization: the

excitation at different frequencies can be parallelized such that several frequency samples are simulated at the same time on different CPUs.

One has to avoid changing the particle distribution as a result of the BTF excitation while still obtaining a good signal to noise ratio. As a rule of thumb in this work the response amplitude of the motion of the beam centre of charge was kept smaller than 1% of the RMS width of the unperturbed beam to avoid perturbing the particle distribution.

5.3 Validation

The various approximations necessary to make the code run on a manageable amount of computing power require careful validation of the implemented effects by means of comparison to analytically accessible scenarios. For this work, the implementation was validated against well-known results from literature, all of which were presented in Chapter 3 and Chapter 4. Validation examples can be found in the following subsections.

5.3.1 Beam Transfer Function

The perfect validation example for the BTF implementation are coasting beams with a Gaussian velocity profile and chromaticity as the sole source of tune spread. The case was discussed analytically in Chapter 4, the analytic expectation for the BTF shape can be found in Equation 4.10. For beams with betatron tune spread from chromaticity, the frequency spread σ_ω is given by the RMS momentum spread δ and the chromaticity ξ_{chrom} as $\sigma_\omega = 2\pi\delta \cdot \xi_{\text{chrom}} f_0$. Simulation and analytic expectation agree as shown in an exemplary BTF in Figure 5.8.

5.3.2 Space Charge

BTFs with space charge and can be validated on the analytic expectation for BTFs with coasting beams: In the presence of space charge, coasting beams result in BTFs as described in Section 4.4. Figure 5.9 shows exemplary simulated BTFs in comparison to the analytic expectation for beams with different space charge parameters U_{sc} . Simulation and analytic expectation agree.

5.3.3 Beam-Beam Effect

For head-on beam-beam interactions of two bunches in one interaction point, the positions of the π and σ modes are known analytically [66] and were discussed

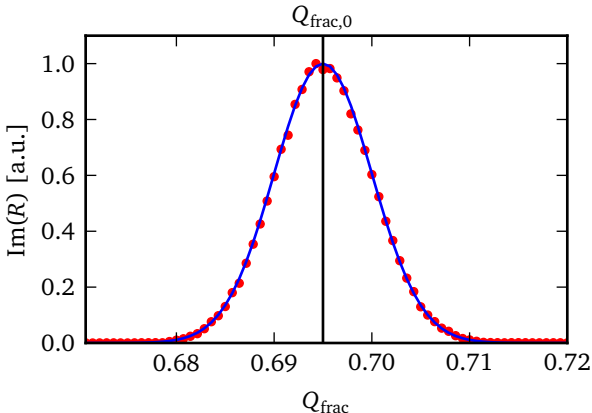


Figure 5.8: Comparison between simulated BTF (dots) and analytic expectation (line) for a beam with Gaussian velocity profile and chromaticity as the sole source of tune spread. The small discrepancy can be attributed to the granularity of the macroparticle distribution.

in Subsection 3.2.2. Furthermore, the tune shift of the π mode with respect to the σ mode is known to depend on the implementation of the interaction: BTFs in simulations using the assumption of a transverse Gaussian distribution using the analytic equations from Equation 3.33, are expected to show a mode separation $\Lambda = 1.103\xi$ [86]. Simulations using transverse fields corresponding to the discretized beam particle distribution arrive at a mode separation consistent with Equation 3.51 of $\Lambda = 1.215$. Validating plots for both scenarios can be found in Figure 5.10. Additional quantities used for validation of the implementation of both the beam-beam effect and the electron lens but not shown explicitly in this chapter were the tune distribution of the particles, and analytic expectation for the transverse field strengths. The implementation was in agreement with the analytic expectation for all of these.

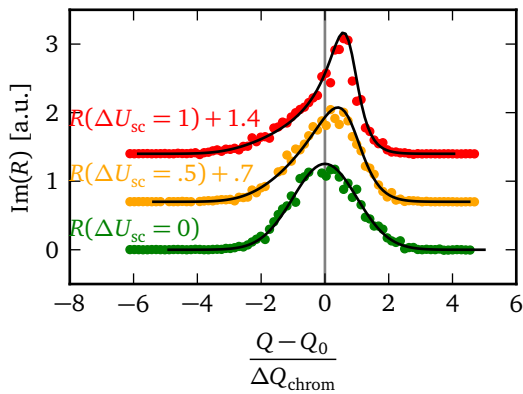


Figure 5.9: Imaginary part of simulated BTFs (dots) showing good agreement with analytic expectation (continuous line) for beams with different space charge parameters. The real part (not shown) also agrees. Deviations can be attributed to the granularity of the macro particles and decrease with increasing macroparticle number.

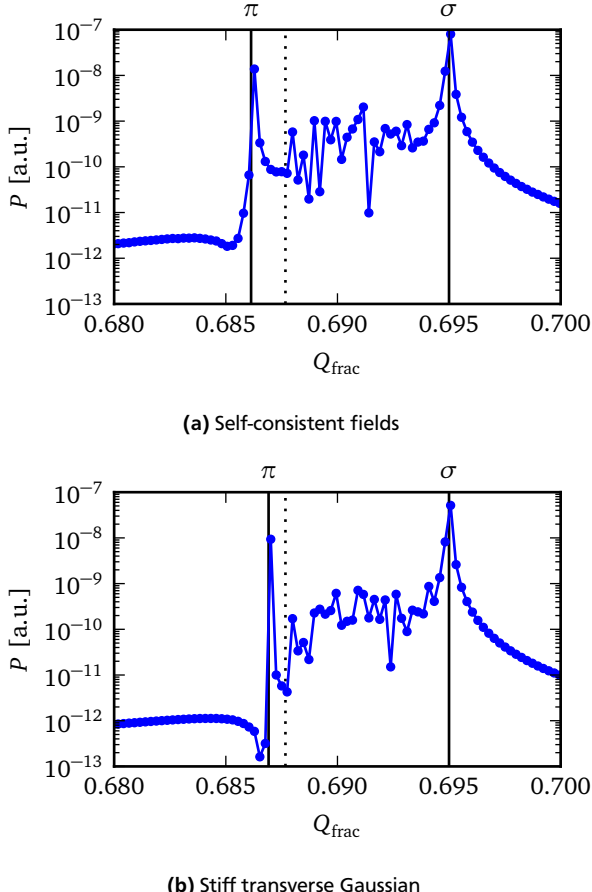


Figure 5.10: Validation of the beam-beam implementation: Power spectral density P of transverse beam oscillations over 4000 in simulated beams with one beam-beam interaction in RHIC. The π mode position is analytically expected to be shifted by 1.215ξ with respect to the σ mode for a model with self-consistent fields [66] and by 1.103ξ for a stiff transverse Gaussian model [86]. The dashed line indicates the beam-beam parameter ξ , the left limit of the incoherent particle distribution. Both models replicate the analytic expectation for the coherent mode frequencies.

6 BTFs of Bunched Beams with Space Charge

For bunched beams interacting with transverse nonlinearities such as an electron lens, there is no dependence of the interaction strength on the longitudinal particle coordinate. However, when discussing space charge, the transverse field amplitude at the location of the particles scales with the local bunch current density.

Previous discussions of BTFs of beams with space charge focused on coasting beams. In coasting beams, the magnitude of the transverse space charge is constant along the beam. Secondly, BTFs show peaks for coherent modes such as the synchrotron satellites introduced by bunching. Previous research shows that in the presence of space charge the coherent mode frequencies shift in a characteristic way [21, 22, 23].

For this investigation an intermediate regime was chosen: In high energy accelerators, the synchrotron period is frequently several thousand turns long (e.g. between 10^3 and 10^4 turns in SIS100). When measuring the BTF for a time span shorter than one synchrotron revolution, the BTF is unable to resolve the coherent modes and one might expect a more coasting-beam like behaviour.

To asses this assumption, an analytic expectation for the beam transfer functions of bunched beams with frozen synchrotron motion in the presence of space charge is presented in Section 6.1. Its implications for tune measurements are discussed and it is validated against simulation data. Section 6.2 shows the breakdown of the assumption of frozen synchrotron motion on simulated BTFs with increasing synchrotron frequency and argues that the model is applicable to BTF measurements taken over a timespan below the synchrotron period. Section 6.3 discusses the feasibility of recovering the magnitude of space charge from BTF measurements of bunched beams.

6.1 BTFs of Bunched Beams with Frozen Synchrotron Motion

The analytic expectation for BTFs of coasting beams with space charge (Equation 4.27) is the starting point for the treatment of a bunch with frozen synchrotron motion. For this reason it makes sense to revisit it here:

$$R_{\text{sc}}(\Omega) = \frac{R(\Omega)}{1 - (\Delta U_{\text{coh}} - \Delta U_{\text{sc}} + i\Delta V_{\text{coh}})R(\Omega)}. \quad (4.27 \text{ revisited})$$

For frozen longitudinal motion ($Q_s = 0$) the BTF of the whole bunch can be described as a superposition of the coasting beam BTFs of longitudinal slices of the beam of length dz . The longitudinal slices have a local space charge parameter ΔU_{sc} which is defined by the space charge parameter $\Delta U_{sc,max}$ at maximum bunch current j_{max} and the local bunch current $j(z)$ via:

$$\Delta U_{sc}(z) = \Delta U_{sc,max} \frac{j(z)}{j_{max}}. \quad (6.1)$$

With this local space charge the BTF of a bunched beam with frozen synchrotron motion can be expressed as an integration over the contribution of the longitudinal slices with their individual transverse space charge parameters.

$$R_{sc,bunched}(\Omega) = C \int_{z_{min}}^{z_{max}} R_{sc} \left(\Omega, \Delta U_{sc,max} \frac{j(z)}{j_{max}} \right) j(z) dz, \quad (6.2)$$

with C being a normalizing factor. For practical purposes this discussion is restricted to the case of beams in absence of transverse impedances whereby $\Delta U_{coh} = \Delta V_{coh} = 0$. This is permissible without loss of generality as their influence on the BTF (Equation 4.27) is identical to that of ΔU_{sc} . The resulting BTFs are similar to the ones for the coasting beam. Figure 6.1 shows a comparison between the analytic expectation $R_{sc,bunched}$ for bunched and R_{sc} for coasting beams. The stronger the space charge the more obvious the difference: While in the bunch the maximum space charge parameter varies between 0 and $\Delta U_{sc,max}$ for different longitudinal locations, all the particles in the coasting beam see the same space charge parameter ΔU_{sc} . This results in narrower peak for the coasting beam BTFs when compared to the bunched beam BTFs.

As can be seen in Figure 6.1, the peak in the BTF becomes *narrower* as the space charge (and with it the tune spread from longitudinal sources) increases. At the same time the peak width increases with increasing tune spread from chromaticity. Unlike for the case of tune spread from localized transverse sources such as an electron lens (Chapter 7), there is no direct correlation between the peak width and the total tune spread.

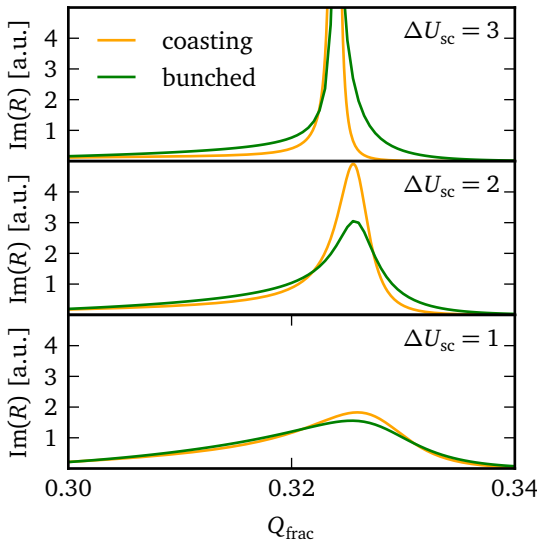


Figure 6.1: Comparison between BTFs for coasting beams with transverse space charge (Equation 4.27) and bunched beams with transverse space charge (Equation 6.2) for different transverse space charge parameters of the coasting beam ΔU_{sc} and the bunched beam $U_{sc,max}$ respectively and otherwise identical beam parameters. The example beam has $Q = 0.32$, $\Delta Q_{chrom} = 0.01$ and $\Delta Q_{sc,[max]} \in [.01, .02, .03]$ in the different plots.

6.1.1 Implications for Tune Measurements

In everyday operation, BTFs are frequently used to measure the tune: often the peak of the betatron sideband is assumed to coincide with the tune for automated tune measurements. With increasing space charge, the peak of the BTF shifts away from the actual tune distribution within the beam. Using the BTF peak to control the machine tune without accounting for this difference can result in particle tunes accidentally crossing a resonance line. Emittance growth and particle losses can be the result. For beams without space charge, the peak position in the BTF and the tune distribution coincide. BTFs with and without space charge together with the expected tune footprints are shown in Figure 6.2. As can be seen for a moderate space charge parameter of $\Delta U_{sc,max} = 1$ one already misjudges the position of the tune distribution by ΔQ_{chrom} when assuming the particle tunes to be centered around the BTF peak. As a guide to the eye, the peaks of the BTF and the tune distribution $\psi(Q)$ are indicated. Note how with increasing space charge parameter the assumption that the peak in the BTF coincides with the peak of the tune distribution breaks down. It should also be noted that the tune distribution and the BTF peak are shifted in opposite directions with respect to the lattice tune Q_0 . This shift should be taken into account when measuring the lattice tune via the BTF.

6.1.2 Simulation

For validation of the analytic prediction with the help of simulated BTFs, the energy of the simulated beam is set to the transition energy. On transition $\eta = 0$ (Equation 3.27) and consequently the synchrotron frequency (Equation 3.14) becomes zero, synchrotron motion freezes. For a beam under these conditions BTFs can be expected to be described by Equation 6.2. Figure 6.3 shows simulated BTFs and the analytic expectation for different space charge parameters. The results are in good agreement for typical space charge parameters. For space charge parameters higher than $\Delta U_{sc,max} > 3$, a slight broadening of the peak in simulation with respect to the analytic expectation was observed. This is likely an effect of limited simulation resolution and could be overcome by increasing the resolution of the space charge simulation by introducing more longitudinal slices and simultaneously increasing the particle number.

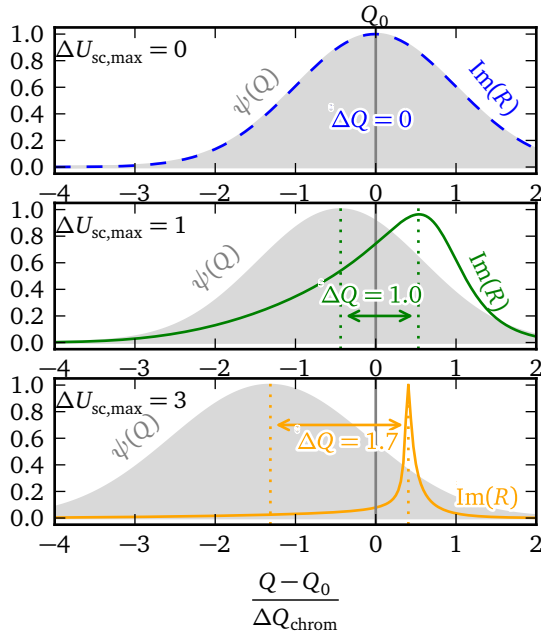


Figure 6.2: The imaginary part of the BTF $\text{Im}(R)$ and the tune distribution ψ for different values of the bunches charge parameter $\Delta U_{\text{sc},\text{max}}$. For a bunch with no space charge ($\Delta U_{\text{sc},\text{max}} = 0$) the $\text{Im}(R) \propto \psi$. For increasing space charge parameters, the two move away from each other. To correctly judge the location of the tune spread with respect to the working point, one has to account for the tune difference ΔQ between the BTF peak and the peak of the betatron tune distribution.

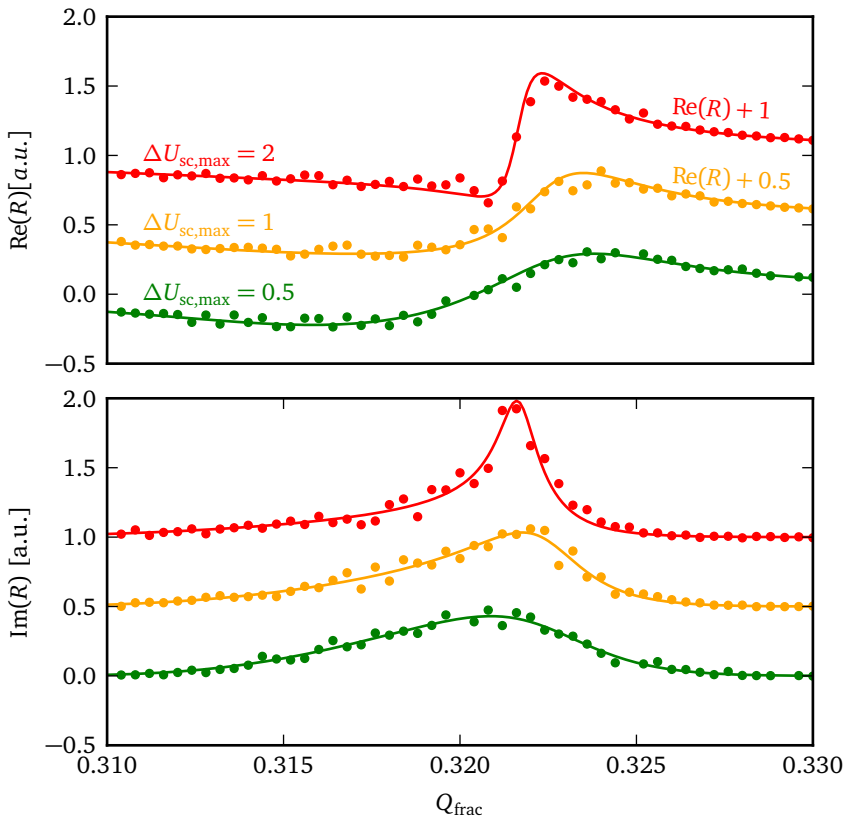


Figure 6.3: Simulated BTFs (dots) and analytic expectation (line) for bunched beams with frozen synchrotron motion and different space charge parameters. The space charge parameter $\Delta U_{sc,max}$ is given in the figure. The BTFs for different $\Delta U_{sc,max}$ are offset with respect to each other. Offsets are given in the plot. The colour code and offsets are the same for both plots. The simulation agrees with the analytic expectation.

6.2 Finite Synchrotron Frequencies

In a real machine beams cannot survive for long on transition energy [6, 62], and efforts are taken to cross transition energy as fast as possible during acceleration or avoid crossing it altogether [87, 88]. For beams that are not exactly on transition, but with reasonably small η as is the case in high energy machines, synchrotron motion is still slow. In real life BTF systems the time for taking a frequency sample is often of the order of magnitude of the synchrotron frequency. For example in RHIC with a synchrotron period of about 30 ms the measurement time for one BTF frequency sample is also about 30 ms. In SIS100 with synchrotron tunes between 10^{-3} – 10^{-4} , the synchrotron period can be as long as 10^4 turns. The BTF will not be able to resolve the synchrotron satellites if their tune difference is less than the number of turns corresponding to the measurement time of a BTF frequency sample ¹ N_{turns}^{-1} . Furthermore aside of the resolving power of the BTF in terms of frequency the synchrotron motion leads to a periodic oscillation of the individual particles betatron frequencies. The combination of these effects was studied in simulated BTFs. The goal of these simulations being to assess the range of parameters for which the model of frozen synchrotron motion can be used to describe the BTF. In doing so the assumption that BTFs measured with a measuring time per frequency sample of less than one synchrotron period will not show synchrotron satellites of the betatron sidebands to can be tested.

Validation for Bunched Beams with Chromaticity

As a first validation example, simulated BTFs of a bunched beam with chromaticity and no other effects were chosen. For the simulation a tune of $Q = 0.32$ was chosen for a bunched beam with a Gaussian velocity profile and a tune spread due to chromaticity of $\Delta Q_{\text{chrom}} = 0.005$. To investigate the limit of the frozen bunch model, the BTF of a beam on transition with $Q_{\text{syn}} = 0$ is compared with that of a beam of $Q_{\text{syn}} = 0.001$. The two BTFs can be expected to show negligible difference as long as the simulated measurement time per frequency sample is shorter than the synchrotron period of 1000 turns. Starting from a measurement time per frequency sample of 1000 turns the synchrotron satellites should be resolved by the BTF. The results are shown in Figure 6.4. They confirm the expectation: As soon as the BTF measurement time exceeds the synchrotron period of 1000 turns, the synchrotron satellites show up in the simulated BTFs. Until then, the simulation with frozen synchrotron motion, the analytic expectation for the coasting beam (black line) and the simulation with synchrotron motion agree. To reproduce these results in

¹ This is because the frequency resolution of the discrete time Fourier transform is $f_{\text{sampling}}N^{-1}$ with f_{sampling} the sampling frequency and N the number of samples.[84]

measurements one has to make sure that sufficient time for the coherent excitation to decohere is left between measurements of subsequent BTF frequency samples.

Validation for Bunched Beams with Chromaticity and Space Charge

Simulations for BTFs of bunched beams with chromaticity and space charge show that for example beams with moderate space charge with BTF measurement times above the synchrotron period² when the synchrotron satellites should in principle be resolvable, the BTF can still be described by Equation 6.2 with no coherent modes appearing. The reason is likely that in the case of chromaticity as the only source of tune spread, particles return with the same betatron phase after completing one synchrotron oscillation. Thus, after one synchrotron revolution particles excited upon the previous passing oscillate in phase with the BTF driving signal and their contribution to the coherent signal is observed in the BTF. The phenomenon is called recoherence [89, 90]. With an amplitude dependent tune shift such as the one from space charge, the decoherence of the particles with respect to each other reduces the signal amplitude of the recoherence signal over time. This reduces the effect of recoherence and likely accounts for the fact that even for relatively long measurement times of the BTF no appearance of coherent synchrotron satellites is observed in simulations with moderate synchrotron frequencies.

As a result we consider it safe to assume that for BTF measurement times below the synchrotron period the BTF should resemble Equation 6.2.

6.3 Determining the Space Charge Tune Shift

For bunched beams with frozen synchrotron motion and space charge in combination with chromaticity as the source of tune spread, the BTF shape strongly depends on both space charge and chromaticity. There seems to be no simple relation between the BTF and the tune spread introduced by the combination of space charge and chromaticity. The only method left to us to determine the space charge tune shift from the BTF under these conditions is fitting of BTF data against analytical expectation. For practical purposes this means parametrizing Equation 6.2 via the variables $\Delta U_{sc,max}$, C and Ω_0 and determining $\Delta U_{sc,max}$ by means of a least squares fit. This method was used by others in the past for evaluation of BTFs of coasting beams with space charge [48].

Equation 6.2 was fitted against simulated BTF data under the assumption of Gaussian beams (Gaussian distributions in both the transverse and longitudinal directions). The fits undertaken using the Levenberg-Marquardt method available

² Example beam: $\Delta U_{sc,max} = 1$, $\Delta Q_{chrom} = .0032$, $Q_s = 0.001$, simulated BTF measurement time $3T_s$

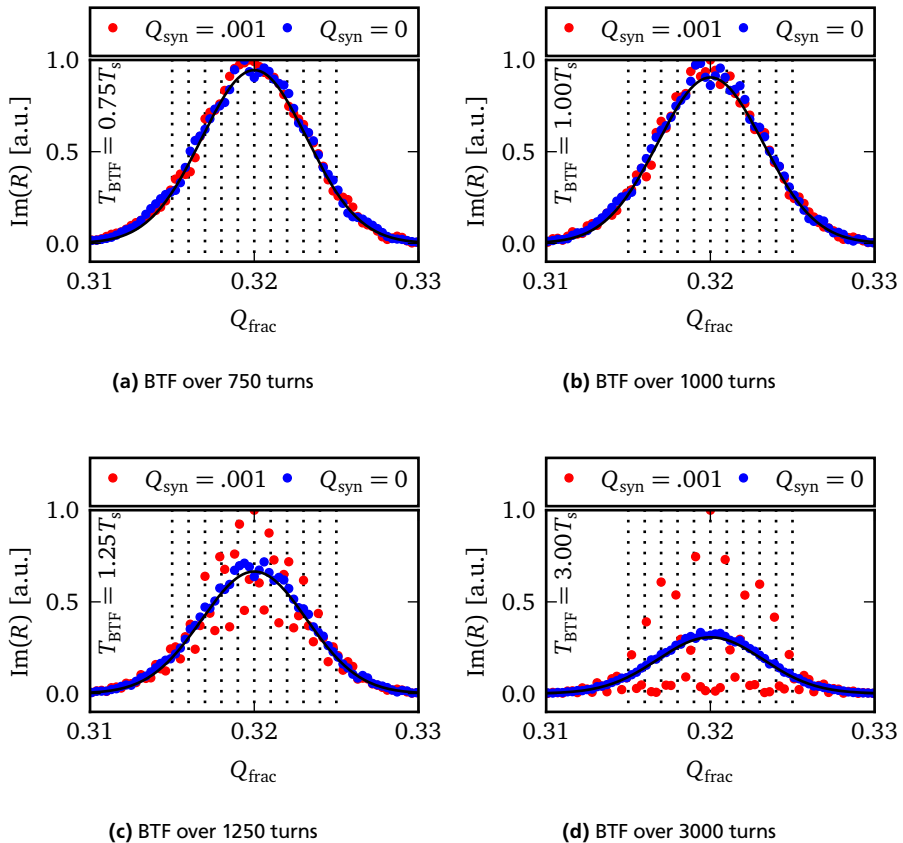


Figure 6.4: Transition between the validity of the frozen synchrotron motion model and the appearance of the synchrotron satellites in simulated BTFs. The black line is the analytic expectation for a beam with frozen synchrotron motion. The positions of the synchrotron satellites for the beam with $Q_{\text{syn}} = 0.001$ are marked by the dashed vertical lines. When the BTF covers more than one synchrotron period (more than 1000 turns for the chosen synchrotron tune), the synchrotron satellites appear, for longer BTF measurement times they are resolved with increasing resolution.

in the python package `scipy` [91] recover the space charge parameter used for simulation input with an accuracy of about 10%. The error is attributed to the noise introduced by the particle granularity in simulation.

Nevertheless this cannot be considered a promising method for everyday measurement of space charge. To derive the space charge tune shift from the $\Delta U_{\text{sc},\text{max}}$ recovered by fitting, one needs to know ξ_{chrom} , a quantity which is frequently not known with sufficient accuracy in everyday operation. Furthermore the analytic model is restricted to beams where single particle tunes are dominated by space charge and chromaticity. No difficulty is expected for extension of the model for other sources of tune spread. However, for recovery of the magnitude of space charge effects from a BTF one would have to have knowledge about the magnitude of all other sources of tune shift to disentangle their influence on the BTF from the influence of space charge. It is much easier to calculate the space charge tune shift directly from beam current measurements in connection with the emittance measurements via Equation 3.42.

7 Using BTF to Measure Tune Spread

As a possible application of the measurement of the transverse BTF in presence of an electron lens, the recovery of the tune distribution of a beam interacting with an electron lens was chosen. With this in mind the BTF of a beam interacting with a local transverse nonlinearity as the primary source of tune spread had to be studied in detail. This chapter presents the results of these studies. First the properties of the BTF are investigated phenomenologically in Section 7.1. Subsequently it is shown that the recovery of the tune distribution is not possible in Section 7.2. Finally, it is discussed how instead of the shape of the tune distribution at least the width of the tune spread can be recovered in Section 7.3.

7.1 BTF Phenomenology

For this application of the expected the beam transfer function, the goal was the recovery of the tune distribution $\psi(Q_x, Q_y)$ with Q_x, Q_y the horizontal and transverse betatron tunes in presence of a transverse nonlinearity. Alternatively, the determination of $\psi(Q_x)$ and $\psi(Q_y)$, the projections of the tune distribution onto the x and y axes, seemed desirable. To better understand properties of the transverse beam transfer functions it makes sense to revisit Equation 4.26:

$$R_x(\Omega) = \frac{\langle x \rangle}{f_x(t)} = C \cdot \iint_0^\infty dJ_x dJ_y \frac{J_x}{\Omega - \omega_x(J_x, J_y)} \frac{\partial \psi_0}{\partial J_x} \quad (4.26 \text{ revisited})$$

ψ_0 is a density and therefore $\psi \in \mathbb{R}_0^+$. Also, $\psi_0 = 0$ for $J_x, J_y \rightarrow \infty$. $\omega_x(J_x, J_y) \approx \Omega$ is continuous. In Equation 4.1 a similar integral in absence of transverse nonlinearity was solved. If R_x has an imaginary part it stems from the denominator of the fraction

$$\frac{J_x}{\Omega - \omega_x(J_x, J_y)} \quad (7.1)$$

going to zero for J_x, J_y where $\omega_x(J_x, J_y) = \Omega$. Furthermore unlike in the case with an out-of plane source of tune spread, not the density ψ but its derivative $\partial \psi / \partial J_x$ times the particle action J_x contribute to the integral. Therefore regions with a high derivative can be expected to contribute strongly to $\text{Im}(R)$ and the contribution of

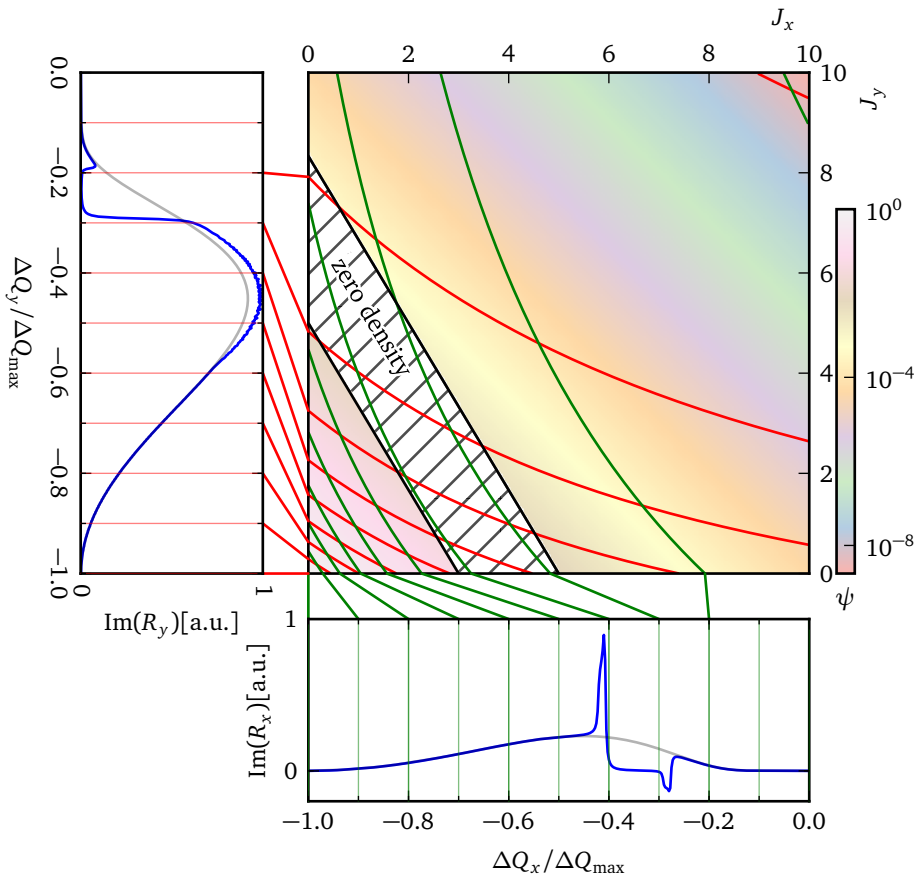


Figure 7.1: Example of the relations between phase space density and the resulting BTF: A hypothetical particle distribution in J_x, J_y space is shown as a density plot. The density distribution ψ is that of a Gaussian beam of the form $\exp(-J_x - J_y)$ in terms of J . It was modified by setting ψ to zero for $3 < J_x + 0.6 \cdot J_y < 5$ in order to generate a hole in phase space. Green and red lines denote contours of equal tune shift in x and y direction. Their tune shift values can be found via the connection to the tune axes of the BTF. The resulting BTF in x and y for the beam interacting with a Gaussian charge distribution of the same size are calculated numerically and are shown to the bottom and to the left of the density plot. Figure published in [92].

particles to scale with their action J_x . A visualization of the phase space density which was published in the framework of this thesis in [92] is shown in Figure 7.1.

The figure shows the expected properties: BTF for the distribution with hole (blue) and the normal Gaussian distribution (grey) are shown in comparison: For the maximum tune shifts found at very small J_x , the pole contributes only little to $\text{Im}(R)$. The imaginary part of the BTF resulting from this is very small as can be seen in the plots of the horizontal and vertical BTF. The edges of the hole contribute differently to the horizontal and vertical BTF: In the horizontal BTF, the edges are parallel to equitune lines and therefore the large derivative at the edge of the hole leads to a sharp peak in the resulting BTF. In the area corresponding to the hole, the BTF becomes zero. At the right edge of the hole the derivative in the opposite direction leads to a negative peak in $\text{Im}(R)$. The BTF then follows the BTF of a normal Gaussian distribution again. The vertical BTF is influenced differently. In a tune shift range of $\Delta Q_y / \Delta Q_{\max} \in [-0.2, -0.3]$, the contribution of the derivative at the right edge of the hole cancels the contribution of the distribution further to the right. Then in $\Delta Q_y / \Delta Q_{\max} \in [-0.3, -0.55]$, one edge of the hole partly compensates the other and from $\Delta Q_y / \Delta Q_{\max} = 0.55$ on only the centre of the beam with Gaussian particles distribution contributes, the BTF is identical to that of a beam with Gaussian distribution.

7.2 Recovery of Tune Distributions

Further investigating the relationship between BTF and the particle tune distribution, it became apparent that the knowledge of only the BTF is insufficient to determine the tune distribution: This is easiest to understand for a beam of constant density in J_x, J_y phase space: For such a beam, $\partial \psi / \partial J_x$ is 0 everywhere but at the edge. Thus no conclusion on the tune distribution apart from its edge is possible. It was first shown in the framework of this thesis in [92] that the reconstruction of the tune distribution is impossible for the case of flat beams, the arguments are repeated in this section.

7.2.1 Flat Beams

To escape the complications of the full 2D nonlinear case, a very flat beam distribution $\psi(J_x, J_y)$ that is introduced. The real world equivalent could for example be a beam of very low vertical emittance. Let the flat beam be defined by

$$\psi(J_x, J_y) = \begin{cases} \varepsilon^{-1} \psi_x(J_x), & J_y < \varepsilon \\ 0, & J_y \leq \varepsilon \end{cases} \quad (7.2)$$

and assume ε to be sufficiently small that $\omega_x(J_x, 0) - \omega_x(J_x, \varepsilon) \ll \Delta\omega$ or in words, that the horizontal amplitude dependent frequency shift on the interval $J_y \in [0, \varepsilon]$ is much smaller than the total tune spread in x direction (and the same for the y direction). In the following the horizontal and transverse BTF are calculated.

Horizontal BTF

The integrand does not show J_y dependency, therefore Equation 4.26 directly simplifies to:

$$R_x(\Omega) = c \int_0^\infty \frac{1}{\Omega - \omega_x} J_x \frac{d\psi}{dJ_x} dJ_x \quad (7.3)$$

Substituting $\omega_x \rightarrow u$ and assuming invertible $\omega_x(J_x)$ wherever $d\psi/dJ_x \neq 0$ and therefore the existence of $J_x(\omega_x)$. Inserting $dJ_x = (dJ_x/du)du$ yields:

$$R_x(\Omega) = c \int_{\omega_{\min}}^{\omega_{\max}} \frac{1}{\Omega - \omega_u} J_x \frac{d\psi}{du} du \quad (7.4)$$

An equation of this form was already encountered in Equation 4.8 and therefore can be simplified directly to:

$$R_x(\Omega) = c \int_{\omega_{\min}}^{\omega_{\max}} \frac{1}{\Omega - u} J_x \frac{d\psi}{du} du + i\pi \cdot c J_x(\Omega) \frac{d\psi}{d\omega}(\Omega) \quad (7.5)$$

with P.V. the principal value integral. Attention should be given to the imaginary part of R_x :

$$\text{Im}(R_x(\Omega)) = c \pi J_x(\Omega) \frac{d\psi}{d\omega}(\Omega) \quad (7.6)$$

If $J_x(\omega_x)$ is known, this allows us to recover ψ by integration of $\frac{d\psi}{d\omega}$ over ω . Unfortunately $J_x(\omega_x)$ is normally unknown, especially in machines with transverse nonlinearities from different sources. Furthermore, in cases where $\omega(J_x)$ is known, the horizontal frequency distribution can be assessed without measuring BTFs, by just measuring $\psi(J_x)$ for example by means of an ionization profile monitor and translating it to frequency by means of $\omega(J_x)$.

Vertical BTF

The vertical BTF is given by:

$$R_y(\Omega) = c \iint_0^\infty \frac{1}{\Omega - \omega_y(J_x, J_y)} J_y \frac{d\psi}{dJ_y} dJ_y dJ_x. \quad (7.7)$$

It can be solved with similar ease. Equation 7.2 results in:

$$\frac{d\psi}{dJ_y} = -\psi_x \delta(\varepsilon - J_y) \quad (7.8)$$

with δ the dirac delta function. The J_y integration therefore gives:

$$R_y(\Omega) = \varepsilon c \int_0^\infty \frac{1}{\Omega - \omega_y(J_x, \varepsilon)} \Psi(J_x) dJ_x \quad (7.9)$$

which finally results in

$$\text{Im}R_y(\Omega) = \varepsilon c \psi(\Omega) \frac{dJ_x}{d\omega_x}(\Omega). \quad (7.10)$$

With knowledge of $J_x(\omega_y)$ this result would be useful. Unfortunately the same arguments as above apply and $J_x(\omega_y)$ is not known. These considerations show us that even for a flat beam, it is not possible to reconstruct the tune distribution solely from the BTF. Consequently a method of recovering the tune distribution from BTF applicable without prior knowledge can be excluded.

7.3 Thresholds

Having established that reconstruction of the tune distribution is not possible, it makes sense to revisit Equation 4.26

$$R_x(\Omega) = C \cdot \iint_0^\infty dJ_x dJ_y \frac{J_x}{\Omega - \omega_x(J_x, J_y)} \frac{\partial \psi_0}{\partial J_x} \quad (4.26 \text{ revisited})$$

to see what useful information might still be extracted. It is important to stress the argument first put forward in the framework of this thesis in [92]: Since all involved functions are real and their integrals are finite, $R_x(\Omega)$ will be real if for all J_x, J_y

either $J_x d\psi/dJ_x = 0$ or $\omega_x(J_x, J_y) - \Omega \neq 0$, because in these cases no singularity contributes to the integral. Thus:

$$\forall J_x, J_y : \frac{d\psi}{dJ_x} \vee \Omega - \omega_x(J_x, J_y) \neq 0 \Rightarrow \text{Im}(R_i(\Omega)) = 0 \quad (7.11)$$

negating this expression one arrives at:

$$\text{Im}(R_x)(\Omega) \neq 0 \Rightarrow \exists J_x, J_y : J_x \frac{d\psi(J_x, J_y)}{dJ_x} \neq 0 \wedge \omega_i(J_x, J_y) = \Omega. \quad (7.12)$$

Therefore it can be concluded [92]: Wherever the $\text{Im}(R_x(\Omega)) \neq 0$, there must be particles with $\omega_x = \Omega$ and $J_i d\psi/dJ_x \neq 0$. Neglecting points with $\psi = 0$ and $J_i d\psi/dJ_x \neq 0$ one can say: Wherever $\text{Im}R_x(\Omega) \neq 0$ there are particles at J_x, J_y with $\omega_x(J_x, J_y) = \Omega$. However it does not follow that there are no particles where $\text{Im}(R) = 0$, it might just be that the phase space derivative at J_x, J_y is zero but the density is not.

An additional complication arises in the case of measured or simulated BTF, even BTF calculated numerically with finite accuracy: $\text{Im}(R)$ will never be exactly zero: in simulation the granularity of the macroparticle distribution presents a source of noise, in measurements the electronics add noise to the signal. To accommodate for this fact one can introduce a threshold t and instead of demanding $\text{Im}(R) = 0$ be satisfied with $|\text{Im}(R)| < t$. This allows to adjust t to compensate for unwanted contributions from noise. Depending on the BTF to be examined, it can be beneficial to modify the condition to demand $|\text{Im}(R)| < t|R|$.

7.3.1 Choice of Thresholds

To make thresholds comparable, it makes sense to normalize the BTF with their peak value and apply the threshold to $R_{\text{max}}(|R|)^{-1}$ instead of R . As a result thresholds used can be compared directly independent of the arbitrary amplitude of the input BTF and are always indicated as a fraction of the maximum BTF value at the betatron peak.

Noise in Measurement

In measured BTF the noise is introduced by the electronics: Even with the improved signal to noise ratio due to the direct diode detection method, a noise background is observed in measured BTF. Furthermore damping from sources other than the tune spread may play a role, for example damping coupled in from the other transverse plane, or via the beam-beam interaction from the other beam. A

method for determination of the threshold was developed in this thesis and first introduced in [92]: To determine a reasonable threshold one chooses a frequency interval of the BTF which can safely be considered as noise dominated, in the most cases this is just a frequency interval in a region that can safely be considered as not containing any single particle tunes. One then calculates

$$a_{\text{noise}} = \max(|\text{Im}(R)|) \quad (7.13)$$

as the noise amplitude. The threshold t can then be set to a chosen multiple r of that value, in this work $r = 1.5$ is used. Increasing r leads to a smaller proportion of the actual particle tune spread being recovered (because for some frequencies, the Landau-damping from the particle tunes that is present still falls short of the threshold). Decreasing r increases the risk of mistakenly considering part of the noise as particle tunes. In simple terms, r adjusts the sensitivity of the threshold method.

7.3.2 Recovered Tune Spreads and Beam-Beam Parameters

While other methods recover the beam-beam parameter ξ_{bb} (the peak tune shift due to the beam-beam effect), the threshold method recovers frequencies with incoherent particle tunes. As a measure for the tune spread, the width of the region where the threshold condition is satisfied can be used. Furthermore with a nonzero threshold the condition only becomes true for a part of the actual tune spread. The aim is to translate between the tune spread recovered from the threshold method (the width of the area where $\text{Im}(R) > t$ or $\text{Im}(R) > t|R|$) and the corresponding beam-beam parameter ξ_{bb} . Since tune spread will primarily be arising from matched transverse Gaussian distributions for the case of the beam-beam effect and electron lenses, Equation 4.26 can be calculated numerically, and from it the threshold dependence of the recovered tune spread. Putting it together one arrives at what can be seen in Figure 7.3. Figure 7.2 shows the threshold method applied to the analytic BTF (Figure 4.4). Figure 7.3 shows how the detected tune spread changes as a function of the used threshold. To make the factor determined using the relation representative, normalized BTF can be used ($R/\max(|R|)$), whereby the thresholds become comparable and are always represented as a fraction of the peak BTF amplitude.

7.3.3 Thresholds and Coherent Beam-Beam Modes

A prerequisite for the application of the threshold method for the detection of tune spread is that the distribution of incoherent particle tunes dominates the BTF

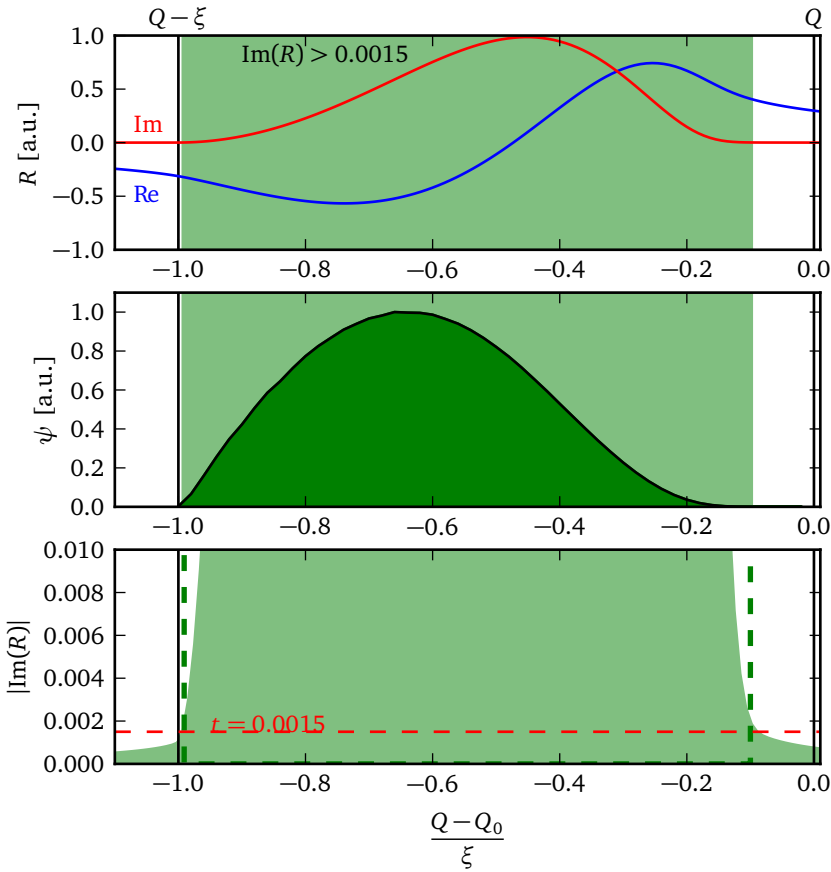


Figure 7.2: The threshold method applied to the BTF from Figure 4.4. The chosen threshold was 0.0015, the tails visible in the magnified plot of $\text{Im}(R)$ stem from the numerical solution with a_{noise} set to the numeric accuracy of the integration in MATHEMATICA [93] of 0.001. The integral was solved on $0 < J_{x,y} < 20$.

as is the case for a beam interacting with a localized electron lens. This is not the case anymore when dealing with beam-beam interactions which produce coherent beam-beam modes (section 3.2.2). While a priori it is clear that the BTF of a beam in presence of coherent beam-beam modes will differ from the analytically accessible

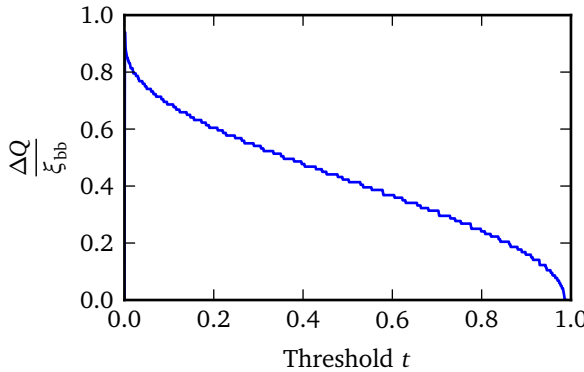


Figure 7.3: The threshold dependence of the tune spread ΔQ returned by the threshold method for the BTF of a round Gaussian beam interacting with a round Gaussian charge distribution of matched transverse dimensions (as shown in Figure 4.4 and Figure 7.2 respectively).

case of a beam dominated by the incoherent tune spread, this does not necessarily mean that the threshold method is useless. From the discussion of the incoherent BTF above it is known that a nonzero imaginary part to the BTF is expected in the regions of incoherent particle tunes. At the frequencies of the coherent modes a response of the beam can be expected and correspondingly $\text{Im}(R) > 0$. However there is no reason to expect that the coherent modes suppress the imaginary part of the BTF given rise to by the incoherent tune spread. Therefore the incoherent tune spread might still be visible in the BTF. The main motivation in proposing the second variant of the threshold method above ($|\text{Im}(R)| < t|R|$) was to limit the influence of the coherent beam-beam modes by normalizing the imaginary part of R by the absolute value of R everywhere. It could then become possible to identify the coherent modes and gain knowledge about the tune spread from the remaining BTF. Simulation results were promising, an example is shown in Figure 7.4. Note how even in presence of the dominating coherent modes, the incoherent tune spread is clearly visible in $\text{Im}(R)/|R|$. After identification of the π and σ modes the tune spread seems to correspond well to the shaded region where $\text{Im}(R)/|R| > t$.

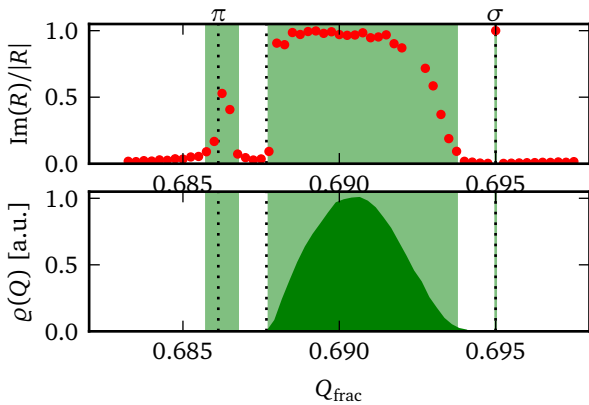


Figure 7.4: Threshold method applied to simulated BTF of a beam with nominal RHIC tunes and coherent beam-beam oscillations. The analytically expected positions for the π and σ modes as well as for the left edge of the tune spread are indicated by dashed lines. $\text{Im}(R)/|R|$ and the tune distribution $\varrho(Q)$ calculated from particle trajectories are shown. The threshold used was 0.07.

8 Measurement with the Threshold Method

The threshold method introduced in Chapter 7 was successfully applied to simulated BTFs of electron lenses and seemed promising for application in real-life measurements. This chapter discusses its application to measured BTFs obtained in experiments designed to replicate the beam dynamics in presence of an electron lens. The first measurements for this work at RHIC took place in the proton runs 2012 and 2013. This was prior to the installation of the electron lenses. To replicate the conditions seen by a beam interacting with an electron lens in absence of the actual device, the beam-beam effect was used as a stand-in for the electron lens. As discussed in Subsection 3.2.2, unlike the electron lens, the beam-beam effect causes coherent modes through interaction between the bunches of the two rings. For typical RHIC conditions these modes dominate the BTF because of their amplitude. In this chapter, Section 8.1 discusses the measures put in place to avoid coherent modes. Section 8.2 discusses the effect of synchrotron motion for the experiment and argues that it can be neglected based on simulation data for the planned measurement conditions. With the prerequisites outlined, Section 8.3 emphasizes additional constraints by the RHIC accelerator and discusses the setup and expected results of a BTF measurement taken in the 2013 RHIC proton run. Section 8.4 discusses the results of the measurement and discusses them with respect to the expectation. The application to an actual electron lens is shown in Section 8.5 with promising results. Finally the application of the threshold method to beams with coherent beam-beam modes can be found in Section 8.6 and indicates that the method is not applicable in presence of coherent beam-beam modes.

8.1 Weak-strong Beam-Beam Interaction as a Stand-in for the Electron Lens

To better approximate the transverse dynamics of a beam interacting with an electron lens by means of the beam-beam effect and get rid of beam-beam specific results, two measures seemed promising:

Tune Splitting

By operating the two rings on different working points, the bunches can be made to return to the interaction points with different betatron phase changes. The resulting offset in transverse phase results in a shift of coherent modes. Predictions by Alexahin [94] showed that the shift can be sufficient to Landau damp the coherent modes inside the incoherent spectrum. However the Landau-damping can result in a deformation of the BTF.

Intensity Splitting

When beams of different intensity collide, the intensity difference leads to a shift in the π mode towards the incoherent spectrum. For beams with an intensity ratio larger than about two, [94] predicts that the π -mode enters the incoherent spectrum and becomes Landau damped.

To assess the effect of a combination of tune and intensity splitting on the BTF, the situation was first studied in simulation. To minimize the influence of the weak beam on the strong beam, an intensity ratio of 1:10 was chosen. Simulation for the measurement conditions showed BTFs for two beams interacting head-on were in agreement with BTFs of beams interacting with the transverse Gaussian charge distribution corresponding to the electron lens and the analytic expectation for the same machine conditions as shown in Figure 8.1. This made us confident that the measurement conditions would be suitable to reproduce BTFs as are to be expected for an electron lens.

8.2 Influence of Bunching

The theory in Equation 4.26 is valid for coasting beams, it only takes into account transverse motion. Its application for bunched beams in RHIC is justified by the fact that the sampling time of the BTF system roughly equals the synchrotron period and therefore the BTF should barely be able to resolve synchrotron motion. Furthermore the tune spread due to chromaticity is very small in comparison to the beam-beam tune shifts: with $\delta_{\text{rms}} = 2 \cdot 10^{-4}$ and $\xi_{\text{chrom}} = 0 - 6$ as typical values for RHIC at high energy, the maximum tune shift due to chromaticity is less than $1 \cdot 10^{-3}$ while the tune shift due to the beam-beam effect is typically of the order of 10^{-2} . To validate this simplification, simulations for coasting beams and bunched beams with synchrotron motion were carried out and the resulting BTFs were compared. For the parameters given in Table 8.1 no significant deviation of the BTFs of coasting and bunched beams were observed. Therefore it can be considered safe to use Equation 4.26 to describe bunched beams in typical high energy synchrotrons with compensated chromaticity and the resulting low chromatic tune spread. In presence

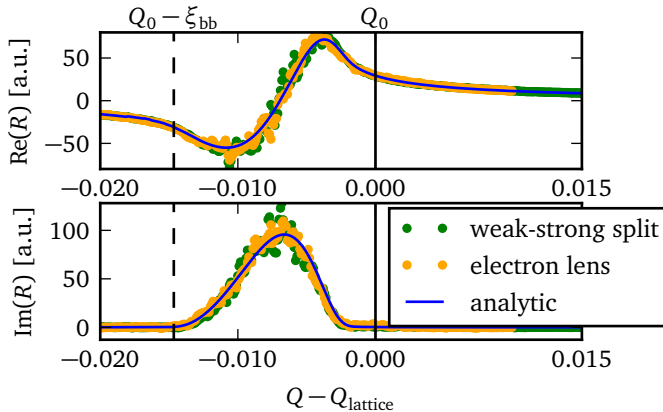


Figure 8.1: Simulated BTFs: BTFs of the weak beam in interactions of two beams with an intensity ratio of 1:10 with split tunes are compared to simulated BTFs of a beam interacting with an electron lens and the analytic expectation according to Equation 4.26.

of higher chromatic tune spread or significantly higher synchrotron frequency it is recommendable to check the validity of the coasting beam theory for the bunched beam in question on simulated BTFs. The findings are also consistent with simulation results for space charge, where no synchrotron satellites of the betatron sidebands for BTF measurement times up to about 4 synchrotron periods were observed.

Table 8.1: Simulation parameters for the evaluation of the assumption of coasting beams in beams with low synchrotron frequency and low chromaticity. For these parameters no notable dependence of the shape of the BTF in dependence of synchrotron frequency was observed. Typical RHIC high energy proton parameters are shown for comparison.

	RHIC	Simulation
Chromaticity	$\approx 0 - 6$	0-6
Momentum spread	$\approx 2 \cdot 10^{-4}$	$2 - 8 \cdot 10^{-4}$
BTF sample time	≈ 30 ms	30-50 ms
Synchrotron period	≈ 30 ms	15 ms, 30 ms, coasting

8.3 Experimental Setup

The experiment had to adhere to peculiarities of the RHIC system and was planned as follows: Each ring was filled with 28 bunches. The blue ring was filled with bunches of nominal intensity. The yellow ring was filled with 22 bunches of 1/10 of the nominal intensity and another 6 bunches of nominal intensity. A cartoon of the filling scheme can be found in Figure 8.2. The bunches of nominal intensity in the yellow ring were necessary in order to permit acceleration without beam loss: The tune feedback system that is needed for acceleration is not sensitive enough to operate reliably on the low intensity bunches. Failure of the tune feedback likely causes dumping of the beam by the interlock system. The small amount of beam time shared by the beam physics experiments does not permit for unnecessary beam dumps and thus the six safety bunches were added to the setup.

Furthermore to reach a good signal to noise ratio for the BTF in normal operation at RHIC, the BTF system measures the combined BTF of all bunches. As a result the BTF given by the system is the sum of the BTFs of all bunches combined (BTF are additive). Standard mode BTFs on the yellow beam for this setup will therefore present us with a superposition of the BTFs of the weak bunches and the BTFs of the strong bunches. There would be no way for us to disentangle the incoherent signal of the weak bunches from the strong bunches. To avoid this problem after an initial BTF on all bunches of the yellow beam the operating mode of the BTF system was changed such that a time gating only allowed the signal from the weak bunches to contribute to the BTF signal.

Some more thought has to be spent on the superposition: The injector chain does not perfectly reproduce the beam parameters for the injected bunches. Therefore the intensity of the bunches in both beams varies by 10%. As a result, the beam-beam parameter of the individual bunches of the blue beam varies by the same amount (which defines the tune shift seen by the bunches of the yellow beam).

After filling both rings, the beam was accelerated to 100 GeV. The beams were brought into collision in the interaction points of the STAR and PHENIX experiments. BTF 1 was measured. The transverse beam profile of the strong beam was measured and the emittance was calculated from it. The BTF system was switched into gated mode, such that only the BTF of the weak bunches in the yellow ring were measured. BTF 2 was measured. The beams were moved out of collision in the interaction point at the PHENIX experiment. BTF 3 was measured. The tunes of the machines were separated. BTF 4 was measured.

The expected results are as follows

BTF 1 Is not gated. It is dominated by the strong-strong bunches and as a result it should show coherent beam-beam modes. The positions of these modes

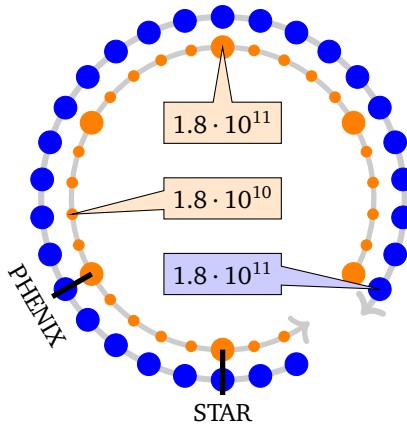


Figure 8.2: Bunching scheme for the experiment (first presented in [92]). The measurement for electron lens like conditions was done using gated BTF on the low intensity bunches in the yellow ring. The 6 high charge bunches are necessary to provide intensity for tune feedback on the ramp. They were also used to determine the beam-beam parameter via the π and σ mode positions for the strong-strong collisions.

can be used to determine the beam-beam parameter. The σ -mode position is independent of the bunch parameters and should therefore be quite exactly at the lattice tune for all bunches, the π mode might vary slightly with bunch intensity. The peak at the π mode will be broadened accordingly.

- BTF 2** Includes only weak bunches interacting in two interaction points. The expectation is that the beam-beam parameter matches the one from BTF 1. The σ mode might be visible at the lattice tune.
- BTF 3** The weak bunches are now interacting only in one interaction point. It can be expected that the beam-beam parameter is half that observed in BTF 1 and BTF 2. The σ mode might be visible at the lattice tune.
- BTF 4** The tunes are now split. The beam-beam parameter can be expected to match that of BTF 3. All coherent modes should have moved inside the incoherent spectrum.

Intuitively and in accordance with simulation and experience at BNL, one expects the BTFs of beams interacting in two interaction points to exhibit twice the tune

spread and beam-beam parameter of beams only interacting in one interaction point.

8.4 Experimental Results

The experimental results obtained in measurements at RHIC on fill #17355 and #17356 (the latter being a virtual fill number) to a good extent match the expectation.

Determination of the Beam-Beam Parameter from Coherent Mode Positions

In BTF 1 coherent modes in the vertical plane are observed. This is common at RHIC [95] and explained by coupling of Landau-damping between the planes. Figure 8.3 shows the BTF in the yellow ring in the vertical plane. The beam-beam parameter corresponding to the tune difference of $\Delta Q = 0.19$ between the π and σ modes corresponds to a beam-beam parameter of

$$\xi_{\text{bb}} = \frac{\Delta Q}{\Lambda} = 0.17 \quad (8.1)$$

when assuming round beams. The result stays accurate even for elliptical beams: The change of Λ (Equation 3.51) for beams of aspect ratios between 0.3 and 0.7 only results in a maximum change of 3% in Λ and consequently in $\Delta \xi_{\text{bb}}$, therefore the determined beam-beam parameter can be expected to be quite accurate. Broadening of the π mode due to bunch current variation was observed within the expected limits, taking into account the fact that sets of six bunches couple in each measurement. If the relative error of the charge of one bunch is 10%, the average charge in these sets only varies by 4%. The frequency source of the BTF system is sufficiently accurate to disregard the possible error in frequency.

Determination of the Beam-Beam Parameter via Emittance Measurement

Measurements of the transverse emittances of the blue beam by means of beam profile monitors suggest a round beam ($\varepsilon_x = 14.3 \mu\text{m}$ and $\varepsilon_y = 13.1 \mu\text{m}$) emittances¹. The beta function at the location of the beam profile monitor at the time of this measurement is inaccurate because no measurement of the beta beat (the deviation of the beta function) for the measurement conditions was available, the uncertainty of the β function dominates the uncertainty of the transverse emittance measurement. The beta function enters calculation of the emittance from the transverse profile according to $\varepsilon_x = \frac{\sigma_x^2}{\beta_x}$. Consequently with an uncertainty of 20% of

¹ Normalized 6 σ emittances, see Equation 3.12

the β_x at the beam profile monitor, the resulting emittance also has an expected error of 20%, which propagates to the beam-beam parameter inaccuracy. The beam-beam parameter calculated via the emittance and the particle number by means of Equation 3.50 is: $\xi_x = 0.0094$ in the horizontal and $\xi_y = 0.0098$ in the vertical direction. When the beams are interacting in two IPs, the beam-beam parameter during the two interactions accumulates to $2\xi_x = 0.0189$, $2\xi_x = 0.0197$.

The error is dominated by the systematic error of the emittance measurement and assuming uncorrelated errors in ε_x and ε_y of 20%, the total error of the resulting beam-beam parameters is inaccurate by about 16%. In presence of additional error sources, the beam-beam parameter would become even more inaccurate. Within the given accuracy, the value for the beam-beam parameter calculated from the blue emittances agrees with the one from the coherent mode positions. The more accurate value for the beam-beam parameter determined via the coherent beam-beam modes will be used for the following consideration.

Determination of the Beam-Beam Parameter by Means of the Threshold Method

With two estimates for the beam-beam parameter, the threshold method can be applied to BTF 2–4 and the results can be compared. Because the beams in RHIC are assumed to be Gaussian, a third possible method is to try to determine

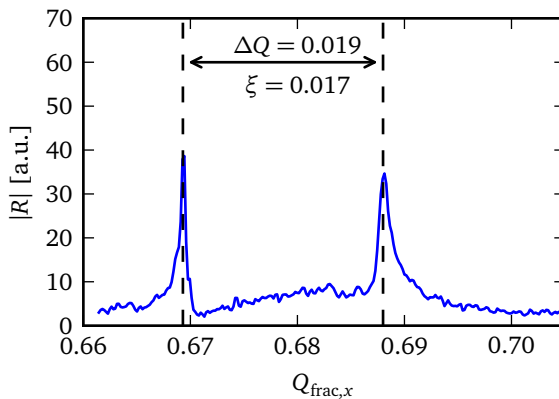
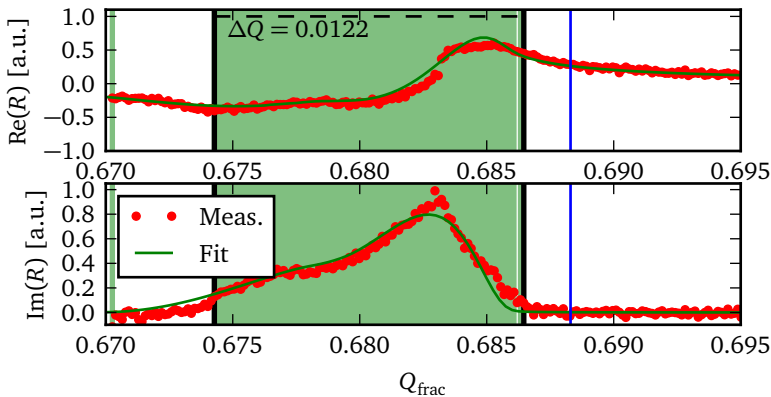


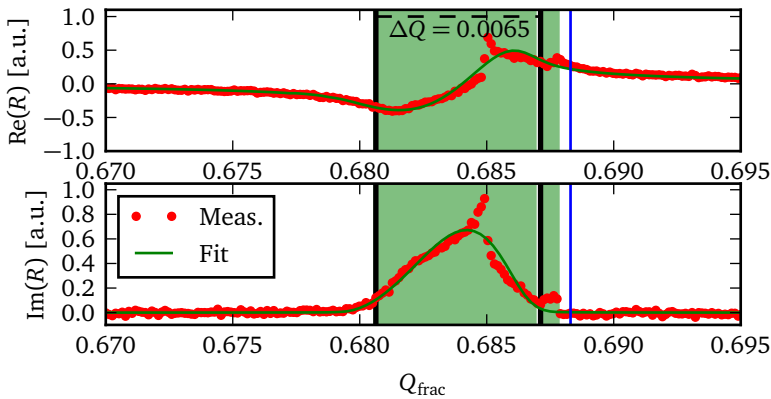
Figure 8.3: Coherent beam-beam modes as observed in the BTF on the yellow ring in the vertical axis. The indicated beam-beam parameter was calculated using the Yokoya factor (Equation 3.51) Λ for round beams, plausible aspect ratios result in $\xi_{bb}^{-1} \Delta \xi_{bb} < 3\%$

the beam-beam parameter by fitting Equation 4.26 for Gaussian beams against the BTF. The results in the horizontal plane (Figure 8.4) agree with the expectation: For BTF 2 both the threshold method and the fit return a beam-beam parameter of 0.0179 and 0.0178 respectively, in good agreement with the beam-beam parameter determined from the coherent mode positions (0.017 ± 0.0017). After separation, the beam-beam parameter determined from BTF 3 and BTF 4 (Figure 8.6) is still consistent with the expectation: The recovered tune spread is about half the value it was before reflecting the reduction of collisions in two IPs to only one IP. The values for the beam-beam parameter as determined by the different methods are listed in Table 8.2. The fits for the beams before separation were using a superposition of Equation 4.26 for two and one IP because the filling scheme above leaves two of the yellow bunches without a second collision partner. Whether or not a superposition is assumed does not significantly affect the recovered tune spread.

The weak BTFs (yellow beam) in the vertical axis (Figure 8.5) do not match the expectation: A total beam-beam parameter as high as 0.027 is unlikely in RHIC. Furthermore the yellow vertical BTF exhibits a multi-peak structure the origin of which is not clear. Nevertheless nearly the expected halving of the tune spread upon separation of the beams is observed, indicating a relation of the phenomenon to the beam-beam parameter. Furthermore the BTFs seem to be independent from the tunes of the blue beam, they do not change significantly upon splitting of the tunes (compare Figure 8.5b and Figure 8.6b). One possible explanation of the unexpected width of the peak in the imaginary part of the BTFs in the vertical direction is interplane coupling: Looking closely at the BTFs one notices that the BTFs in the vertical direction usually overlap those in the horizontal direction. Assuming part of the damping in the vertical plane is coupled in from the horizontal plane would explain both the broadening and the halving of the total width of the recovered tune spread.

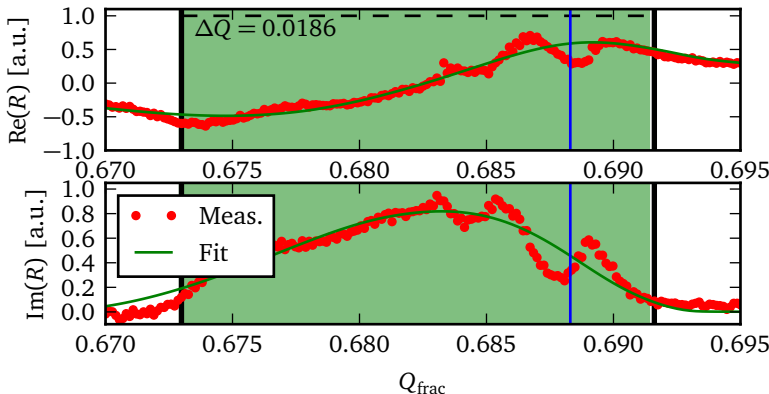


(a) Horizontal BTF 2 in the yellow ring and threshold tune width for beams colliding in two IPs

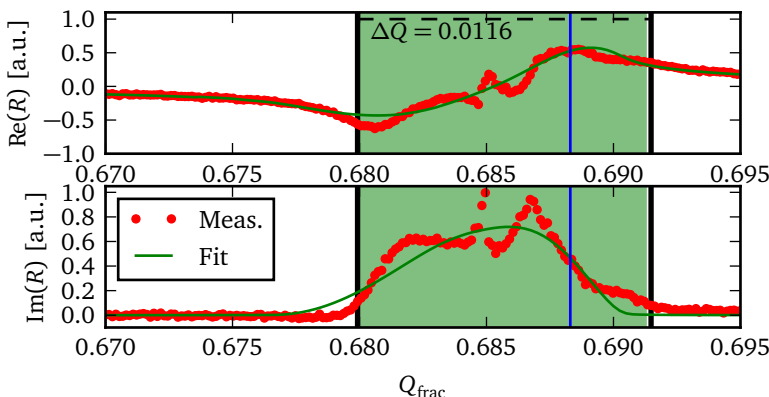


(b) Horizontal BTF 3 in the yellow ring and threshold tune width for beams colliding in one IP

Figure 8.4: Horizontal results for the width of the tune spread from the threshold method are given in the respective plots. The green area is where the threshold condition is fulfilled, the chosen threshold is 0.1. The blue line denotes the horizontal tune of the machine at the time of the measurement, the green line is a fit of Equation 4.26 to the data.

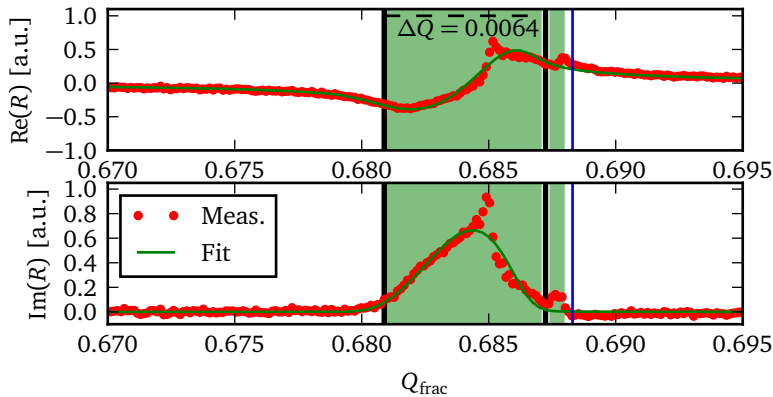


(a) Vertical BTF 2 in the yellow ring and threshold tune width for beams colliding in two IPs. No coherent σ mode is visible because the separation of the beams already split the tunes of the two beams by 0.02, sufficient to damp the coherent σ mode.

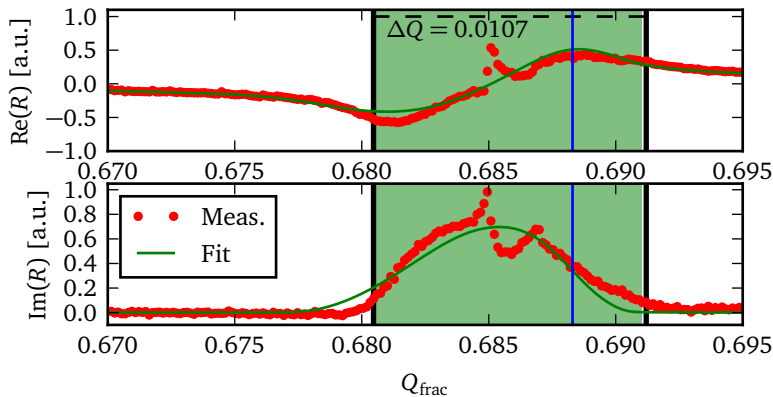


(b) Vertical BTF 3 in the yellow ring and threshold tune width for beams colliding in one IP

Figure 8.5: The green line is a fit of Equation 4.26 to the data. The green area is where the threshold condition is fulfilled, the chosen threshold is 0.1. The tune spread measured using this threshold is indicated in the plots. The blue line denotes the horizontal tune of the machine at the time of the measurement.



(a) Horizontal BTF 4 in the yellow ring and threshold tune width for beams colliding in two IPs and split tunes



(b) Vertical BTF 4 in the yellow ring and threshold tune width for beams colliding in one IP and split tunes

Figure 8.6: Horizontal and vertical results for the width of the tune spread from the threshold method are given in the respective plots. The green area is where the threshold condition is fulfilled, the chosen threshold is 0.1. The blue line denotes the horizontal tune of the machine at the time of the measurement, the green line is a fit of Equation 4.26 to the data.

Table 8.2: Beam-beam parameter calculated for the BTFs obtained using either fits against analytic expectation or the threshold method. ξ_y determined from coherent mode positions was 0.017 ± 0.003 . ξ_y determined from emittance and beam current measurements is $\xi_x = 0.019 \pm 0.004$. That ξ determined for BTF 2 should be equal ξ for BTF 1 and the ξ in BTF 3 and BTF 4 are to be expected to show half that value.

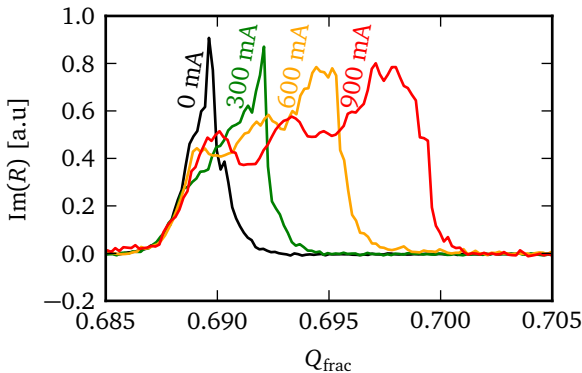
	BTF 2	BTF 3	BTF 4
$\xi_{x,\text{threshold}}$	0.0179	0.095	0.093
$\xi_{x,\text{fit}}$	0.0178	0.0093	0.0086
$\xi_{y,\text{threshold}}$	0.0273	0.0170	0.0157
$\xi_{y,\text{fit}}$	0.0275	0.0171	0.0156

8.5 Threshold Method Applied to an Actual Electron Lens

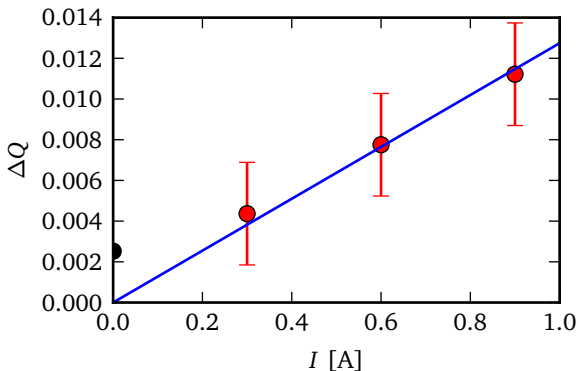
During 2015 RHIC proton, shortly before finalization of this document, first BTFs of proton beams interacting with the electron lenses were observed. The BTFs allow to validate the method in operation on an actual electron lens. BTF data measured on fill 18886 to determine the tune spread introduced by the electron lens were kindly provided by X. Gu and W. Fischer. The BTFs of beams in the yellow ring interacting with the electron lens were measured without electron lens (zero current) and with different electron lens currents. The tune spread introduced by the electron lens scales linearly with the electron lens current. The threshold method can be used to determine the tune spread introduced by the electron lens. The expected result is that the recovered spread increases linearly with the electron current. The BTFs are shown in Figure 8.7a. The evaluation using the threshold method to determine the tune spread was complicated by the fact that the zero current measurement also showed a significant spread. Since the source of the zero current spread is unknown it is unclear cannot know if it adds to or subtracts from the tune spreads of the electron lens or if the electron lens dominates the tune spread entirely. For that reason it is assumed assume that the tune spread for the zero current measurement represents an upper estimate for the error of the electron lens tune spread. The tune spreads recovered by the threshold method are shown in Figure 8.7b. Judging from the linearity of the three electron lens measurements, the zero current measurements as upper bounds for the electron lens peak width likely overestimates the error of the tune spread measurements. For the used threshold $t = 0.1$, the total tune spread seems to be dominated by the electron lens tune spread and the recovered tune spreads are quite linear, thus matching the expectation.

8.6 Threshold Method in Presence of Coherent Beam-Beam Modes

In Subsection 7.3.3 it was shown (Figure 7.4) that even in presence of coherent beam-beam modes, the tune spread could still be recovered from simulated BTF by means of the threshold method. Validation on BTF measured in 2015 on from fill 18771 unfortunately shows that the conditions in the real machine are not sufficiently perfect to replicate the simulation result. While it is possible to distinguish the features seen in the simulation (the π and σ modes and the incoherent tune distribution), the clear separation between the coherent modes and the incoherent tune spread is not observed. The exemplary BTF measurement on two beams colliding in IP 8 is shown in Figure 8.8. To allow comparison both $\text{Im}(R)$ and $\text{Im}(R)/|R|$ are shown. Neither of the two allows a reliable identification of the



(a) $\text{Im}(R)$ for different electron lens currents



(b) $\Delta Q(I)$ recovered from the BTFs for different electron lens currents with a threshold of 0.1, the blue line is a fit against $a \cdot I$, the error bars of the peak widths are equal to the zero current peak width, which was the only measure available for the actual error. The linearity of the fit suggests that this error greatly overestimates the actual error of the measurement.

Figure 8.7: Measurement of the BTF of a beam in the yellow ring interacting with an electron beam of constant width and different electron beam currents. The peak width scales linearly with electron beam current. (BTF data courtesy of X. Gu and W. Fischer.)

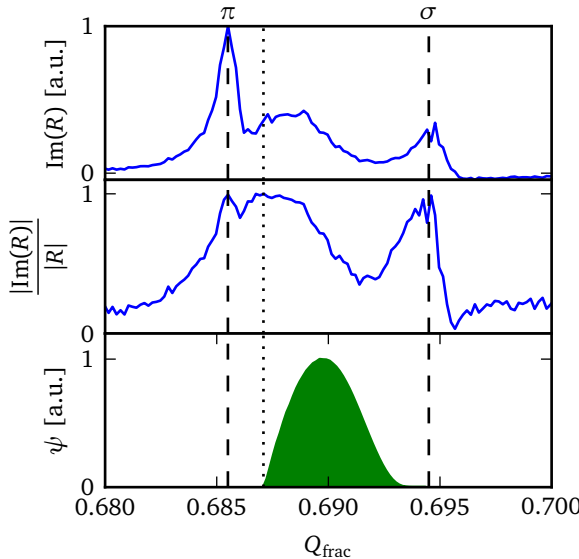


Figure 8.8: Measured BTF of the yellow beam in collision with the blue beam in IP 8. The π and σ beam-beam modes are marked. The beam-beam parameter calculated from their distance is marked by a dotted line. The tune distribution ψ calculated analytically under the assumption that the beam-beam effect and Gaussian beams are the primary source of tune spread is indicated. Compare with the simulated BTF for similar conditions (Figure 7.4). (BTF data courtesy X. Gu and W. Fischer.)

incoherent tune distribution. The tune distribution expected for Gaussian beams with the beam-beam parameter recovered from the coherent mode positions is shown in the bottom for comparison. While the coherent modes are easily identified, the incoherent tune spread cannot be separated by a threshold method from either $\text{Im}(R)$ or $|\text{Im}(R)|/|R|$.

8.7 Conclusions from the Measurements

The measurements results indicate applicability of the threshold method to beams in absence of coherent beam-beam modes. The theory does not rely on the specific shape of the single particle tune distribution and any sources of single particle

tune shifts contribute to the imaginary part of Equation 4.26. For this reason one can expect the threshold method to be applicable for any BTF dominated by the incoherent beam distribution. The simulations both in Section 4.4 and the parameter study in this chapter suggest that slow synchrotron motion with synchrotron periods of the order of the time for measurement of a single BTF frequency sample can be neglected, justifying a coasting beam model for the BTF.

In presence of coherent beam-beam modes the threshold method does not give a good estimate for the beam-beam tune spread any more. It can be considered reasonable to assume that the presence of coherent modes from other effects in the frequency range of the incoherent tune spread has a similar detrimental influence on the recovery of the incoherent tune spread from the BTF.

9 Conclusion and Outlook

Previous research allowed analytic description of BTFs of coasting beams in presence of space charge, chromaticity and other sources of tune spread [48, 71] and made it feasible to directly measure these quantities by means of the BTFs of coasting beams [48, 20]. Also BTFs of bunched beams with fast synchrotron motion were well understood, showing characteristic coherent modes with a space-charge dependent frequency distribution [21, 22, 23].

This work focuses on a new intermediate regime: in high energy hadron synchrotrons with bunched beams, both of the previously available descriptions break down for real-life BTF measurements: The coasting beam description assumes a DC beam and therefore fails to correctly describe effects due to the time-varying current of a bunched beam. The coherent modes arising from the longitudinal synchrotron motion are observable, but real-life BTF frequency samples are often measured for a time below or of the order of magnitude of the synchrotron period and therefore do not resolve the coherent mode frequencies.

This work closes a gap between the two regimes: For exemplary effects, the beam-beam effect, space charge and electron lenses, BTFs for bunched beams with slow synchrotron motion, commonplace in high energy synchrotrons, were described analytically.

The analytic expectation for the BTF of a beam with tune spread caused by a local transverse nonlinearity was presented in this work and shown to be adequate for the description of bunched beams with slow synchrotron motion interacting with an electron lens or another beam. The analytic result was validated against both simulation and measurement. As a possible application for the model, the determination of the betatron tune distribution, an important quantity determining beam life time, was chosen. On theoretical grounds it could be shown that the betatron tune distribution induced by transverse sources cannot be recovered from the BTF. However, while the shape of the distribution remains inaccessible, it was shown how by means of a chosen threshold at least its width can be recovered. This method was then applied to simulated and measured BTFs and it was shown that it yields an easy-to-automatize method for tune spread measurement in absence of coherent modes [92]. It was successfully applied for the measurement of the tune spread induced by an electron lens recently installed at RHIC.

For bunched beams with tune spread caused by space charge and chromaticity, the coasting beam model of the BTF was extended for this work to account for

the local variation of the magnitude of transverse space charge over the length of the bunch. The model was validated on simulated BTFs of bunched beams with frozen synchrotron motion. The breakdown of the model for increasing synchrotron tunes was investigated with the help of the simulation model. It was estimated analytically, and shown on simulated BTFs that coherent modes due to synchrotron motion appear when the sampling time for a BTF excitation frequency exceeds the synchrotron period. Below that measurement time, the presented analytic expectation holds. The model can therefore be considered applicable for most ion species in high energy synchrotrons (e.g. SIS100).

The description of the BTF in presence of space charge as was presented in this work is necessary for the correct interpretation of measured machine parameters: BTF measurements are the method of choice to determine the tune. In presence of space charge, the peak of the BTF does not coincide with the tune of the majority of particles but instead is found with an offset, depending on the magnitude of space charge. For beams with the incoherent space charge tune shift known from other sources such as beam current and emittance measurements, the offset can be predicted by means of the analytic model. This allows to account for the distortion introduced by the space charge tune shift and subsequently improves the accuracy of tune measurements. As a result the working point can be adjusted to avoid resonance lines and thereby preserve beam quality.

Further research could focus on the influence of impedances on the BTFs of bunched beams with space charge. The analytic results for BTFs of coasting beams with space charge, used as a starting point for the investigation of BTFs of bunched beams with space charge in this document, allow for its inclusion, but were here used in a simplified version by neglecting the influence of impedances.

Another possible starting point for future research is the investigation of the interplay between different sources of transverse tune spread, for example by investigating the BTF in the combined presence of both space charge, momentum spread, chromaticity and local transverse nonlinearities such as an electron lens. A possible application would be the prediction of the offset between the peak in the BTF and the tune distribution of the beam, allowing for a better choice of the working point.

Acknowledgements

I wish to thank Prof. Oliver Boine-Frankenheim. Aside from offering me the position at TEMF, he supported my work with constructive criticism and successfully guided me to use my strengths for the good of the work. Aside from the science he accepted and supported my work for the PhD representation. He also established the contact to Wolfram Fischer without which the work in its present state would never have taken place. I thank Wolfram Fischer for having been a great host and collaborator at Brookhaven National lab who, despite his tight schedule, always had an open ear and a creative suggestion. I thank both Prof. Thomas Weiland and Prof. Oliver Boine-Frankenheim for allowing me to extend my PhD time, enabling me to properly conclude the work after birth of my son Leif.

During my two visits to Brookhaven National Laboratory I met many inspiring and inspired people. By name I wish to thank Mike Blaskiewicz and Simon White for sharing their knowledge with me, not only but especially during the implementation of the beam-beam effect in the simulation code and for helping plan and carry out the measurements. Furthermore I wish to thank Yun Luo for his support with the measurements and everybody at Brookhaven who contributed to the measurements one way or another. Last but not least I wish to thank Yann Dutheil and everyone at BNL who made me feel welcome also in my free time.

The graduate school HGS-HIRe offered me additional training and financial support for travel. Without it I would have had much less opportunity to travel for my PhD project and present my work at conferences. With respect to conferences I also want to thank the European Physical Society and the Deutsche Physikalische Gesellschaft for financially supporting my participation in the International Particle Accelerator conferences and DPG spring meetings respectively.

My colleagues at TEMF and GSI were very welcoming and supportive. By name I wish to thank my long-time office mate and colleague Uwe Niedermayer and my former colleagues and office mates Sandra Aumon and Ivan Prokhorov for sharing a coffee when a break was necessary and never hesitating to debate a problem. Furthermore I wish to thank Sabrina Appel and Giuliano Franchetti for always having an open door for questions and discussions, be they scientific, organizational or political.

After some time of writing everyone becomes blind to his own errors. I wish to thank (in alphabetical order) Sandra Aumon, Anna Constantinescu, Lewin Ei-dam, Nico Formanek, Anna Hesse, Klaus Görgen, Matthias Holl, Uwe Niedermayer,

David Röhrscheid and Nikolai Schmitt for their help in combating this blindness by proofreading parts of the text and thereby making the document reach its final form.

I want to thank my family, especially my mother Renate Ehlerding for inspiring the fascination for science in me that allowed me to come this far. I also have to thank Klaus Görzen and Ute Wehrheim-Hesse for helping care for our son while my wife and myself were both finalizing our Theses. Finally I thank my wife Anna Hesse and my son Leif Görzen for giving up some of their time with me to allow me to finish this work and for making transitioning back to family in the evening the easiest thing in the world.

List of Figures

2.1	The RHIC accelerator chain	6
2.2	A RHIC electron lens	8
2.3	Original layout of the FAIR project	9
3.1	Coordinate system for parametrization of particle motion	13
3.2	Resonance diagram with resonance lines up to order 3	15
3.3	The phase space ellipse	17
3.4	Illustration of synchrotron satellites	20
3.5	Radial dependence of beam density, electric field and tune shift	26
3.6	Resonance diagram showing resonances up to $l = 3$ with space charge tune spread.	27
3.7	Cartoon of an electron lens	31
4.1	BTF measurement	34
4.2	Circuitry for Direct Diode Detection	35
4.3	BTF of a beam with momentum spread and chromaticity	38
4.4	BTF of a beam with tune spread from a Gaussian transverse charge distribution	41
4.5	BTFs of a coasting beam with space charge	42
5.1	Flowchart of particle tracking	46
5.2	Flowchart of particle-to-grid interpolation	49
5.3	Flowchart of the space charge simulation module	50
5.4	Illustration of slicing for space charge simulation with bunched beams	52
5.5	Flowchart of the beam-beam effect module	53
5.6	Illustration of the RHIC geometry	54
5.7	Illustration of the collision sequence	55
5.8	Validation of BTF implementation against a beam with momentum spread and chromaticity	58
5.9	Simulated and analytic BTFs of coasting beams with space charge . .	59
5.10	Validation of the implementation of the Beam-Beam effect	60
6.1	Comparison between analytic BTFs for bunched and coasting beams with space charge.	63
6.2	BTF and tune distribution for bunched beams with space charge . .	65
6.3	Simulation and analytic BTFs of bunched beams with frozen longitudinal motion	66

6.4	BTFs in the transition between the validity of the frozen synchrotron motion model and appearance of synchrotron satellites	69
7.1	Visualization of the relations between phase space density and BTF .	72
7.2	Threshold method applied to an analytic BTF	78
7.3	Threshold dependence of recovered ΔQ	79
7.4	Threshold method for a simulated BTF with coherent beam-beam modes	80
8.1	Comparison of BTFs of beams with weak-strong split tunes beam-beam interactions beams interacting with an electron lens	83
8.2	Bunching scheme of the experiment	85
8.3	Coherent beam-beam modes between strong bunches	87
8.4	BTF measurement in horizontal direction before and after separation	89
8.5	BTF measurement in vertical direction before and after separation .	90
8.6	BTF measurement in horizontal and vertical direction after tune splitting	91
8.7	Threshold method applied to measurements with an electron lens .	94
8.8	Threshold method on a measured BTF with coherent beam-beam modes	95

List of Tables

8.1	Simulation parameters showing negligible synchrotron motion	83
8.2	Comparison between different measures for beam-beam parameter .	92



List of Symbols

Units are given in SI or derived SI units where applicable. An arrow over a symbol denotes a vectorized quantity, where applicable the same symbol without the arrow is used for the absolute value of the quantity. A dot over a quantity denotes the derivative of the quantity with respect to time. A hat denotes a quantity Fourier-transformed with respect to time. $\langle \cdot \rangle$ indicates a mean value.

Symbol	Description	Units	Page
$\alpha(s)$	An alpha function	1	14
α_x	The horizontal alpha function	1	14
α_y	The vertical alpha function	1	14
\vec{B}	The magnetic flux density, as only fields in vacuum are discussed sometimes referenced to as magnetic field	T	11
β	Relativistic factor $\beta = v/c$	1	12
β_x^*	The horizontal beta function at the interaction point	m	29
β_y^*	The vertical beta function at the interaction point	m	29
$\beta(s)$	A beta function	m	14
β_x	The horizontal beta function	m	14
β_y	The vertical beta function	m	14
C_{circ}	The machine circumference	m	12
c	The speed of light	m s^{-1}	12
δ	The relative momentum deviation	1	13
ΔQ_{chrom}	RMS tune shift due to momentum spread and chromaticity	1	22, 62
ΔQ_k	Tune shift of the k^{th} synchrotron satellite	1	43
Δt	A time difference	s	12
ΔU_{coh}	Real part of the coherent space charge tune shift in units of ΔQ_{chrom}	1	41
ΔU_{sc}	Incoherent space charge tune shift in units of ΔQ_{chrom}	1	41
ΔV_{coh}	Imaginary part of the coherent space charge tune shift in units of ΔQ_{chrom}	1	41
\vec{E}	The electric field	V m^{-1}	11

Symbol	Description	Units	Page
ε	An emittance, RMS-emittance unless otherwise noted	m	16, 21
\vec{e}_x	The unit vector in the horizontal direction of the co-moving coordinate system	m	12
\vec{e}_y	The unit vector in the vertical direction of the co-moving coordinate system	m	12
\vec{e}_z	The unit vector along the trajectory of the reference particle in the co-moving coordinate system	m	12
\vec{F}	A force	N	11
f_0	The revolution frequency	s^{-1}	21
ϕ_i	A phase	1	19
f_0	The synchrotron frequency	s^{-1}	18
φ	An electric potential	V	23
γ	Relativistic factor $\gamma = (1 - \beta^2)^{-\frac{1}{2}}$	1	12
$\gamma(s)$	A gamma function	m^{-1}	14
γ_x	The horizontal gamma function	m^{-1}	14
γ_y	The vertical gamma function	m^{-1}	14
γ_T	Transition γ	1	21
\vec{H}	The magnetic \vec{H} field	$A m^{-1}$	11, 18, 38
J	The particle action	m	14
k	A focusing strength	m	14
Λ	Yokoya factor	1	30
m_0	Rest mass	kg	12
μ_0	The vacuum permittivity	$F m^{-1}$	11
ω_0	The angular revolution frequency	s^{-1}	21
ω_s	The angular synchrotron frequency	s^{-1}	18
p	A momentum	$kg m s^{-1}$	13
p	Normalized betatron coordinate (in Section 4.3)		38
Ψ	A phase		14
ψ	A density		36
Ψ_j	A phase	1	19
Q	A tune	1	14
q	A charge	C	11
Q_0	A tune	1	15
q	Normalized betatron coordinate (in Section 4.3)		38
Q_{frac}	The fractional part of Q	1	16
Q_s	The synchrotron tune	1	18

Symbol	Description	Units	Page
R	A beam transfer function		33
r_{aspect}	Aspect ratio of a beam for the calculation of the Yokoya factor	1	30
ρ	Bending radius in magnetic field	m	12
ϱ	Particle density		23
σ	A σ width of a distribution		23, 37
\vec{v}	A velocity vector	m s^{-1}	11
\vec{v}_0	The velocity of the reference particle	m s^{-1}	12
ξ_{chrom}	The chromaticity	1	22
ξ_x	The horizontal beam-beam parameter	1	29
ξ_y	The vertical beam-beam parameter	1	29



List of Acronyms

AGS Alternating Gradient Synchrotron.

BNL Brookhaven National Laboratory.

BTF Beam Transfer Function.

DC Direct current.

ESR Experimentierspeicherring.

FAIR Facility for Antiproton and Ion Research in Europe.

GSI GSI Helmholtzzentrum für Schwerionenforschung GmbH.

IP Interaction point.

LHC Large Hadron Collider.

RHIC Relativistic Heavy Ion Collider.

RMS Root mean square.

SI International system of units (Système International d'unitées).

SIS100 Schwerionensynchrotron 100.

SIS18 Schwerionensynchrotron 18.

UNILAC Universal Linear Accelerator.

Bibliography

- [1] W. Crookes. On radiant matter. *Popular Science Monthly*, 16, 1879.
- [2] E. Rutherford. The scattering of alpha and beta particles by matter and the structure of the atom. *Philosophical Magazine*, 21:669, 1911.
- [3] J. D. Cockcroft and E. T. S. Walton. Experiments with high velocity positive ions.
–(i) further developments in the method of obtaining high velocity positive ions. *Proceedings of the Royal Society A*, 129:447ff, 1930.
- [4] R. Wideröe. Über ein neues prinzip zur herstellung hoher spannungen. *Archiv für Elektrotechnik*, 21(4):387, 1928.
- [5] J. D. Lawson and G. Brianti. *50 Years of Synchrotrons*. CERN, Geneva, 1997.
- [6] E. Courant and H. Snyder. Theory of the alternating-gradient synchrotron. *Annals of Physics*, 3(1):1, 1958.
- [7] R. W. Hamm and M. E. Hamm. The beam business: Accelerators in industry feature. *Physics Today*, 64(6), 2011.
- [8] D. W. Kerst, F. T. Cole, H. R. Crane, L. W. Jones, L. J. Laslett, et al. Attainment of very high energy by means of intersecting beams of particles. *Physical Review*, 102(2):590, 1956.
- [9] G. K. O'Neill. Storage-ring synchrotron: Device for high-energy physics research. *Physical Review*, 102(5):1418, 1956.
- [10] M. Harrison, S. Peggs, and T. Roser. The rhic accelerator. *Annual Review of Nuclear and Particle Science*, 52(1):425, 2002.
- [11] M. Brennan, P. Cameron, P. Cerniglia, R. Connolly, J. Cupolo, et al. Tune measurement in RHIC. In *Tenth Workshop on Beam Instrumentation*, pp. 134–149. American Institute of Physics, 2002.
- [12] L. Evans and P. Bryant. LHC machine. *Journal of Instrumentation*, 3(08), 2008.
- [13] J. Borer, G. Guignard, A. Hofmann, E. Peschardt, F. Sacherer, et al. Information from beam response to longitudinal and transverse excitation. *Transactions on Nuclear Science*, 26(3):3405, 1979.
- [14] A. W. Chao. *Physics of Collective Beam Instabilities in High Energy Accelerators*. WILEY-VCH, New York, 1993.

- [15] W. Herr. Beam-beam interactions. In *Proceedings of the CERN Accelerator School on Intermediate Accelerator Physics*. Fermi National Accelerator Laboratory (FNAL), Batavia, IL, CERN, 2003.
- [16] V. Shiltsev, Y. Alexahin, K. Bishofberger, V. Kamerdzhiev, G. Kuznetsov, et al. Experimental demonstration of colliding-beam-lifetime improvement by electron lenses. *Physical Review Letters*, 99(24):244801, 2007.
- [17] W. Fischer, X. Gu, S. M. White, Z. Altinbas, D. Bruno, et al. First experience with electron lenses for beam-beam compensation in RHIC. In *Proceedings of 5th International Particle Accelerator Conference*. 2014.
- [18] G. Stancari, A. Valishev, R. Bruce, S. Redaelli, A. Rossi, et al. Electron lenses for the large hadron collider. In *Proceedings of the 5th International Particle Accelerator Conference*. 2014.
- [19] K. Schindl. Space charge. In *Proceedings of the CERN Accelerator School: Intermediate Course on Accelerator Physics*. CERN, 2006.
- [20] S. Paret, V. Kornilov, and O. Boine-Frankenheim. Transverse schottky and beam transfer function measurements in space charge affected coasting ion beams. *Physical Review Special Topics - Accelerators and Beams*, 13(2):1, 2010.
- [21] R. Singh, O. Boine-Frankenheim, O. Chorniy, P. Forck, R. Haseitl, et al. Interpretation of transverse tune spectra in a heavy-ion synchrotron at high intensities. *Physical Review Special Topics - Accelerators and Beams*, 16(3):034201, 2013.
- [22] O. Boine-Frankenheim and V. Kornilov. Transverse schottky noise spectrum for bunches with space charge. *Physical Review Special Topics - Accelerators and Beams*, 12(11):1, 2009.
- [23] M. Blaskiewicz. Fast head-tail instability with space charge. *Physical Review Special Topics - Accelerators and Beams*, 1(4):1, 1998.
- [24] R. Berg, H. Blosser, and M. Gordon. Theoretical and experimental beam studies for the michigan state university cyclotron. *Nuclear Instruments and Methods in Physics Research, Section A: Accelerators, Spectrometers, Detectors and Associated Equipment*, 58(2):327, 1968.
- [25] G. H. Rees. Beam-beam interactions: in e-p storage rings. In *Proceedings of the 1st International School of Particle Accelerators Ettore Majorana*, pp. 341–376. CERN, Erice, Italy, 1977.

[26] E. Keil. Beam-beam interactions: in p-p storage rings. *Proceedings of the 1st International School of Particle Accelerators Ettore Majorana*, pp. 341–376, 1977.

[27] S. Machida. Space-charge effects in low-energy proton synchrotrons. *Nuclear Instruments and Methods in Physics Research, Section A: Accelerators, Spectrometers, Detectors and Associated Equipment*, 309(1-2):43, 1991.

[28] H. J. Kim and T. Sen. Beam-beam simulation code BBSIM for particle accelerators. *Nuclear Instruments and Methods in Physics Research, Section A: Accelerators, Spectrometers, Detectors and Associated Equipment*, 642(1):25, 2011.

[29] Python/c++ implementation of the orbit (objective ring beam injection and tracking) code. URL <https://code.google.com/p/py-orbit/>.

[30] O. Boine-Frankenheim and V. Kornilov. Implementation and validation of space charge and impedance kicks in the code patric for studies of transverse coherent instabilities in the fair rings. In *Proceedings of ICAP 2006*, pp. 267–270. 2006.

[31] Particle accelerators, encyclopedia britannica online, accessed 2015-05-26. URL <http://www.britannica.com/EBchecked/topic/445045/particle-accelerator/60521/Proton-synchrotrons>.

[32] R. A. Beth and C. Lasky. The brookhaven alternating gradient synchrotron. *Science (New York, N.Y.)*, 128(3336):1393, 1958.

[33] D. Trbojevic and S. Peggs. Required accuracy of the RHIC circumference, RHIC/AP 3. Technical Report RHIC/AP 3, Brookhaven National Laboratory, Upton, NY, 1993.

[34] Z. Parsa. Booster parameter list with 40kv rf voltage. Technical report, Brookhaven National Laboratory, Upton, NY, 1986.

[35] M. Bai, L. Ahrens, I. G. Alekseev, J. Alessi, J. Beebe-Wang, et al. Polarized proton collisions at RHIC. *Proceedings of PAC 2005*, 2005.

[36] Collider-Accelerator Department. RHIC configuration manual. Technical report, Brookhaven National Laboratory, 2000.

[37] A. N. Zelenski, V. Klenov, Y. A. Kuznetsov, V. Zoubets, G. Dutto, et al. Optically-pumped polarized h^- ion sources for RHIC and HERA colliders. In *Proceedings of the 1999 Particle Accelerator Conference*. IEEE, 1999.

- [38] W. Weng, L. Ahrens, R. Damm, and A. McNerney. Construction and early commissioning results of the ags booster. In *Proceedings of the 1991 IEEE Particle Accelerator Conference*, pp. 8–12. 1991.
- [39] I. Alekseev, C. Allgower, M. Bai, Y. Batygin, L. Bozano, et al. Polarized proton collider at RHIC. *Nuclear Instruments and Methods in Physics Research, Section A: Accelerators, Spectrometers, Detectors and Associated Equipment*, 499(2-3):392, 2003.
- [40] M. Gasior. Faraday cup award: High sensitivity tune measurement using direct diode detection. In *Proceedings of the Beam Instrumentation Workshop*. Newport News, VA, USA, 2012.
- [41] W. Fischer, Z. Altinbas, M. Anerella, M. Blaskiewicz, D. Bruno, et al. Status of head-on beam-beam compensation in RHIC. (arXiv:1410.5315):12 p, 2014.
- [42] Gsi facts and figures, accessed 2015-06-15. URL https://www.gsi.de/en/start/about_us/facts_and_figures.htm?nr=%2Fproc%2Fself%25.
- [43] B. Franczak. SIS parameter list, 1987.
- [44] SIS100 working group. Fair technical design report - SIS 100. Technical report, GSI Gesellschaft für Schwerionenforschung, Darmstadt, 2008.
- [45] H. H. Gutbrod, I. Augustin, H. Eickhoff, K.-D. Groß, W. F. Henning, et al., editors. *Fair Baseline Technical Design Report*. Darmstadt, 2006.
- [46] W. Barth, A. Adonin, S. Appel, P. Gerhard, M. Heilmann, et al. Heavy ion linac as a high current proton beam injector. *Physical Review Special Topics - Accelerators and Beams*, 18(5), 2015.
- [47] R. Singh. *Tune Measurement at GSI SIS-18: Methods and Applications*. Ph.D. thesis, TU Darmstadt, 2013.
- [48] S. Paret. *Transverse Schottky Spectra and Beam Transfer Functions of Coasting Ion Beams with Space Charge*. Ph.D. thesis, TU Darmstadt, 2010.
- [49] J. D. Jackson. *Classical Electrodynamics*. WILEY-VCH, 3rd edition, 1999.
- [50] K. Wille. *The physics of particle accelerators: an introduction*. Oxford Univ. Press, Oxford, 2000.
- [51] S. Y. Lee. *Accelerator physics*. World Scientific, Singapore, 1999.

- [52] K. Wille. *Physik der Teilchenbeschleuniger und Synchrotronstrahlungsquellen*. Teubner, Stuttgart, 1996.
- [53] M. Reiser. *Theory and Design of Charged Particle Beams*. WILEY-VCH, Weinheim, 1994.
- [54] S. Chattopadhyay. *Some fundamental aspects of fluctuations and coherence in charged-particle beams in storage rings*. CERN, Geneva, 1984.
- [55] D. Boussard. Schottky noise and beam transfer function diagnostics. In S. Turner, editor, *Proceedings of the CERN Accelerator School: 5th Advanced Accelerator Physics Course*, pp. 749–782. CERN, 1995.
- [56] E. W. Weisstein. *Jacobi – Anger Expansion*.
- [57] J. Rossbach and P. Schmüser. Basic course on accelerator optics. In *Proceedings of the CERN Accelerator School*, pp. 17–88. CERN, 1994.
- [58] M. Bassetti. Closed expression for the electrical field of a two-dimensional Gaussian charge. *CERN-Report ISR-TH/80-06*, 1980.
- [59] L. Palumbo, V. G. Vaccaro, and M. Zobov. Wake fields and impedance. In *Proceedings of the CERN Accelerator School*, volume 041, p. 70. CERN, 1994.
- [60] S. Kheifets. Potential of a three-dimensional Gaussian bunch, petra-note-119. Technical report, DESY, Hamburg, 1976.
- [61] A. Burov and V. Lebedev. Transverse instabilities of coasting beams with space charge. *Physical Review Special Topics - Accelerators and Beams*, 12(3):034201, 2009.
- [62] A. W. Chao, K. H. Mess, M. Tigner, and F. Zimmermann, editors. *Handbook of Accelerator Physics and Engineering*. World Scientific, Singapore, second edition, 2012.
- [63] E. Métral and H. B. Cern. Achievable space-charge tune shift with long lifetime in the CERN PS and SPS. pp. 153–156, 2008.
- [64] M. Reiser, P. O’Shea, R. Kishek, S. Bernal, P. Chin, et al. The maryland electron ring for investigating space-charge dominated beams in a circular fodo system. volume 1, pp. 234–236. IEEE, 1999.

- [65] B. Beaudoin and R. A. Kishek. Tune variation and transverse displacement as a diagnostic for profiling beam energy. *Physical Review Special Topics - Accelerators and Beams*, 114201(January 2012):1, 2013.
- [66] K. Yokoya and K. Haruyo. Tune shift of coherent beam-beam oscillations. *Particle Accelerators*, 27:181, 1990.
- [67] R. Calaga, W. Fischer, G. Robert-Demolaize, and N. Milas. Long-range beam-beam experiments in the relativistic heavy ion collider. *Physical Review Special Topics - Accelerators and Beams*, 14(9):1, 2011.
- [68] A. W. Chao. Beam-beam instability, SLAC-PUB 3179. Technical report, 1983.
- [69] M. Gasior and R. Jones. The principle and first results of betatron tune measurement by direct diode detection, LHC project report 853. Technical report, CERN, Geneva, 2005.
- [70] K. Ng. *Physics of Intensity Dependent Beam Instabilities*. World Scientific, Singapore, 2006.
- [71] J. Berg and F. Ruggiero. Landau damping with two-dimensional betatron tune spread. *CERN-SL (AP)*, 71, 1996.
- [72] O. Boine-Frankenheim, V. Kornilov, and S. Paret. Measurement and simulation of transverse schottky noise with space charge. *Physical Review Special Topics - Accelerators and Beams*, 11(7):1, 2008.
- [73] B. Stroustrup. *The C++ Programming language*. Addison-Wesley, 4th edition, 2013.
- [74] Mad-x. URL <http://madx.web.cern.ch/madx/>.
- [75] V. Kapin. A method for numerical solution 2d poissons equation with image fields. In *Proceedings of EPAC 2002*, pp. 1637–1639. 2002.
- [76] C. K. Birdsall. *Plasma Physics via Computer Simulation*. Taylor and Francis, 2004.
- [77] R. W. Hockney and J. W. Eastwood. *Computer Simulation Using Particles*. IOP Publishing, London, 1988.
- [78] M. Zorzano and F. Zimmermann. Simulations of coherent beam-beam modes at the large hadron collider. *Physical Review Special Topics - Accelerators and Beams*, 3(January):1, 2000.

[79] W. Herr, M. P. Zorzano, and F. Jones. Hybrid fast multipole method applied to beam-beam collisions in the strong-strong regime. *Physical Review Special Topics - Accelerators and Beams*, 4:37, 2001.

[80] M. Furman. Hourglass effects for asymmetric colliders. In *Proceedings of the 1991 IEEE Particle Accelerator Conference*. IEEE, San Francisco, CA, USA, 1991.

[81] H. S. Matis, R. L. Brown, W. Christie, W. R. Edwards, R. Jared, et al. Integration and conventional systems at STAR. *Nuclear Instruments and Methods in Physics Research, Section A: Accelerators, Spectrometers, Detectors and Associated Equipment*, 499(2-3):802, 2003.

[82] The PHENIX collaboration. sPHENIX: An upgrade concept from the PHENIX collaboration, 2012.

[83] S. G. Johnson, A. Cervelino, and J. Wuttke. libcerf, numeric library for complex error functions, 2013. URL <http://apps.jcns.fz-juelich.de/libcerf>.

[84] D. Stranneby and W. Walker. *Digital Signal Processing and Applications*. Elsevier, second edition, 2004.

[85] T. Pieloni, W. Herr, A. Bay, and L. Rivkin. *A study of beam-beam effects in hadron colliders with a large number of bunches*. Ph.D. thesis, Ecole Polytechnique, Lausanne, 2008.

[86] K. Yokoya. Limitation of the Gaussian approximation in beam-beam simulations. *Physical Review Special Topics - Accelerators and Beams*, 3(September), 2000.

[87] A. Sørensen. Crossing the phase transition in strong-focusing proton synchrotrons. *Particle Accelerators*, 6(3):141, 1975.

[88] T. Risselada. Gamma transition jump schemes. In *Proceedings of the CERN Accelerator School: 5th General Accelerator Physics Course*, pp. 313–328. CERN, 1994.

[89] R. Meiler, A. Chao, J. Peterson, and S. Peggs. Decoherence of kicked beams, SSCL-N-360. Technical report, 1987.

[90] S. Y. Lee. Decoherence of kicked beams II, SSCL-N-749. Technical Report February, 1991.

- [91] E. Jones, T. Oliphant, P. Peterson, and Others. SciPy: Open source scientific tools for Python. URL <http://www.scipy.org/>.
- [92] P. Görgen, O. Boine-Frankenheim, and W. Fischer. Beam transfer functions for relativistic proton bunches with beam-beam interaction. *Nuclear Instruments and Methods in Physics Research, Section A: Accelerators, Spectrometers, Detectors and Associated Equipment*, 777:43, 2015.
- [93] Wolfram Research Inc. Mathematica, 2014.
- [94] Y. Alexahin. A study of the coherent beam-beam effect in the framework of the vlasov perturbation theory. *Nuclear Instruments and Methods in Physics Research, Section A: Accelerators, Spectrometers, Detectors and Associated Equipment*, 480(2-3):253, 2002.
- [95] S. White, M. Bai, W. Fischer, Y. Luo, A. Marusic, et al. Coherent beam-beam effects observation and mitigation at the RHIC collider. In *Proceedings of the 3rd International Particle Accelerator Conference*. New Orleans, USA, 2012.

Paul Görge

Lebenslauf

Education

2011–2015 **PhD candidate**, *Computational Electromagnetics Laboratory*, TU Darmstadt.
(est. July) On accelerator physics, topic: *Beam Transfer Functions for Relativistic Ion Bunches with Space-charge and Beam-beam Effect*.

2009–2011 **Master of science in Physics**, *TU Darmstadt*, final grade 1.46.

2005–2009 **Bachelor of science in Physics**, *TU Darmstadt*, final grade 2.6.

1995–2004 **Abitur**, *Justus Liebig Gymnasium*, Darmstadt, final grade 1.9.

Grades in the German grading system, from 1 (very good/outstanding) to 6; failing grades 5 and 6.

Work

2011–2015 **PhD candidate**, *TU Darmstadt Computational Electromagnetics Laboratory / GSI (Facility for Heavy Ion Research)*, Darmstadt, Germany.
Research topic: Beam physics simulation using a MPI based parallel simulation code. Member of the beam physics group on site at GSI 2011–2014. Apart from research: administration of linux development nodes and responsible for interfacing between beam physics group and HPC group.

2012, 2013 **Visiting Scientist**, *Brookhaven National Laboratory (BNL)*, Upton, NY, USA.
Three months total at BNL: preparation and conduction of measurements, collaboration on PhD-thesis related topics. Results published in [1].

2005–2010 **Student assistant**, *TU Darmstadt University computing centre*, Darmstadt, Germany.
Computer support for students and institutes of the university, all operating systems. From simple hardware- and network configuration up to data recovery from crashed systems and setup of new machines. Writing and maintaining of documentation for hard- and software.

2007–2008 **Student assistant**, *TU Darmstadt Physics Department*, Darmstadt, Germany.
Supervision of lab courses in experimental physics.

2004–2005 **Civil service**, *Department for radiotherapy, Klinikum*, Darmstadt, Germany.
Civil service as a alternative to German military service. Morning power-up of the therapy accelerators, daily reference measurements and compilation of their time trends.

Volunteer work

2014 **Representative of GSI**, *Helmholtz Juniors, representation of PhD candidates in Helmholtz Society*.
Leading a team of 7 in the conduction and evaluation of a survey on working conditions among the 6000 PhD candidates of the 18 Helmholtz Institutes. Also responsible for running the infrastructure (etherpad / webrtc / web server), selection and operation of the survey platform, and development of the interactive website for the evaluation of the results.

Computer Skills

Programming	Python, Cython, C++, C, Perl, Java, JavaScript, MPI, Shellscript (Bash), Perl, R, Git
Administration	Linux Kernel (patching and compiling), Virtual machines (KVM/qemu, Virtualbox), Web servers (Lighttpd, Apache, node.js), RAID, NFS, Seafile, NIS, Iptables, Dmcrypt, FlexLM
Scientific Computing	Parallelization (MPI), Gridengine, Lustre, Numpy, Cython, Mathematica, CST-Studio, Particle tracking simulations
Office	L ^A T _E X, HTML, Office

Language skills

German	Native	
English	Fluent	<i>Self-assessment: C1/C2 in the Common European Framework of Reference for Languages (CEFR). I communicate with my colleagues primarily in English.</i>
French	Basics	<i>Self-assessment: A2/B1 in CEFR</i>

Grants and Scholarships

2011–present **University of Darmstadt**, *Scholarship for my PhD Thesis*.

2014, 2011 **European Physical Society Accelerator Group EPS-AG**, *Scholarship for accomodation and conference fees for the International Particle Accelerator Conference*.

2013, 2011 **W. u. E. Heraeus-Stiftung**, *Scholarship for accomodation and conference fees for the spring meeting of the German physical society*.

2012 **Helmholtz Graduate School for Heavy Ion Research**, *HGS-HIRe abroad travel scholarship for a 2 month period as a guest scientist at Brookhaven National Laboratory*.

Extracurricular activities

Sports events Organized the participation in short distance triathlons for company-teams of 10 for my university institute, graduate school and GSI for the past three years.

Publications

Peer-reviewed journals

[1] P. Görgen, O. Boine-Frankenheim, and W. Fischer. Beam transfer functions for relativistic proton bunches with beam-beam interaction. *Nuclear Instruments and Methods A – Accelerators and Beams*, 2014.

Conference proceedings

[2] P. Görgen, O. Boine-Frankenheim, and W. Fischer. Beam-Beam Effect on the BTF in Bunched Beams. In *Proceedings of the 5th International Particle Accelerator Conference*, Dresden, Germany, 2014.

[3] P. Görgen, O. Boine-Frankenheim, and W. Fischer. BTF Measurements with Beam-Beam Interactions. In *Proceedings of the ICFA Mini-Workshop on Beam-Beam Effects in Hadron Colliders, 18-22 Mar 2013*, Geneva, Switzerland, 2014. CERN, arXiv:physics.acc-ph/0707.3168.

[4] P. Görgen, O. Boine-Frankenheim, W. Fischer, and S. White. Simulation of Baseband BTF using a Particle-In-Cell code. In *Proceedings of the 11th Computational Accelerator Physics Conference*, Rostock, Germany, 2012.

[5] P. Görgen, O. Boine-Frankenheim, S. Appel, C. Dimopoulou, S. Litvinov, and M. Steck. Experimental Studies of Beam Loss during Low Energy Operation with Electron Cooled Heavy Ions in the ESR. In *Proceedings of the 2nd International Particle Accelerator Conference*, San Sebastian, Spain, 2011.

Oral presentations without publication in proceedings

[6] P. Görgen, O. Boine-Frankenheim, and W. Fischer. Beam Transfer Functions and Tune Spread in Bunched Beams. In *Oral presentation during the DPG Spring meeting*, Wuppertal, 2015.

[7] P. Görgen, O. Boine-Frankenheim, and W. Fischer. Transverse Beam Transfer Functions: Measurements and Simulations. In *Hic4Fair physics day on Accelerator Physics*, Frankfurt, 2014.

[8] P. Görgen, O. Boine-Frankenheim, and W. Fischer. Tune spread reconstruction from beam transfer functions at high energy. In *Advances in electromagnetic fields research*, Riezlern, Austria, 2014.

[9] P. Görgen. Beam-Beam, Electron lenses, Beam transfer functions and why we care. In *HGS HIRe Graduate Days*, Worms, 2013.

[10] P. Görgen, O. Boine-Frankenheim, and W. Fischer. Transverse baseband beam transfer functions of beams under the influence of the beam-beam effect or an electron lens. In *Advances on electromagnetic fields research*, Riezlern, Austria, 2013.

[11] P. Görgen, O. Boine-Frankenheim, and W. Fischer. Analyse von transversalen Beamtransferfunktionen für intensive Ionenstrahlen. In *Oral presentation during the DPG Spring meeting*, Dresden, 2013.

[12] P. Görgen. Transversal BTF considerations with beam-beam in RHIC. In *Oral presentation during the Arbeitstreffen Kernphysik*, Schleching, 2013.

[13] P. Görgen, O. Boine-Frankenheim, and W. Fischer. Simulation of transverse baseband beam transfer functions using a particle-in-cell code. In *Advances in electromagnetic fields research*, Riezlern, Austria, 2012.

Reports

[14] P. Görgen and O. Boine-Frankenheim. *Observation and simulation of transverse BTFs of high energy bunched beams*, volume 2014-1 of *GSI Report*. GSI Helmholtzzentrum für Schwerionenforschung, Darmstadt, 2014.

[15] P. Görgen, O. Boine-Frankenheim, and W. Fischer. *BTF of beams influenced by a localized Gaussian charge distribution*, volume 2013-1 of *GSI Report*. GSI Helmholtzzentrum für Schwerionenforschung, Darmstadt, 2013.